LOW THERMAL STABILITY MAGNETIC TUNNEL JUNCTIONS FOR COMPUTING APPLICATIONS

A dissertation submitted
to Carnegie Mellon University in partial
fulfillment of the requirements for the
degree of Doctor of Philosophy

by
Bradley Parks
July 2021

Doctoral dissertation written by

Bradley Parks

M.S., Carnegie Mellon University, Pittsburgh PA, USA 2017

B.S. University of California, Los Angeles, Los Angeles, CA, USA 2015

Acknowledgments

This work was a huge team effort. I had great group of senior graduate students to teach me the methods I needed. I learned the ways of nanofabrication from Stephan Piotrowski and Samuel Oberdick. I learned the conductive AFM test from Mukund Bapna. It has also been great to work with Hao Chen on nanofabrication and circuit designs and just throwing ideas around.

I could not ask for a better advisor than Sara Majetich. She struck the right balance of being tough and demanding results and allowing me to try new ideas, sometimes at great expense. She has been fair, and she has always gone to bat for me with the department, with funding, and with potential employers.

Abstract

Thermally stable magnetic tunnel junctions (MTJs) have been used for years for data storage. They have been proposed for use as cache memory in sometimes-on processors. However, thermally unstable magnetic tunnel junctions can be used for novel logic operations. These novel logic operations require an electronic means of influencing the likelihood of the MTJ being in one state or the other. They also require a means of reading the statistical output of the thermally switching devices and of comparing those outputs to one another. In this work, I present two electronic means of influencing the state of the devices, spin transfer torque and spin orbit torque. I also present two different means of controlling the rate of thermal reversal, voltage controlled magnetic anisotropy and a hard axis magnetic field. Finally, I demonstrate a stochastic AND operation combining the spin transfer torque influencing of the device state and the hard axis magnetic field control of the thermal reversal rate. This stochastic AND operation can be scaled up to more complex operations using more stochastically switching MTJ devices.

Preface

When I began my graduate research, I was working on high thermal stability magnetic tunnel junctions (MTJs) similar to the type used for data storage and magnetic memory. I was assisting the senior graduate students with their research as I learned the techniques we used in the nanofabrication lab and for electronic test of our devices. As the size of the devices became smaller and smaller, we started to see random telegraph noise due to the thermal magnetization reversal in our MTJs. In trying to understand this thermal reversal, I stumbled across papers about stochastic logic using a random telegraph noise that was influenced electronically to favor one voltage level or another. The goal of my thesis research quickly became the demonstration of a stochastic logic operation using low thermal stability magnetic tunnel junctions as the source of the telegraph noise. This document tells the story from some of my first attempts at nanofabrication to prototyping the stochastically switching MTJs and mechanisms to control their telegraph noise. It all culminated with the demonstration of a stochastic AND gate using three low stability MTJs.

In Chapter 1, I introduce MTJs, tunnel magnetoresistance (TMR), and magnetic anisotropy. These are the building blocks of the rest of the thesis in terms of the fabricated devices, the resistance contrast mechanism, and the static behavior of the MTJs. I then describe superparamagnetism in terms of patterned thin film ferromagnets. This describes the thermal magnetization reversal and its associated random telegraph noise (RTN) signal, which is the characteristic I aim to exploit to eventually perform a stochastic computing operation.

In Chapter 2, I introduce the primary control mechanisms I use manipulate my MTJs, spin transfer torque (STT) and spin orbit torque (SOT). I provide an explanation of a simple cartoon model of STT as well as a brief presentation of the STT component of the Landau Lifschitz Gilbert (LLG) equation. I then break down SOT into its competing theories, the

Rashba effect and the spin Hall effect. These mechanisms for electronically writing an MTJ bit have been studied for data storage applications, but I used them to influence a stochastically switching magnetization.

In Chapter 3, I present a result I worked on as a junior graduate student: the switching of a high thermal stability perpendicular MTJ using SOT. This was the smallest MTJ to be switched using SOT up to the time of publication. This project was led by Mukund Bapna and is the only high thermal stability MTJ experiment presented in the thesis. My contribution was to fabricate the device, with the help of Sam Oberdick, and build some of the test circuitry as I was continuing to learn about SOT.

Chapter 4 is my first published paper on the use of a low thermal stability perpendicular MTJ to generate true random numbers. This was the first project that I lead. I fabricated and measured the device independently. The ability to generate random numbers quickly is an important enabling technology for cryptography. It also represents one side of the cryptographic arms race, with invertible stochastic computing being the other. Mukund Bapna assisted with some of the data analysis in this paper.

In Chapter 5, I fabricated prototype stochastic MTJs with STT control. The ability to electronically influence the MTJ's state probabilistically was a key component to building a stochastic logic circuit. The data presented in Chapter 5 was published in a paper I worked on with Ahmed Abdelgawad. I performed the fabrication, test, and some of the data analysis for the experiment. Ahmed did some of the data analysis as well as simulations in support of the experimental results. Thomas Wong also assisted with some of the data analysis. The thermal magnetization reversal rate shown in the data in Chapter 5 held the speed record for a few years until recently being superseded in 2021.

Chapter 6 presents some comparative results of pure STT switching and STT/SOT hybrid switching. This was another prototype device investigated for use in the stochastic logic circuit. The SOT current reduced the necessary STT current as expected, but I ultimately determined the current density benefit of hybrid switching was not worth the extra channel necessary for SOT.

Chapter 7 is the full demonstration of the stochastic controlled NOT and stochastic AND operations. The AND gate operated in both the forward and reverse directions, allowing the user to set the result of a computation and read out the list of possible inputs that lead to that result. This technology will greatly reduce the time to solve difficult problems, such as prime factorization. The ability to quickly perform prime factorization is necessary for breaking encryption.

Chapter 8 is an investigation into an effect I discovered while performing the AND gate experiment. I found that I could apply a magnetic field along the magnetic hard axis of the MTJ and cause it to thermally reverse at a greater rate. I performed angle-resolved magnetic field switching on one of the devices used in the AND gate. I discovered a cubic component to the magnetic anisotropy in a device that should have been uniaxial due to its shape anisotropy.

Parts of this thesis have been published in the following journal articles:

1. **Parks, B.**, Abdelgawad A., Wong, T., & Majetich, S. A. (2019). Magnetoresistance dynamics in superparamagnetic CoFeB nanodots. *Physical Review Applied*, *13*, 014063.

2. **Parks, B.**, Bapna, M., Igbokwe, J., Almasi, H., Wang, W., & Majetich, S. A. (2018). Superparamagnetic perpendicular magnetic tunnel junctions for true random number generators. *AIP Advances*, *8*(5), 055903.

3. Bapna, M., **Parks, B.**, Oberdick, S. D., Almasi, H., Wang, W., & Majetich, S. A. (2018). Spin-Orbit-Torque Switching in 20-nm Perpendicular Magnetic Tunnel Junctions. *Physical Review Applied*, *10*(2), 024013.

And presented in the following symposiums and conferences:

- “Hardwired MTJs for Stochastic Computing”, Oral, Magnetism and Magnetic Materials conference (MMM) 2019, Las Vegas, NV
- “Comparison of Spin Transfer Torque and Spin Orbit Torque in a Superparamagnetic Tunnel Junction”, Oral, Joint MMM-Intermag conference 2019, Washington D.C.
- “Superparamagnetic Tunnel Junctions for Probabilistic Computing”, Poster, International Conference on Magnetism 2018, San Francisco, CA
- “Voltage-Controlled Magnetic Tunnel Junctions for Probabilistic Computing”, Oral, Magnetism and Magnetic Materials conference (MMM) 2017, Pittsburgh, PA
- “Hardwired Magnetic Tunnel Junctions for Stochastic Computing”, Poster, Center for Spintronics Annual Review Meeting 2017, Minneapolis, MN
- “Detection of Spin Hall Effect Switching of Nanomagnets with Conductive Atomic Force Microscopy**”,** Poster, IEEE Magnetics Society Summer School 2017, Santander, Spain
- “Thermal Switching of Magnetization States in Fe_3O_4 Nanocubes”, Oral, Magnetism and Magnetic Materials conference (MMM) 2016, New Orleans, LA

Table of Contents

List of Figures

List of Tables

Chapter 1 Magnetic Tunnel Junctions and Superparamagnetism

I used the device physics of superparamagnetic magnetic tunnel junctions to perform novel computing operations, so it is important to understand the device physics. Here I introduce magnetic tunnel junctions in general, the tunnel magnetoresistance effect, and superparamagnetism as it applies to patterned thin films. I also describe some of the design considerations involved in selecting thin film materials.

1.1 Magnetic Tunnel Junctions

Magnetoresistance is the change in electrical resistance of a ferromagnet in a magnetic field. Magnetoresistance devices have been part of data recording technology for decades since the introduction of the magnetoresistive head in 1990. Anisotropic magnetoresistance (AMR), the tendency for electrical resistance across a ferromagnetic metal to vary depending on the direction of an external magnetic field, was discovered by William Thomson in 1857 [1]. The use first use of magnetoresistance in technology was the invention of the magnetoresistive readout transducer by Robert Hunt in 1971 [2]. AMR was superseded by giant magnetoresistance (GMR) after it was discovered by Albert Fert and Peter Grunberg in 1988 [3,4]. GMR spin valves consist of two ferromagnetic metals separated by a non-magnetic metal layer. The separating non-magnetic layer is necessary to reduce magnetostatic coupling between the two ferromagnets. When the two ferromagnetic layers are aligned parallel, the resistance of the structure is low; when they are antiparallel, the resistance is high. The difference between high and low resistance in

GMR is typically a few ohms, representing tens of percent of the total resistance. The magnetoresistance ratio, MR, is defined by

$$MR = \frac{R_{AP} - R_P}{R_P}$$

where R_{AP} is the antiparallel high resistance and R_P is the parallel low resistance. The ability to fabricate uniform magnetic films near the single domain limit was crucial for the creation of spin valve technology. GMR spin valves were used for years in the recording heads of magnetic hard-disk drives [5–7]. GMR spin valves are still used as magnetic sensors for some applications [8]. Room temperature tunnel magnetoresistance (TMR) was discovered in 1994 by Moodera et al. [9]. The fabricated structures which use TMR are called magnetic tunnel junctions (MTJs). The advent of MTJ represented a significant improvement in spintronics from giant magnetoresistance (GMR) spin valves, with MR ratios in the hundreds of percent [10,11].

MTJs consist of two ferromagnets separated by a thin insulating layer through which electrical current tunnels, generating tunnel magnetoresistance (TMR). MTJs were first proposed by Michel Julliere in 1975 [12]. He looked at tunnelling between Fe and Co films separated by a thin layer of Ge at low temperature, 4.2 K. He observed a contrast in tunnelling conductance when the two ferromagnetic layers were aligned parallel versus antiparallel. The ability to reliably deposit clean, uniform insulators to act as tunnel barriers was one of the critical enabling technologies in the development of MTJs.

Both GMR and TMR devices work by switching the magnetization direction of one ferromagnetic layer, the free layer or recording layer, while the other ferromagnetic layer magnetization remains constant, the fixed layer or reference layer. In both GMR and TMR, differential resistance arises from the relative directions of the magnetic moments in the two ferromagnetic layers. When the two magnetic moments are aligned parallel, the resistance is low. When the moments are aligned antiparallel, the resistance is high. The use of TMR in MTJs results in a greater difference between parallel and antiparallel resistance compared to GMR spin valves due to the superior spin filtering of tunnel barriers using particular materials [13]. The resistance of the all-metal GMR spin valves is typically a few ohms with the difference in resistance states being 60-80% at room temperature using sputtered films [14–16]. Using the sputtered CoFeB/MgO/CoFeB material system, resistances of TMR devices can range from less than 1 kΩ to megaohms and differences between states typically greater than 100%, with record-setting devices achieving greater than 600% difference at room temperature [17–20].

1.2 Tunnel Magnetoresistance

Tunnel magnetoresistance is cause by the spin-dependent density of states of ferromagnetic metals. The magnetization direction of a ferromagnet defines a spin polarization axis for the electrons in the material. Ferromagnetic metals contain more electrons whose spins align to the local magnetization than electrons whose spins align in the opposite direction. These spin polarized electrons are said to be majority and minority spin carriers, respectively [21]. Since the insulating tunnel barrier supports potential gradients, applying a bias voltage across the junction raises the Fermi level of the one ferromagnet relative to the other. As shown in Figure 1-1, when the two ferromagnets are aligned parallel, the number of majority spin states available on the low energy side of the barrier is large enough to accept the majority spin carriers incident on the barrier from the high energy side. Thus, a large current flows across the barrier. If the ferromagnets are aligned antiparallel, the incident majority spin carriers must transmit across the tunnel barrier to occupy the minority spin states on the low energy side. The restricted number of available states results in a low current flow across the barrier.

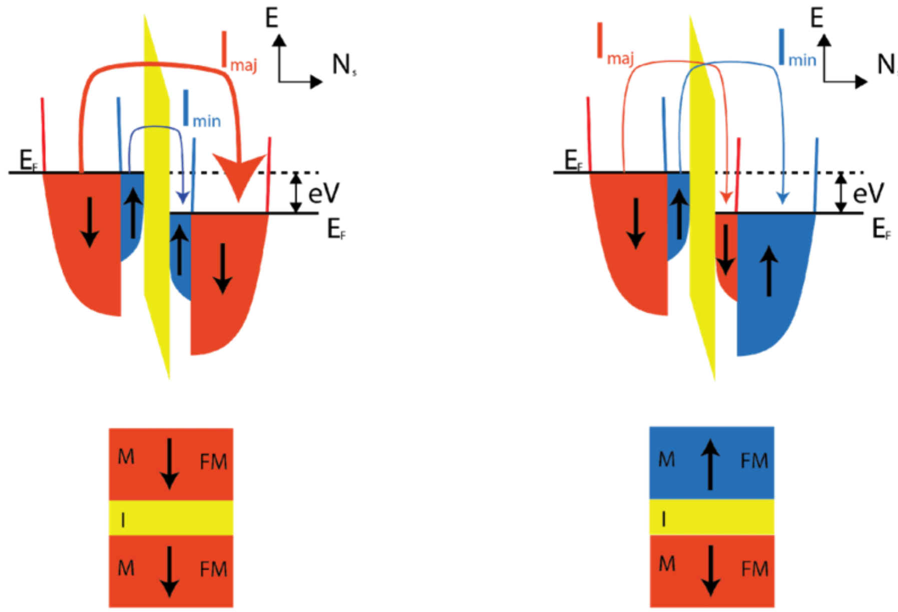

Figure 1-1. Tunnel magnetoresistance arises from the the population of majority and minority spin carriers on the incident side of the tunnel barrier relative to the opposite side of the barrier. When the ferromagnets are aligned parallel, the majority spin carriers from the incident side have many available states to occupy after tunneling, and thus the resistance is low. When the ferromagnets are antiparallel, the majority spin carriers have a small number of available states to tunnel into, and the resistance is high.

The relative number of majority and minority spin carriers in a ferromagnet are used to define the spin polarization, *P*, of the material by the equation

$$P = \frac{N_{maj} - N_{min}}{N_{maj} + N_{min}}$$

where N_{maj} is the number of majority spin carriers and N_{min} is the number of minority spin carriers [21]. The ratio of the difference between the high and low resistances across the MTJ to the low resistance is called the TMR ratio, or simply MR. It is related to the spin polarization of the ferromagnetic materials by the equation

$$MR = \frac{R_{AP} - R_P}{R_P} = \frac{2P_1P_2}{1 - P_1P_2}$$

where R_{AP} is the antiparallel resistance, R_P is the parallel resistance, P_1 is the spin polarization of the first ferromagnet, and P_2 is the spin polarization of the second ferromagnet [21].

1.3 Magnetic Anisotropy

The energy barrier to magnetization reversal is set by the magnetic anisotropy. The total magnetic anisotropy is made up of contributions from the magnetocrystalline, shape, and interfacial anisotropies. The magnetocrystalline anisotropy is an intrinsic energy density that arises from the spin-orbit coupling in transition metal ferromagnets. The form of the magnetocrystalline anisotropy depends upon the symmetry of the crystal. The most commonly known form is that of a uniaxial system, where the magnetocrystalline anisotropy, K_μ, can be approximated by

$$K_\mu \approx A(\sin\theta)^2$$

where A is a material specific expansion constant and θ is a small angle deviation from the magnetocrystalline easy axis [22]. A similar approximation can be made for more complex cases. For instance, in a cubic crystal the magnetocrystalline anisotropy can be approximated by expansion to second order as

$$K_\mu \approx A(\sin\theta\cos\theta)^2.$$

In the CoFeB films used as free layers in most MTJs, the magnetocrystalline anisotropy is negligible compared to the other sources of anisotropy [23].

Shape anisotropy describes the tendency of the magnetization to lie along the long direction of the ferromagnet. Shape anisotropy is summarized by the demagnetizing field, $\boldsymbol{H_d}$, by the equation

$$\overrightarrow{H_d} = -\begin{pmatrix} N_{xx} & N_{xy} & N_{xz} \\ N_{yx} & N_{yy} & N_{yz} \\ N_{zx} & N_{xzy} & N_{zz} \end{pmatrix}\begin{pmatrix} M_x \\ M_y \\ M_z \end{pmatrix}$$

where N_{ij} are the elements of the demagnetizing factor tensor and M_i are the components of the magnetization vector [22]. In an ellipsoidal magnetic particle, the easy axis of the demagnetizing field lies along the major axis. In a sphere, there is no demagnetizing field. In a circular disc, the demagnetizing factor tensor diagonalizes and $N_x+N_y+N_z=2N_x+N_z=4\pi$ [24].

Interfacial anisotropy is observed in magnetic films where the ferromagnetic layers are especially thin, usually less than 2 nm. Multilayer ferromagnets, such as CoPt, use many repeats of thin layers of Co and Pt to create a perpendicular magnetic moment using the Co 3d/Pt 5d orbital hybridization [25]. At a CoFeB/MgO interface, the hybridization of the Fe 3d orbitals and O 2p orbits causes a large interfacial anisotropy [26]. When the CoFeB thickness is less than 1.5 nm, a larger portion of the volume of the CoFeB is interface than is bulk, resulting in a magnetic easy axis perpendicular to the direction preferred by shape anisotropy. These perpendicular MTJs tend to have very large interfacial anisotropy and are of most interest for data storage. The magnitude of the interfacial anisotropy in the CoFeB/MgO/CoFeB system can be modified using an electric field, an effect called voltage controlled magnetic anisotropy (VCMA) [18,24]. This will be discussed later in Chapter 4.

The different types of anisotropy sum to a total effective anisotropy. The effective anisotropy, K_{eff}, multiplied by the ferromagnetic volume determines the intrinsic energy barrier to magnetization reversal for the ferromagnet. The effective anisotropy can also be thought of as an effective magnetic field, called the anisotropy field. In the uniaxial case, the anisotropy field magnitude, H_k, is defined by the equation

$$H_k = \frac{2K_{eff}}{M_S}$$

where M_S is the saturation magnetization of the ferromagnetic material. Magnetization reversal occurs due to an external magnetic field when the applied field exceeds the anisotropy field.

1.4 MTJ Film Design Considerations

To enable the manipulation of the resistance of the MTJ by external magnetic field, the fixed and free layers are engineered to have different coercivities, the amount of magnetic field required to reverse the magnetization [12,21]. The coercivity engineering may take the form of material selection, choosing a material with higher magnetic anisotropy for the fixed layer than the free layer, or by engineering combinations of layers to hold the fixed layer magnetization in the same direction. In Julliere's experiment, he chose Fe as his fixed layer and Co as his free layer for their different coercivities [12]. In most in-plane magnetized MTJs produced today, the fixed layer is held fixed by a synthetic antiferromagnet (SAF) that is in turn pinned by a field-annealed antiferromagnet. Figure 1-2 shows a typical in-plane MTJ structure, this particular film deposited by Everspin Technologies. In the MTJ film shown, the 50 nm thick Ta layer was used to seed the crystalline texture necessary to grow the PtMn film. The PtMn was the pinning antiferromagnet. After the deposition was complete, the film was annealed in a magnetic field to lock in the spins of the high anisotropy, antiferromagnetic PtMn. The uncompensated edge spins of the PtMn pinned the CoFe layer directly above it via exchange bias [27,28]. The 0.8 nm Ru spacer ensures the 2 nm CoFe and the 3 nm CoFe were antiferromagnetically coupled, thus creating the SAF. The 1 nm MgO was chosen as the tunnel barrier because of the high MR in the CoFe/MgO/CoFeB system [13,17]. CoFeB was chosen for its low intrinsic magnetic anisotropy which enabled study focused on shape anisotropy. The 10 nm Ta acted as a boron getter in the annealing process. The Pt cap acted as a conductive top electrode and protected the Ta and CoFeB layers from oxidation.

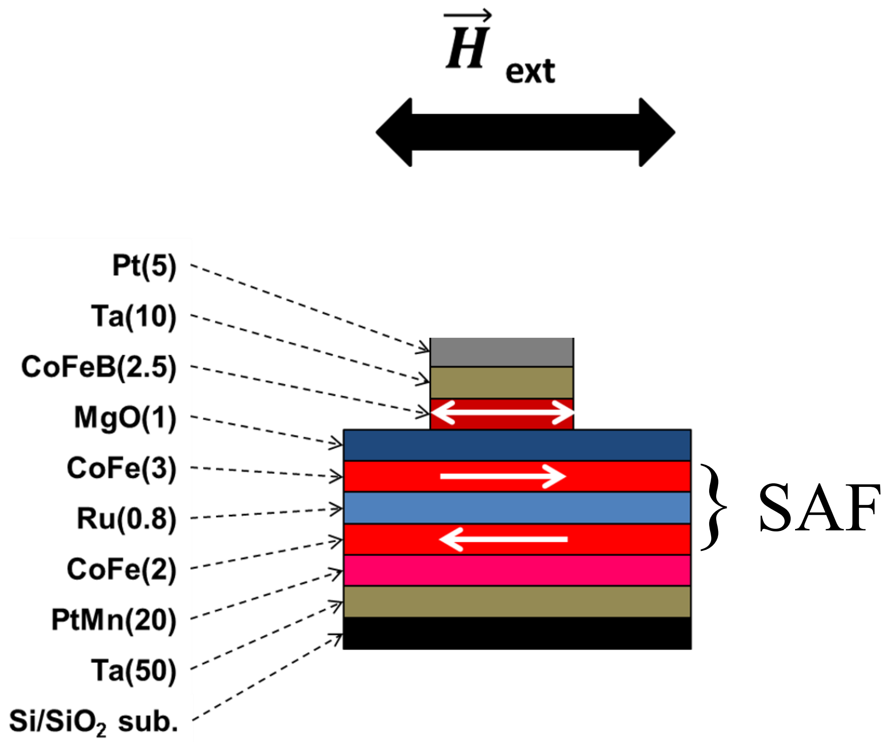

Figure 1-2. A typical in-plane magnetized MTJ uses a synthetic antiferromagnet pinned by a field annealed antiferromagnet as the fixed layer to keep the coercivities of the fixed and free layers well separated. The numbers in parentheses denote the layer thicknesses in nanometers. Figure modified from [29]**.**

The desired control mechanism also plays a role in the design of the MTJ films. If spin orbit torque (discussed in the next chapter) control is desired, a heavy metal, such as Ta or Pt, lead must be placed directly above or below the ferromagnetic free layer. Since the processes used to pattern the MTJ pillars involve etching from the top, the film is deposited with the free layer on the bottom of the tunnel barrier with a heavy metal just below that. The entire structure then needs to be inverted. Figure 1-3 shows an example of one such MTJ film. The pinning antiferromagnet, in this case a new and intriguing material for the task, IrMn, and SAF must all be patterned in the fabrication of the MTJ pillar.

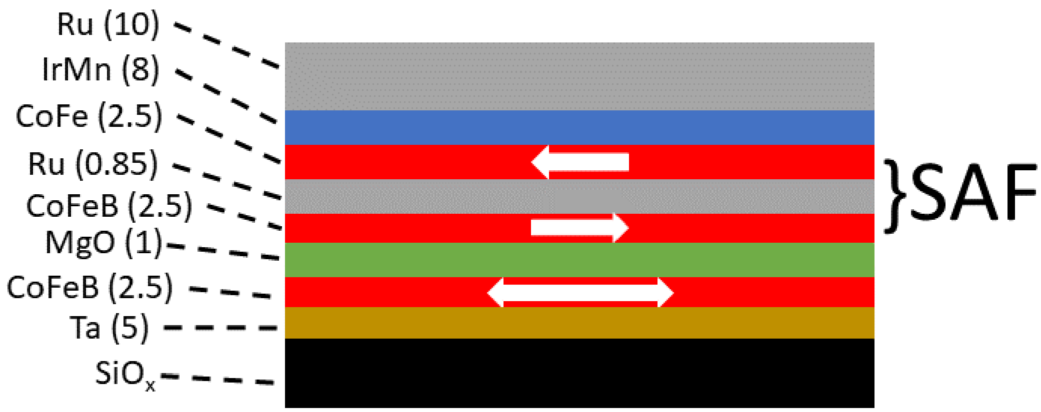

Figure 1-3. When SOT control is desired, the MTJ structure must be inverted so that the free layer is on the bottom next to the Ta lead material. This film sample was deposited by Xixang Zhang's group at King Abdullah University of Science and Technology at our request.

Perpendicular MTJs use interface anisotropy to control the coercivity of the fixed and free layers. When the CoFeB layers in a perpendicular MTJ become thinner, the interface anisotropy becomes greater [30]. A typical perpendicular MTJ has a 0.8-1.3 nm thick CoFeB fixed layer and a 1.5-1.6 nm thick CoFeB free layer [24,31]. The fixed CoFeB may have a coercivity as high as 14.3 kOe [32]. The free layer coercivity ranges from less than 50 Oe to about 225 Oe [19]. Figure 1-4 shows a typical perpendicular CoFeB MTJ. The bottom Ta layer acts as an adhesion layer for the subsequent metal layers above. The 10 nm Ru layer seeds the crystalline texture for the layers above and improves roughness. The next Ta acts as a boron getter when the film is annealed. The 0.85 nm CoFeB is the fixed layer in the MTJ. The less than nanometer thickness gives the fixed layer a very high interfacial anisotropy. The 1.5 nm MgO acts as the tunnel barrier, with a resistance in the megaohm range. The top CoFeB is the free layer. The 1.5 nm thickness of the free layer puts it near the edge of perpendicular anisotropy, thus separating its coercive field from that of the fixed layer. The Ta layer above is the boron getter for the free layer. The Ru cap acts as the top electrical contact. Ruthenium oxide is metallic, making Ru a good choice for an electrode in MTJ pillars that will be exposed to atmosphere.

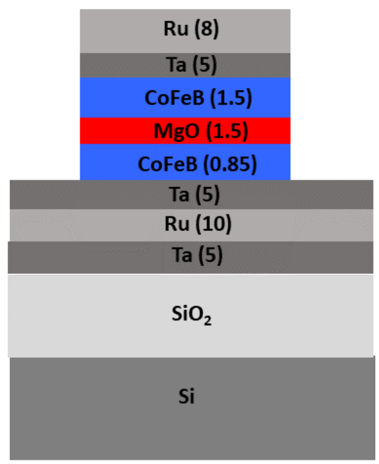

Figure 1-4. A typical perpendicular CoFeB MTJ uses thinner ferromagnetic layers than the in-plane case. The thinner CoFeB is dominated by interfacial, rather than shape, anisotropy. The numbers in parentheses indicate the thickness in nanometers.

Figure 1-5 shows resistance versus magnetic field loop for a perpendicular MTJ. The field toggled the free layer magnetization between parallel and antiparallel to the fixed layer. The field at which the magnetization switches is called the switching field. The average of the two switching fields, the center of the loop, is the field magnetostatic field at the free layer caused by the fixed layer. The difference between the loop center and the switching field is the coercivity. The magnetic field switches of in-plane MTJs usually look very similar to Figure 1-5 as well.

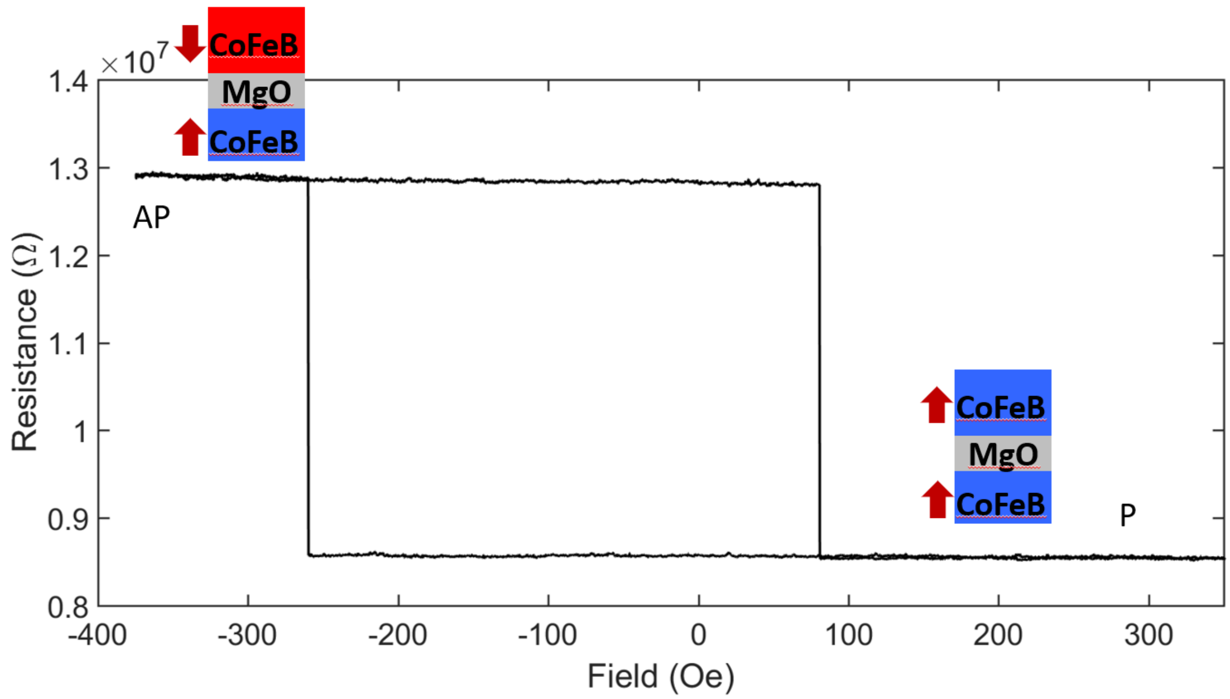

Figure 1-5. A resistance vs applied magnetic field loop toggles the free layer magnetization between parallel and antiparallel to the fixed layer.

1.5 Superparamagnetic MTJs

The stochastic, thermal reversal of magnetization was once a phenomenon to be avoided, particularly when designing magnetic data storage devices [33], [34]. High thermal stability magnetization was preferred for long-term data storage, though the retention time was balanced with write error rate [35]. The advent of magnetic random-access memory (MRAM) necessitated an even more nuanced approach to thermal stability as write times and energy both needed to be minimized for working memory operation [36], with write times now in the 1-10 ns range while maintaining 60-100 k_BT energy barriers [37]. Recent interest in stochastic computing has renewed interest in superparamagnetism as a source of random fluctuations [18,38–42].

Superparamagnetic particles were first defined by Bean in 1955 as "those particles that are so small that, in addition to containing but one domain, the thermal energy at the temperature of the experiment is sufficient to equilibrate the magnetization of an assembly in a time short compared with that of the experiment." [43] Superparamagnetism is a phenomenon that occurs when the temperature of magnetic particles small enough to be monodomain is high enough so that the magnetization equilibrates on timescales that are short compared to the magnetization measurement [44]. In other words, the energy barrier to changes in the magnetization direction is no longer large compared to the thermal energy. When the energy barrier is sufficiently small, thermal fluctuations dominate the magnetization dynamics [45]. Thermal fluctuations of magnetization had already been described [45], but the maintenance of instantaneous long-range magnetic order—the particle remains monodomain—was notable enough create a new classification of behavior [43]. The details of the transient dynamics of low thermal stability magnetic particles were later studied and the statistics of stochastic processes applied [33,46]. The different magnetic configurations have different energies, owing to the intrinsic magnetic anisotropy, shape anisotropy, interface anisotropy, local magnetic fields, exchange bias, spin transfer torque, or spin orbit torque [22,27,28,47–51]. Integration over the thermodynamic partition function of the MTJ can be used to describe the average population statistics, or probability at any given time, of a given magnetic configuration [52–54]. This magnetic particle description was eventually applied to patterned magnetic thin films [55]. Figure 1-6 shows the energy barrier model described above applied to an MTJ. For magnetic nanoparticles, the external input is magnetic field. In MTJs, it can be done using electronic means such as spin transfer torque and spin orbit torque [47–49,56–58]. A common figure of merit for the thermal stability of a magnetic tunnel junction is the thermal stability factor, Δ, defined by the equation

$$\Delta = \frac{E_b}{\mathrm{k_B} T} = \frac{K_{eff} V}{\mathrm{k_B} T}$$

where E_b is the energy barrier to magnetization reversal, $\mathrm{k_B}$ is Boltzmann's constant, T is the temperature, K_{eff} is the effective anisotropy, the sum of the anisotropies discussed earlier, and V is the ferromagnetic volume [29,32,59,60].

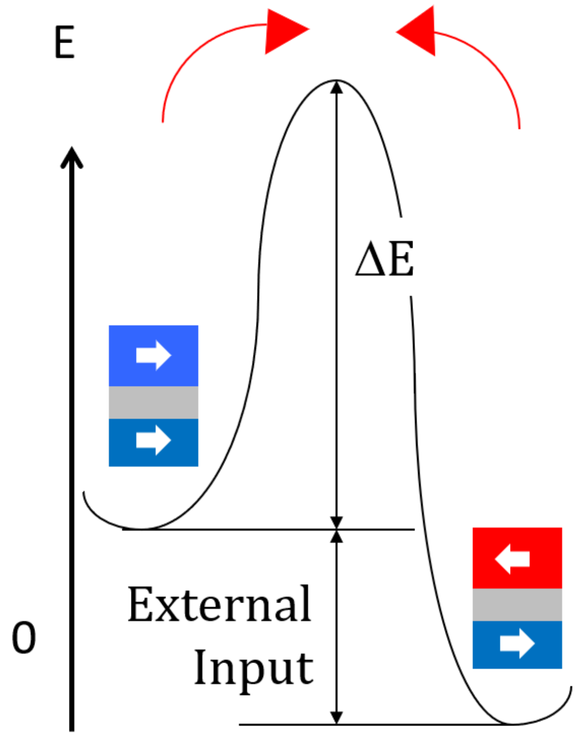

Figure 1-6. The energy of an MTJ with uniaxial anisotropy in the superparamagnetic regime consists of two metastable local minima with a barrier between them. The relative energy of the two local minima can be manipulated by external inputs. For magnetic nanoparticles, the external input is magnetic field. In MTJs, it can be done using electronic means.

1.6 Random Telegraph Noise

The superparamagnetic particle description can be extended to patterned thin films, with the patterned island of ferromagnetic material now acting as the particle [55]. The electronic signature of a uniaxial superparamagnetic spintronic device was first measured in giant magnetoresistance (GMR) recording heads, and it resembled a type of noise found in other electronic systems called random telegraph noise (RTN) [7,61]. In random telegraph noise, the signal randomly fluctuates between two levels, resembling the anharmonic off/on signal of a telegraph. When the random telegraph noise is produced by magnetization reversal, the signal switching is Poisson process. The more time that elapses since the previous switching event, the more likely a switch will occur. Figure 1-7 shows RTN from an MTJ that was not intended to be superparamagnetic but rather was meant to represent a size reduction of stable MTJs. The preference of the RTN for the high and low states was controllable using the external magnetic field. In Figure 1-7a, the device prefers the antiparallel state with the larger applied magnetic field. In Figure 1-7b, the device prefers the parallel state at lower applied field.

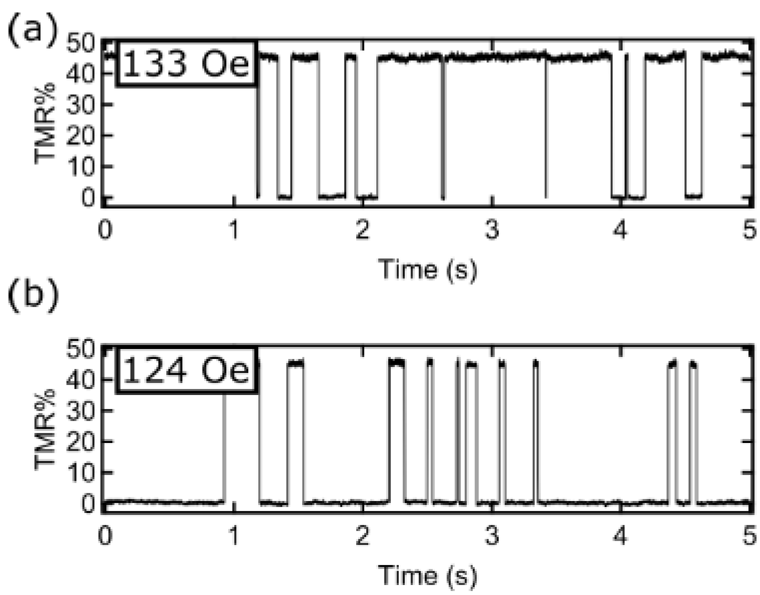

Figure 1-7. As the size of MTJs becomes smaller, random telegraph noise becomes a part of their electronic output signal. Figure taken from [62].

When MTJs intended for data storage become small enough, they become superparamagnetic and output RTN, making them useless for their intended purpose [63]. However, applications like stochastic computing utilize RTN to perform novel computing applications [38,40,64,65]. When MTJs are engineered for low thermal stability, and thus rapid RTN, the dwell time of the magnetic moment along either direction of the easy axis can be quickly reduced from the many years of data storage devices to nanoseconds [36,66,67]. Figure 1-8 shows a recent result in which thermal magnetic reversal occurred on nanosecond timescales [67]. Hayakawa et al. used CoFeB (2.4 nm)/MgO/CoFeB (2.2 nm) MTJ films to fabricate in-plane devices that exhibited magnetization dwell times as short as 8 ns, breaking the previous record of 980 ns [20]. With these dwell times, stochastically switching MTJs are approaching the theoretical characteristics proposed for stochastic computing devices [38].

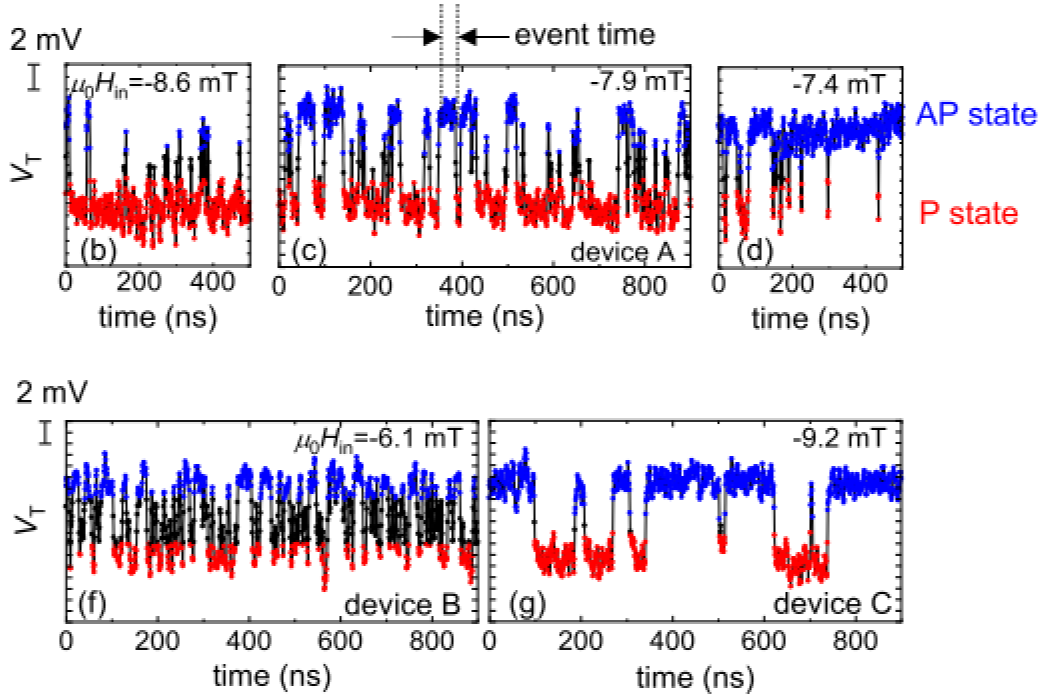

Figure 1-8. Nanosecond timescale magnetization reversal was recently observed in CoFeB/MgO/CoFeB in-plane MTJs. The field values in the top right indicate the in-plane magnetic field that was externally applied to cancel the magnetostatic coupling between the fixed layer and the free layer. Figure taken from [67]**.**

Chapter 2 Spin Transfer Torque and Spin Orbit Torque

In this chapter, I explain the two most common electronic methods of controlling magnetization direction: spin transfer torque and spin orbit torque. Both of these control mechanisms are used throughout the subsequent chapters. I introduce a simple model for understanding both control mechanisms and compare their efficiencies.

2.1 Electronic Control of Magnetization

Magnetic structures can be manipulated by magnetic fields as described in Chapter 1. Inductive coils were once the read/write technology for magnetic data storage. Toggle magnetic random access memory (MRAM) uses magnetic field to write MTJs [68]. However, magnetic fields are difficult to confine to individual MTJs, particularly as the density of devices on a chip becomes commercially relevant. To create working spin electronics, or spintronics, an electronic means of controlling the magnetization direction is required. While there are some novel electric field mechanisms using multiferroics, the most common mechanisms are spin transfer torque (STT) and spin orbit torque (SOT) [47–49,58,69]. Both methods use large current densities, typically greater than 10^6 A/cm^2, to transfer spin angular momentum to the free layer ferromagnet in an MTJ [36,47,70,71]. The application of STT or SOT can be used to reverse the magnetization direction of an isolated ferromagnet, but combining these mechanisms with magnetic tunnel junctions provides a convenient means of reading the free layer state.

To understand STT and SOT, it is important to the different types of electron currents that are involved in these two mechanisms. Figure 2-1 shows the different types of currents with the electrons shown as green circles containing black arrows to indicate their spin direction. Figure 2-1a is an unpolarized charge current in which the electron spins point in random directions and sum to zero. Figure 2-1b is an ideally polarized electron current where all the electron spins point in the same direction. Figure 2-1c is a more realistic spin polarized current with majority and minority carriers. The spins all lie along the same polarization axis, but some point in the opposite direction of the majority. Figure 2-1d shows a pure spin current wherein there is no net charge current in the lateral direction, but electrons with opposite spin flow in opposite lateral directions while the charge current flows in the third dimension.

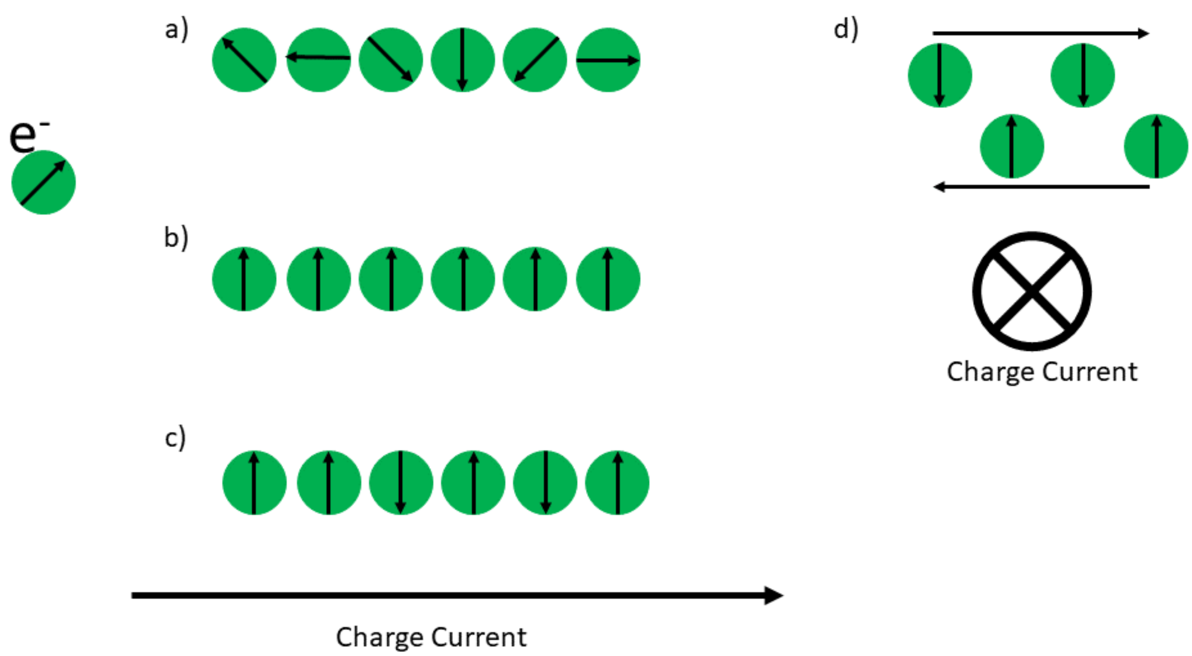

Figure 2-1. The different types of currents in spintronic devices are unpolarized (a), uniformly polarized (b), polarized with majority and minority carriers (c), and pure spin current (d).

2.2 Spin Transfer Torque Switching

Berger and Slonczewski described how spin polarized current could be used to control the magnetization direction of ferromagnets in 1996 [47,48]. STT control uses two-terminal MTJs with the same read and write paths. STT uses bidirectional current depending on whether the intended switch is antiparallel (AP) to parallel (P) or P to AP. First, the two types of STT switch will be described using a simple model. For the AP to P switch, positive bias is applied on the side of the free layer. Electron current flows from the fixed layer to the free layer with the tunnel barrier acting as a spin filter. The electrons become spin polarized when they encounter the fixed layer ferromagnet, with the polarization axis lying along the magnetization direction. As discussed in Chapter 1, there are majority and minority spin carriers. The majority spin carriers from the fixed layer cross the tunnel barrier to fill the minority spin carrier states in the free layer. When the Fermi level is raised high enough, meaning a large enough electric potential is applied, an excess of fixed layer majority spin carriers cross to the free layer. There, the excess spin carriers are re-polarized to the local magnetization. The torque applied to the spin carrier to change its spin angular momentum also acts upon the free layer magnetization in an equal and opposite fashion [71]. The spin angular momentum transferred to the free layer magnetization reverses the magnetization direction when the charge current density flowing through the MTJ exceeds the critical current density [72]. Figure 2-2 shows a schematic representation of the AP to P STT switch.

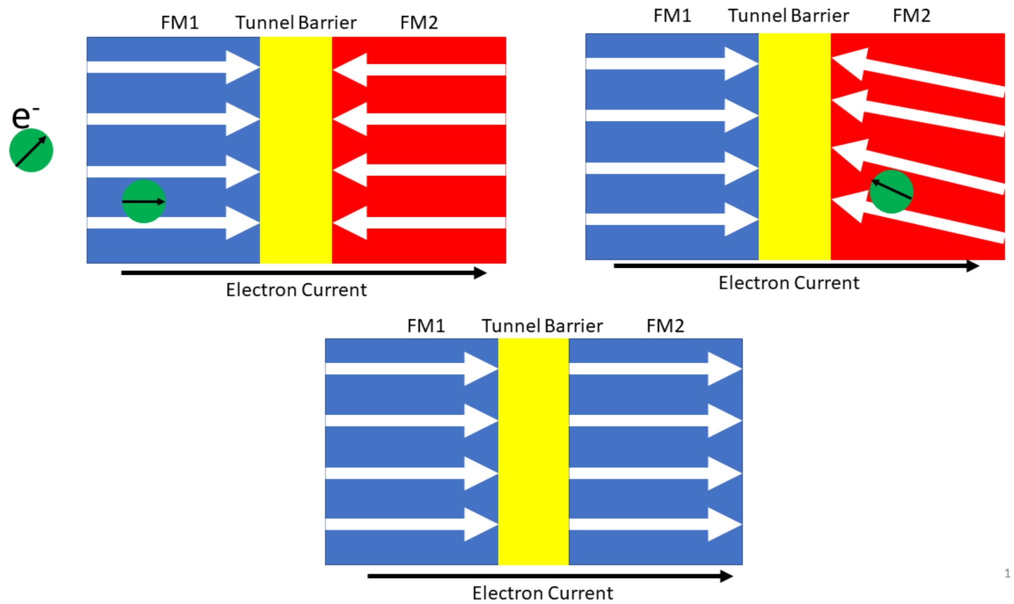

Figure 2-2. Spin transfer torque switches the free layer magnetization direction by conservation of angular momentum. For the antiparallel to parallel switch, the incoherent electron current becomes spin polarized by the local magnetization in the first ferromagnet, FM1. After crossing the tunnel barrier, the electron once again becomes spin polarized by the second ferromagnet. The torque by which the second ferromagnet acts upon the electron current also causes an equal and opposite torque on the ferromagnet.

To perform the reverse switch, P to AP, the direction of the electron current is reversed. The electrons first encounter the free layer magnetization and become spin polarized. The majority spin carriers tunnel across the tunnel barrier and continue through the circuit. Some of the minority spin carriers are scattered and reflected by the tunnel barrier, resulting in an over-density of minority spin carriers in the free layer. The excess minority carriers re-polarize and become majority carriers. As with the AP to P switch, the transfer of spin angular momentum to the free layer magnetization results in magnetization reversal when the charge current density exceeds the critical value. Figure 2-3 shows a model of the P to AP switch.

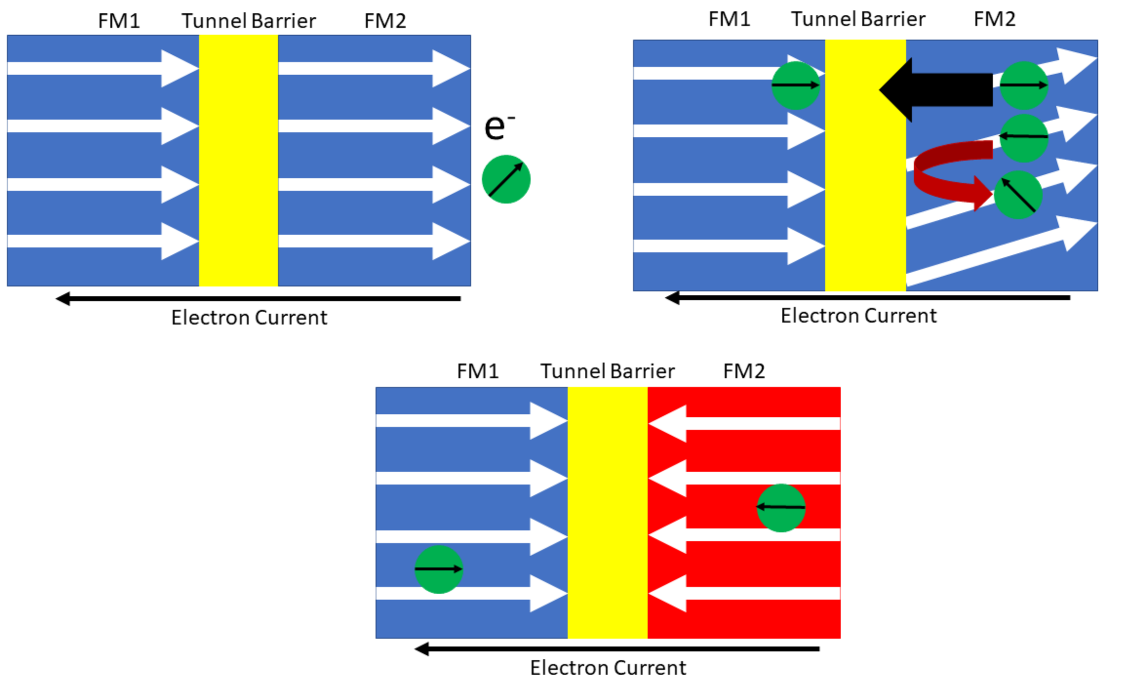

Figure 2-3. The parallel to antiparallel switch uses the spin angular momentum of the reflected minority spin carriers to switch the free layer magnetization. The reflected minority carriers exceed the available minority spin states and re-polarize to the local magnetization. This causes a torque on both the electron spin and the local magnetization as in the antiparallel to parallel case.

The critical current density for the P to AP switch is typically greater than that for the AP to P switch [71,73]. The critical current density to switch a ferromagnet using STT, J_C, can be estimated by

$$J_C = \frac{2\alpha e M_s t}{\hbar P} H_{eff}$$

Where α is the material damping constant, e is the electron charge, M_S is the saturation magnetization, t is the thickness of the ferromagnetic layer, P is the spin polarization, and H_{eff} is the effective magnetic field acting on the free layer, including the demagnetizing field described in section 1.3. In the model described above, the spin polarization is greater in the AP to P switch than the P to AP switch, leading to the difference in critical switching current density.

In terms of the Landau-Lifshitz-Gilbert (LLG) equation, the magnetization dynamics without STT current are described by

$$\frac{\partial \boldsymbol{m}}{\partial t} = -\gamma\, \boldsymbol{m} \times \boldsymbol{H_{eff}} + \alpha \boldsymbol{m} \times \frac{\partial \boldsymbol{m}}{\partial t}$$

where $\boldsymbol{m}$ is the free layer magnetic moment normalized by the saturation magnetization, γ is the gyromagnetic ratio, $\boldsymbol{H_{eff}}$ is the effective magnetic field, the sum of the anisotropy field and any external magnetic fields, and α is the material damping constant. The STT term is added to the LLG equation, taking the form

$$-\gamma \frac{\hbar P}{2e} \frac{J_c}{M_s t} \left(\boldsymbol{m} \times \left(\boldsymbol{m} \times \boldsymbol{m_{fxd}} \right) \right)$$

where $\hbar$ is the reduced Planck's constant, P is the spin polarization in the material, defined in section 1.2, e is the electron charge, J_c is the critical switching current, M_S is the saturation magnetization, t is the film thickness, and $\boldsymbol{m_{fxd}}$ is the normalized fixed layer magnetic moment [71]. Note that when $\boldsymbol{m}$ and $\boldsymbol{m_{fxd}}$ are parallel, the STT term is zero. In that case, thermal noise is required to excite the free layer moment out of alignment.

Another approach could be to use small magnetic fields to keep the free layer from completely aligning with the fixed layer.

STT controlled MTJs are currently in production as MRAM [66,74]. Reduction of the critical current density for STT switching is still a topic of ongoing research [70]. Control of the average magnetic state of a superparamagnetic MTJ has been demonstrated, enabling the use of STT for novel computing applications [20,29,38,39]. STT switching experiments involving superparamagnetic MTJs will be discussed in Chapter 5-7.

The large current density of more than 10^6 A/cm^2 is driven across the insulating tunnel barrier to switch the free layer magnetization direction [36,47,49,70]. This leads to Joule heating of the tunnel junction that is linear in the tunnel current [75]. Heating the MTJ results in a larger denominator in the thermal stability factor described in section 1.5, in turn decreasing the energy input required to reverse the magnetization. Driving the large STT switching current across the tunnel barrier also degrades the tunnel barrier, eventually leading to dielectric breakdown [36]. SOT avoids this problem by driving the large current density through all-metal leads.

2.3 Spin Orbit Torque Switching

SOT control requires three-terminal devices, as the read and write paths are separated but use a common ground. By using an all-metal write path, SOT avoids the power dissipation of driving a large current over a high resistance tunnel barrier. Since the tunnel barrier in an SOT device is subject only the smaller read bias voltage, the longevity of SOT devices is much greater than STT devices. These advantages come at the cost of greater complexity in fabricating the device leads.

SOT is believed to arise from the Rashba effect [57] or the spin Hall effect [56,76]. For both effects, spin orbit coupling in high atomic number metals causes differential scattering of electrons according to their spin [56,57,76]. The spin-orbit coupling term of the Hamiltonian for these electrons, H_{SO}, is described approximately by the equation

$$H_{SO} = \frac{\hbar}{2mc^2}(\nabla V \times \boldsymbol{p}) \cdot \boldsymbol{\sigma}$$

in where m is the mass of the electron, c is the speed of light, $\hbar$ is the reduced Planck's constant, V is the spherical atomic potential, $\boldsymbol{p}$ is the momentum operator, and $\boldsymbol{\sigma}$ is the vector of Pauli spin matrices [76]. From the spin orbit coupling Hamiltonian, both the Rashba and spin Hall effects are predicted. Figure 2-4 shows the effects of this Hamiltonian. Using the Rashba description, the electron flowing through the radial potential at the surfaces of the lead experiences the atomic electric field as a magnetic field in its rest frame. This causes the electrons in the surface states to align their spin to the magnetic field. In the spin Hall effect case, as an electron flowing in the direction of the electron current, opposite the direction of $\boldsymbol{J_C}$, encounters the radial potential V, it is scattered upward or downward if its spin lies in the plane of the lead. If the spin lies along the direction perpendicular to the plane, it is scattered left or right.

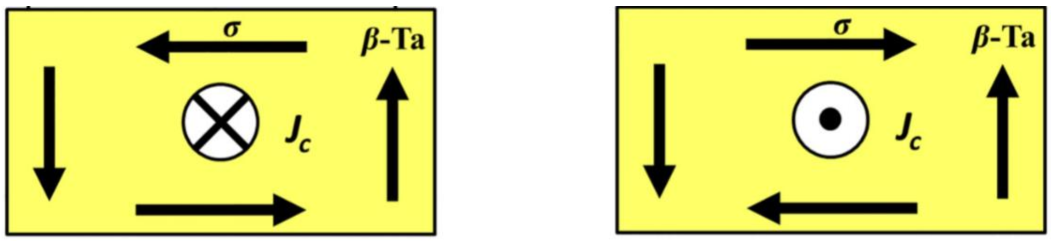

Figure 2-4. Spin orbit torque switching uses a charge current passing through a heavy metal layer adjacent to the ferromagnet. The spin orbit interaction between the charge current and the high atomic number metal leads to spin-dependent scattering, with the polarization axis perpendicular to the charge current direction. Figure adapted from [32]**.**

2.4 Rashba Effect

The Rashba effect was discovered by Rashba and Sheka in 1959 [77]. The effect as originally described explained the splitting of spin bands based on electron momentum in bulk crystals. It was reduced to two dimensions by Bychkov in 1983 [78]. In terms of SOT, the Rashba effect is an interface effect that generates non-equilibrium spin densities in the metallic surface states [57]. Due to relativistic effects, an electron moving in the plane of a two-dimensional electron gas in a perpendicular electric field generates a magnetic field in the rest frame of the electron. The Hamiltonian of that magnetic field acting on the spin of the electron takes the form

$$H = \alpha_R(\boldsymbol{e_z} \times \boldsymbol{k_B}) \cdot \boldsymbol{s}$$

where α_R is the Rashba parameter, $\boldsymbol{e_z}$ is the direction of the electric field, $\boldsymbol{k_B}$ is the Bloch vector, and $\boldsymbol{s}$ is the electron spin. The Rashba parameter can be expressed as a function of the atomic number of the surface material and another parameter describing the asymmetry of the wave function [57]. The spins accumulate at the surface of the heavy metal in the 2DEG, and do not move into the ferromagnet. These spin densities act on the adjacent ferromagnet through the exchange interaction, constituting an effective field. It is as if the 2DEG temporarily magnetizes. The use of surface spin densities and the exchange interaction makes the Rashba effect very short-ranged.

2.5 Spin Hall Effect

The spin Hall effect (SHE) was first described by Hirsch in 1999 [56]. The spin Hall effect is a bulk effect that generates a pure spin current in the perpendicular directions, with the spin polarization axis lying along the third perpendicular direction [56,76]. Electrons with opposite spins flow in opposite directions perpendicular to the charge current direction resulting in a net spin current yet no net perpendicular charge current. The spin current density, $\boldsymbol{J_\sigma}$, is given by

$$\boldsymbol{J_\sigma} = \frac{e^2 k_F^3}{6\pi^2}\left(\frac{\tau_\sigma}{m}\boldsymbol{E} + \alpha \boldsymbol{E} \times \boldsymbol{\sigma}\right)$$

where e is the electron charge, k_F is the wavenumber associated with the Fermi velocity, τ_σ is the electron relaxation time, $\boldsymbol{E}$ is the electric field, α is the material damping parameter, and $\boldsymbol{\sigma}$ is again the vector of Pauli spin matrices [76]. This can be expressed in a simpler form as

$$\boldsymbol{J_\sigma} = \vartheta_{SH}(\boldsymbol{J_c} \times \boldsymbol{\sigma})$$

where θ_{SH} is the spin Hall angle, the ratio of spin current to charge current generated in the material. The spin Hall angle sign and magnitude depends upon the material. For instance, the spin Hall angle of Pt is typically reported as about 0.07 while for Ta it is -0.12 to -0.15.

The sign of the spin Hall angle indicates that the spin up and spin down electrons move in opposite directions in these two materials for the same direction of charge current. The spin current can flow into an adjacent ferromagnet and exert a torque on the magnetization. This adds a term to the LLG equation taking the form

$$-\gamma \frac{\hbar}{2e} \frac{\vartheta_{SH} J_c}{M_s t} \left(\boldsymbol{m} \times (\boldsymbol{m} \times \boldsymbol{\sigma})\right).$$

Note that the direction of this term is parallel to the spin, $\boldsymbol{\sigma}$ [79]. This means that an in-plane magnetized MTJ can be switched using only SOT. Perpendicular MTJs require an in-plane magnetic field to break the rotational symmetry of the torque [32,58]. Figure 2-5 shows the use of an in-plane field to provide the necessary torque to continue the magnetization switch to the perpendicular directions after SOT brings it into the plane.

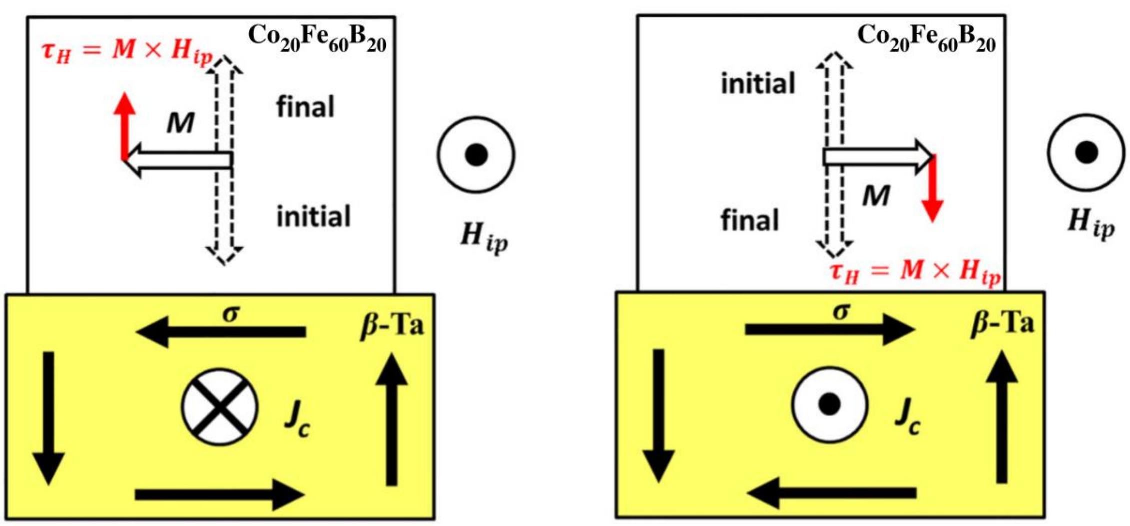

Figure 2-5. An in-plane magnetic field is required to contribute to SOT switching of perpendicular MTJs. The field applied along the direction of the charge current helps continue the switching of the magnetization once the SOT brings it in plane. Figure adapted from [32].

The spin current decoheres over the spin coherence length, which is set by the material and is normally a few nanometers [80,81]. This makes the spin Hall effect short-ranged except for in certain materials with long spin diffusion lengths. One potential experiment to separate the effects of the Rashba and spin Hall effects would be to use a long spin diffusion length material, such as copper, as a spacer between the heavy metal leads and the ferromagnet to be switched. Whether SOT comes from the Rashba effect or the spin Hall effect, or a combination of the two, SOT can be used to switch a ferromagnet adjacent to a high atomic number metallic lead [32,58,82]. SOT switching of a perpendicular MTJ will be discussed in Chapter 3 and an in-plane MTJ in Chapter 6.

2.6 STT vs SOT Efficiency

For in-plane magnetized MTJs switching from antiparallel to parallel, the STT and SHE terms in the LLG equation are practically identical. The fixed layer magnetization in the STT case points in the same direction as the polarization of the spin current in the SHE case. The differences are in the efficiency factors, P vs θ_{SH}, and the magnitude of the critical currents, J_c. The spin polarization factor, P, in an STT device can be estimated from the MR ratio as described in section 1.2. Since in-plane MTJs often use the same materials and same thicknesses for both the fixed and free layers, assume the spin polarizations in both layers are identical. For a typical MR of 100%, the spin polarization factor is about 0.58, or about four times the spin Hall angle of Ta. For the device discussed later in Chapter 6 where STT and SOT switching are compared, the MR is about 0.035 and the spin polarization is 0.13, or approximately equal to the spin

Hall angle of Ta. The magnitude of the critical current for STT switching should therefore be equal to that for SOT switching. The high resistance of the MTJ tunnel barrier that must be crossed by large currents in STT compared to the heavy metal leads which support the large currents in SOT is detrimental to the energy efficiency of STT-controlled MTJs if not the spin torque efficiency.

SOT exceeds STT spin torque efficiency in perpendicular MTJs. The LLG equation for a perpendicular MTJ still has the vanishing STT term in the absence of a thermal excitation to make the cross product nonzero. SOT has the advantage of beginning at the maximum of its cross product with the free layer magnetization. Consider a 20 nm x 1.5 nm circular disc of perpendicular $Co_{40}Fe_{40}B_{20}$ where the subscript numbers indicate the alloy composition in mass percent. The magnetic free layer has a volume of 4.71x10^{-19} cm^3. Ignoring strain effects, the lattice constant of CoFeB is about 0.285 nm, so the free layer contains approximately 2x10^4 atoms, 8.1x10^3 atoms each Co and Fe [83]. Fe and Co have magnetic moments of 2.2 and 1.7 Bohr magnetons per atom, respectively [84]. Thus, the free layer has a moment of 3.16x10^4 μ_B. Now consider a 10 ns pulse of spin polarized charge current used to reverse this free layer using STT. Using the LLG equation with STT

$$\frac{\partial \boldsymbol{m}}{\partial t} = -\gamma\, \boldsymbol{m} \times \boldsymbol{H_{eff}} + \alpha \boldsymbol{m} \times \frac{\partial \boldsymbol{m}}{\partial t} - \gamma \frac{\hbar P}{2e} \frac{J_c}{M_s t} \left(\boldsymbol{m} \times \left(\boldsymbol{m} \times \boldsymbol{m_{fxd}} \right) \right)$$

and assuming a 100% TMR, P=0.577, γ=3.1 MHz/Oe, $\boldsymbol{H_{eff}}$=40 Oe, α=0.01, M_S=800 emu/cm^3, $\boldsymbol{m_{fxd}}=-\boldsymbol{m}$, and a 0.1 radian thermal excitation to the free layer magnetization then J_c^{STT}=2.53x10^6 A/cm^2. The SOT current density takes the same form but replaces the 0.1

radian excitation with a factor of 1, because the spin polarization is now perpendicular to the free layer magnetization. However, replacing the spin polarization of 1 with a spin Hall angle of -0.15 tempers this advantage. This yields an SOT critical current density of 9.7×10^5 A/cm^2, 38% of the STT critical current density.

Chapter 3 Spin Orbit Torque Switching of High Thermal Stability Magnetic Tunnel Junction

In this chapter, I present a result using SOT to switch a very high thermal stability MTJ. This work was done when I was a junior graduate student working with Mukund Bapna. I performed the nanofabrication for this device using a process developed by Sam Oberdick. I also fabricated the means to connect the pulse generator to the SOT leads. This result was the smallest MTJ switched using SOT at the time of publication. This work was publish in Phys. Rev. Applied [32].

3.1 Background

Magnetic tunnel junctions (MTJs) are currently in use in magnetic random access memory (MRAM) and are proposed for specialized logic applications [36,39,85–89]. The resistance state of MTJs has been controlled using external magnetic field, spin transfer torque (STT), and electric field [18,37,47,48,71,90–92]. Another promising control mechanism is spin orbit torque (SOT) [50,56,57,76,93]. SOT occurs when charge current passes through a conductor with large spin orbit coupling and results in an accumulation of spins perpendicular to the charge current [56,57]. SOT may have energy efficiency advantages over external magnetic field and STT control as well as advantages in device longevity over STT.

SOT is believed to arise from the Rashba effect [57] or the spin Hall effect [56,76]. For both effects, spin orbit coupling in high atomic number metals causes differential scattering of electrons according to their spin [56,57,76]. The spin-orbit coupling term of the Hamiltonian for these surface states, H_{SO}, is described approximately by the equation

$$H_{SO} = \frac{\hbar}{2mc^2}(\nabla V \times \vec{p}) \cdot \vec{\sigma}$$

in where m is the mass of the electron, c is the speed of light, $\hbar$ is the reduced Planck's constant, V is the potential, $\vec{p}$ is the momentum operator, and $\vec{\sigma}$ is the vector of Pauli spin matrices [76]. From this Hamiltonian, the two different effects are predicted. Whether it comes from the Rashba effect or the spin Hall effect, or a combination of the two, SOT can be used to switch a ferromagnet adjacent to a high atomic number metallic lead [58,82].

The Rashba effect is an interface effect that generates non-equilibrium spin densities in the metallic surface states [57]. The spins accumulate at the surface of the heavy metal, and do not move into the ferromagnet. These spin densities act on the adjacent ferromagnet through the exchange interaction, constituting an effective field. The use of surface spin densities and the exchange interaction makes the Rashba effect very short-ranged.

The spin Hall effect is a bulk effect that generates a pure spin current in the perpendicular directions, with the spin polarization axis lying along the third perpendicular direction [56,76]. -This spin current decoheres over the spin coherence length, which is set by the material and is normally a few nanometers [80,81]. This makes the spin Hall effect short-ranged except for certain materials with long spin diffusion lengths.

Reversing a perpendicular-to-plane magnetization using SOT requires an in-plane magnetic field [58,94]. Experiments touting field-free switching simply substituted an external field for an effective field from exchange bias [95]. As shown in Figure 3-1, the in-plane field, H_{ip}, is essential to the generation of the torque that reverses the magnetization. The in-plane field here is constant, so it can be generated by exchange bias [95], magnetostatic interaction, or even field-like STT current [96]. SOT offers other advantages over STT or magnetic field switching as well.

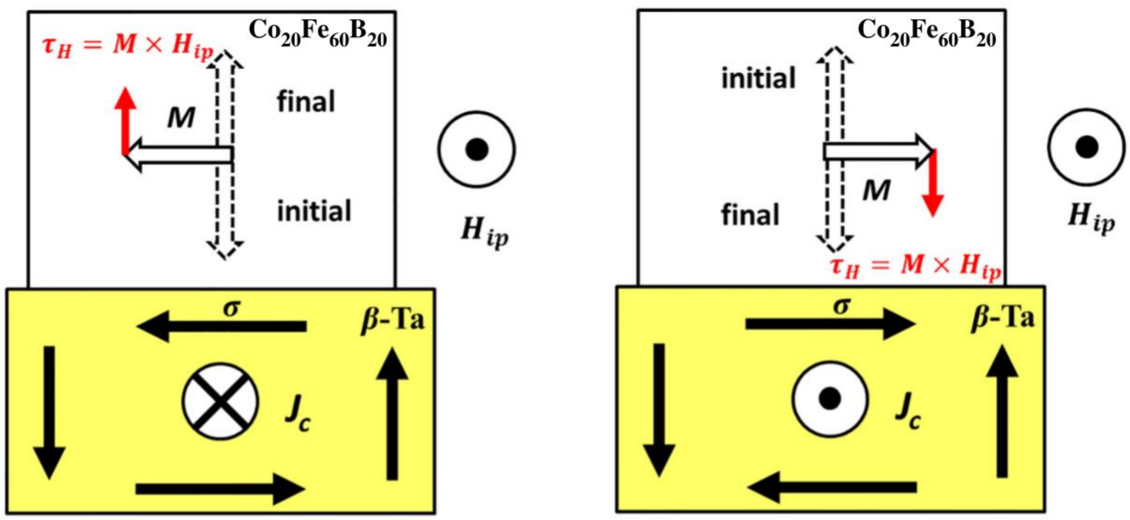

Figure 3-1. The direction of the spin orbit torque depends upon the direction of the charge current in the heavy metal. A charge current flowing through the lead shown here in cross-section results in spin currents in both perpendicular directions. The spin currents are polarized in the third perpendicular direction. For example, the vertical spin current shown here flowing into the CoFeB is polarized along the horizontal axis. Figure taken from [32].

STT works by spin polarizing charge current as it encounters the ferromagnetic layers adjacent to the tunnel barrier. The free layer magnetization is reversed by exceeding a critical current density set by the intrinsic energy barrier to switching of the free layer [47,48]. The critical current density is normally on the order of 10^6 A/cm^2 [97].

Driving this high current density across the MTJ’s tunnel barrier degrades the tunnel barrier [36]. SOT avoids this longevity problem by driving the large current density through an entirely metallic channel. Driving large currents across the high resistance tunnel barrier in STT is also highly dissipative. SOT drives its large currents through metallic leads, thus offering lower energy expenditure per switch. These benefits come at the cost of added complexity in creating a three terminal device rather two. However, three terminal transistors are the current technological paradigm.

Magnetic field control of MTJs uses electric current flowing through leads patterned on the chip to generate an Oersted magnetic field [68]. These MTJs are controlled using fields of 50-250 Oe for industrially relevant MTJs with diameters of 20-40 nm [19]. The current flowing through these leads generates field all along the leads, not only near the MTJs they are meant to switch. This type of arrangement severely limits the possible density of MTJs on a given chip. Field controlled MTJs are also effectively four-terminal devices, with two terminals for the read circuit connected to the MTJ and another two for the field-generating write circuit. The benefit of this scheme is that the read and write paths are electrically isolated [68]. SOT offers potential for high density MTJs, while separating the read and write paths, though the two paths share a common ground between separately energized leads.

SOT offers energy saving over STT by using a lower resistance write path. The use of the metallic write path also increases device longevity compared to STT by removing the high current density from the high resistance tunnel barrier. Three-terminal SOT devices also offer lower complexity and higher density than the four-terminal magnetic field-switched MTJ products.

Here I will present an experiment in which SOT was used to switch a very high thermal stability ferromagnet. This work was done when I was a junior graduate student working with Mukund Bapna, so my contributions were mostly in nanofabrication and setting up the SOT current pulse circuit. I will focus a bit more on those aspects here than in later chapters.

3.2 Nanofabrication

The MTJs were patterned from a thin film stack grown by magnetron sputtering on a silicon substrate by Weigang Wang's group at the University of Arizona. The stack consisted of Ta(3)/Ru(5)/Ta(4)/$Co_{20}Fe_{60}B_{20}$(0.8)/MgO(1.5)/$Co_{20}Fe_{60}B_{20}$(1.5)/Ta(5)/Ru(9), where the numbers in parentheses are the film thickness in nanometers, and the subscripts indicate the CoFeB alloy composition. Recall that CoFeB layers with thicknesses of 1.5 nm and smaller have perpendicular-to-plane magnetization while CoFeB layers with thicknesses greater than 1.5 nm have in-plane magnetization [30].

To make the SOT devices using this film, 21 nm of silicon nitride was added to act as a hard mask for later etching. Next, the sample was spin coated with hydrogen silsesquioxane (HSQ) and baked at 190°C for two minutes. The pillars were then written in the Sirion 600 SEM using Nabity nanometer pattern generation system (NPGS) software. The pillars were written as concentric circles using line dose parameters, since area dose had proven unreliable on that system at small feature size. After development with CD-26, the exposed HSQ left behind 30 nm thick islands of silicon oxide. Next, CF_4/CHF_3 reactive ion etching (RIE) was used to etch the silicon nitride. This chemistry etched silicon oxide more slowly than silicon nitride, and the silicon oxide added thickness where the HSQ was exposed to the electron beam. Thus, after RIE, the sample was left with islands of bilayer silicon nitride and silicon oxide on top of the metallic films. Next, the sample was etched using Ar ion milling. This type of etch removed the silicon compounds slower than the metals. After ion milling, the MTJ pillars were left on top of a thin Ta layer. Careful selection of the silicon nitride thickness and etch times was important to both guarantee the pillars remained after ion milling and that there was no residual silicon nitride on top of the pillars to interfere with later electrical connection. The sample was next coated with AZ 4110 photoresist and exposed in a Karl Suss MA6 mask aligner with a photomask that defined the Ta bottom leads. After development, the sample consisted of a thin layer of Ta on the substrate, an array of MTJ pillars, and about 1 μm thick AZ resist in the shape of the cross leads and bond pads. The sample was then etched again in the ion mill to remove the remain Ta except where it was covered by photoresist. After sonicating to remove the remaining photoresist, the photolithography procedure was repeated with another mask identical to the first except for opposite polarity and a small gap near the crossed leads. This left the sample coated with photoresist except for trenches where the thick Pt leads belonged. A film of 10 nm Ta and 200 nm Pt was then sputter deposited on the sample. Finally, the photoresist was removed by sonicating in acetone.

This removed the excess lead material, leaving behind the Pt leads and bond pads. The sample was then ready for testing.

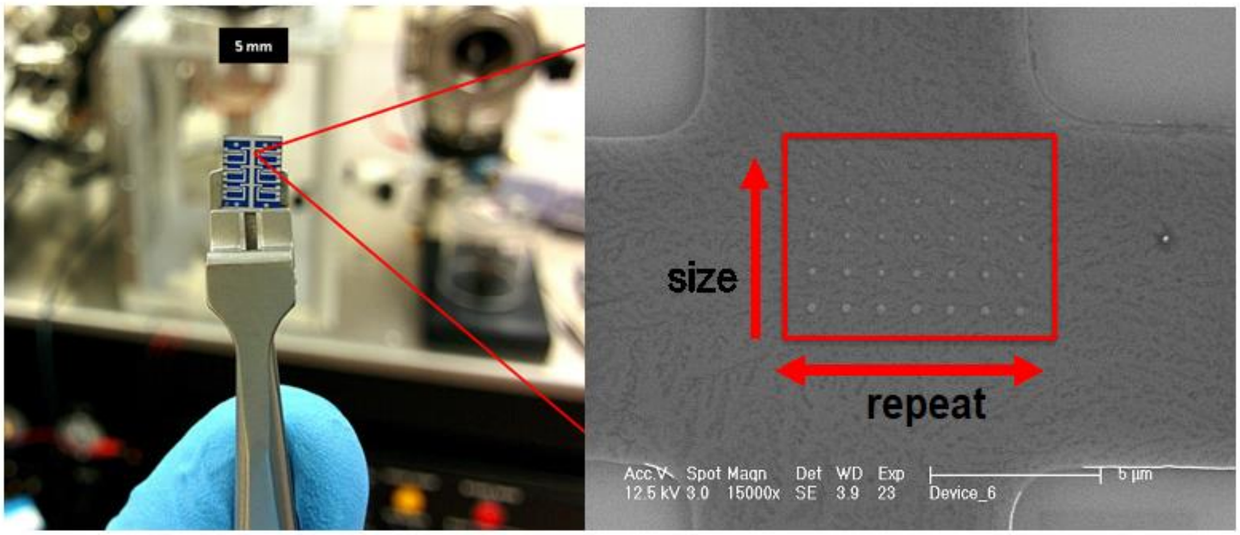

Figure 3-2. Arrays of the perpendicularly magnetized MTJs sit on thin Ta leads. The MTJ pillars were etched by Ar ion milling, then thick Pt leads and wire bonding pads were sputter deposited. The MTJs sit at the center of cross-shaped leads enabling tests of the symmetry of the spin orbit torque.

3.3 Detecting Switches by Conductive Atomic Force Microscopy

The Pt bond pads on the sample were wire bonded to macroscopic leads to be connected to the pulse generator and the oscilloscope used to monitor the current pulse. The sample was placed in our RHK UHV 350 conductive atomic force microscope (CAFM). The sample was measured in atmosphere at room temperature. Figure 3-3 shows the experimental setup. An in-plane field was applied using permanent magnets along the direction of the charge current to contribute to the torque as shown in Figure 3-1 as H_{ip}. Once the MTJ pillars were located with the CAFM, the CAFM tip was placed on top of the MTJ pillar, and a resistance vs magnetic field loop was collected. Resistance vs magnetic field loops function similarly to magnetic moment vs magnetic field loops typically performed with magnetic nanoparticles or thin films, but show switching by a change in resistance rather than magnetic moment. The fields at which switching occurs are usually the same. After determining the orientation of the MTJ's fixed layer, a small external magnetic field was applied in the opposite direction of the fixed layer magnetization, the CAFM tip was raised out of contact with the MTJ, and a current of 40 mA was pulsed through the underlying Ta lead for 200 μs. The current pulsed was monitored with an oscilloscope connected in parallel with the Ta leads as shown in Figure 3-3. After the current pulse, the CAFM tip was again placed on the MTJ pillar to measure the new resistance and perform another resistance vs magnetic field measurement. This procedure was repeated for different combinations of fixed layer magnetization direction and SOT-generating charge current direction, as will be discussed later.

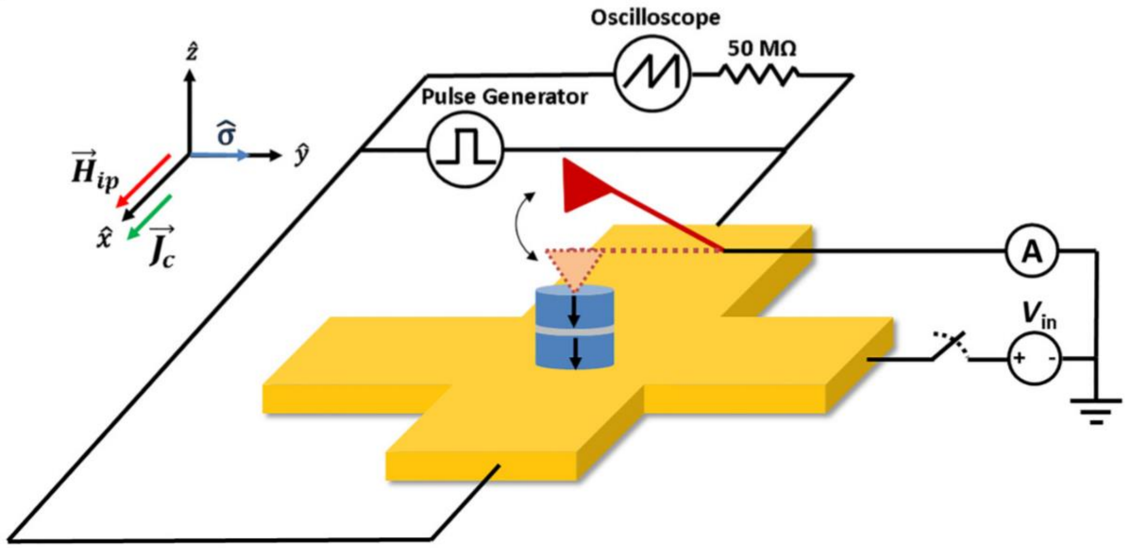

Figure 3-3. The perpendicularly magnetized MTJ sits at the center of cross-shaped Ta leads. The leads are connected to a pulse generator, which is used to generate the charge current in the Ta. Connected to the perpendicular lead is the bias source for the conductive AFM read circuit. The AFM tip is placed on top of the MTJ pillar to read the state of the device, raised out of contact while the SOT current is pulsed, and finally lowered to measure the state of the device after the pulse. Meanwhile, a small, in-plane magnetic field is applied parallel to the direction of the pulsed current. The current pulse is monitored by an oscilloscope connected in parallel with the pulse generator. Figure taken from [32]**.**

3.4 Spin Orbit Torque Magnetization Switching

In this experiment, the fixed layer of a perpendicularly magnetized MTJ was switched using a combination of magnetic field and SOT. Figure 3-4a shows an SEM micrograph of the 20 nm diameter MTJ under test. The 20 nm diameter made these devices technologically relevant, being smaller even than MRAM devices in production in 2020 [37,98].

Figure 3-4b shows a CAFM current map scan of the MTJ initialized in the low-current, antiparallel state. The shape of the MTJ appears elliptical and rough at the edge. This is partly an artifact of CAFM imaging. The CAFM image is a convolution of the CAFM probe and the object being imaged, resulting in unreliable lateral dimensions in imaging. Other imaging artifacts arise from the fast and slow scanning directions. The CAFM probe moves across the surface like a typewriter, scanning quickly left to right before resetting at the left edge of the next line. This tends to result in streaking and stretching left to right as the tip scans quickly across the surface and image tearing up and down as thermal drift causes inconsistent resetting of the tip line to line. The edge roughness that persists between Figure 3-4b and Figure 3-4c is likely due to the debris shown as the bright spots around the pillar in Figure 3-4a.

After acquiring a current map of the MTJ in the antiparallel state, a 100 Oe out-of-plane field was applied using an electromagnet and 40 mA of current was pulsed for 200 μs through the Ta lead under the MTJ. This corresponds to a current density of 4.17×10^7 A/cm^2 averaged across all the metal layers underlying the magnetic layer. Considering the three metal layers as parallel resistors, the Ru layer, with its low resistivity and greater thickness, dominates the current density. The spin diffusion length of Ta has been found to be 5.1±0.6 nm, so the SOT generation was dominated by the top Ta layer immediately adjacent to the ferromagnet [99]. Accounting for the differences in resistivity, the top Ta layer carried a charge current density of 3.35×10^6 A/cm^2, on par with STT current densities.

Since the ferromagnetic layer adjacent to the Ta lead was intended as the fixed layer of this MTJ film, the energy barrier to switching its magnetization direction was greater than could be overcome with the SOT current pulse alone. The 100 Oe out-of-plane field served to aid the SOT current in reversing the magnetization. Figure 3-4c shows the CAFM current map of the MTJ after the current pulse. The MTJ switched from antiparallel before the pulse to parallel after the pulse.

To confirm that the lower resistance of the MTJ was caused by switching the magnetization direction of the fixed layer and not a thermally activated switch of the free layer, the switching experiment was repeated. A resistance vs magnetic field measurement was made to determine the direction of the loop shift for the free layer. Since the fixed layer is so stable, the 1.3 kOe field available from the electromagnet was insufficient to reverse the fixed layer. Instead, the direction of the fixed layer magnetization was measured indirectly using the offset in the free layer magnetization loop. The field from the fixed layer caused an offset in the switching fields of the free layer such that they were not centered on zero. The switching fields were instead centered on the stray field from the fixed layer. Figure 3-4d shows the free layer magnetization loop before the SOT current was pulsed. The switching field offset before pulsing was positive. After pulsing, shown in Figure 3-4e, the switching field offset was negative. This indicated indirectly that the fixed layer magnetization had switched directions.

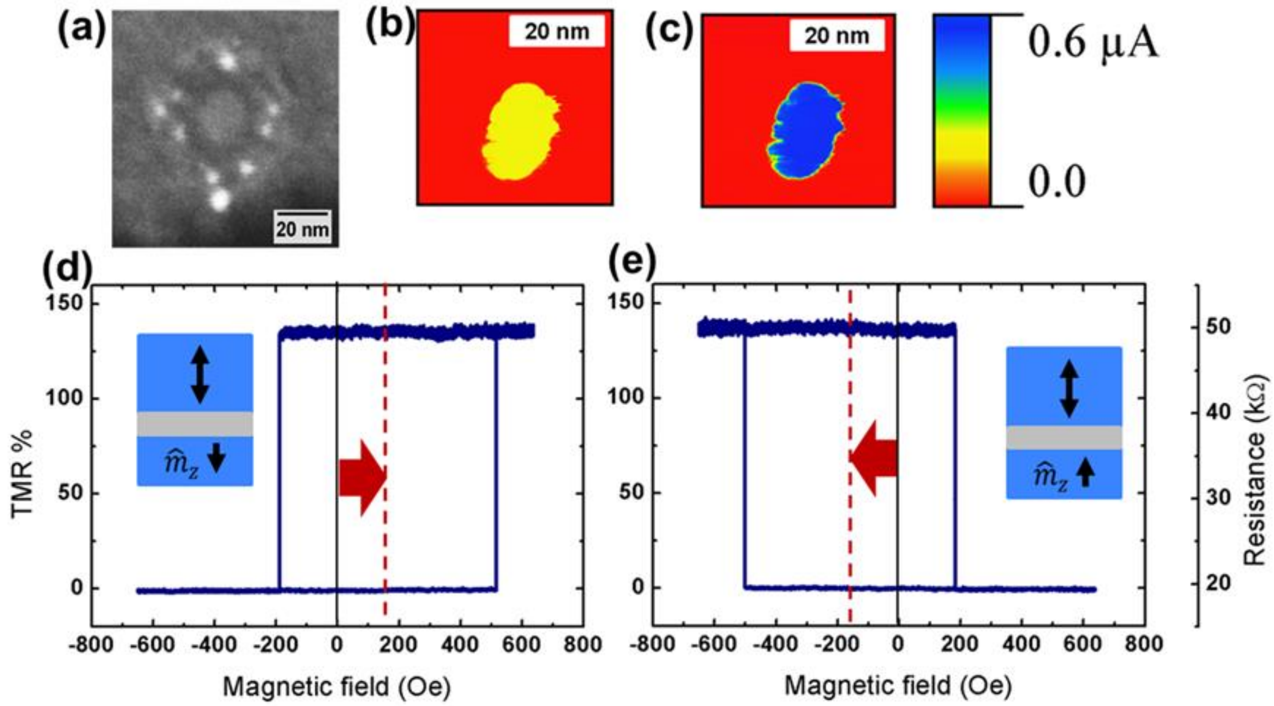

Figure 3-4. a) This SEM micrograph shows the 20 nm diameter perpendicular MTJ. b) The CAFM current map shows the MTJ initialized in the antiparallel state. c) After pulsing current through the Ta leads, the current map shows the device has switched to the parallel state. d) Prior to the current pulse, the free layer magnetization loop is shifted toward positive field. e) After the current pulse, the free layer magnetization loop is shifted toward negative field. Figure taken from [32]**.**

Another means to confirm the magnetization switching was caused by SOT is to test the switching and non-switching combinations of the SOT-generating charge current directions and initial fixed layer magnetization directions, shown in Figure 3-5. As shown in Figure 3-1, the direction of the torque resulting from the SOT current points in opposite directions for opposite directions of current flow. The torque either reverses the direction of the magnetization or maintains the magnetization direction as it was initialized. The external magnetic field was always applied in the opposite direction of the initialized fixed layer magnetization. The 40 mA for 200 μs current pulse previously used to switch the magnetization direction was then applied. The switching and non-switching combinations measured matched the expectation for SOT switching shown in Figure 3-5.

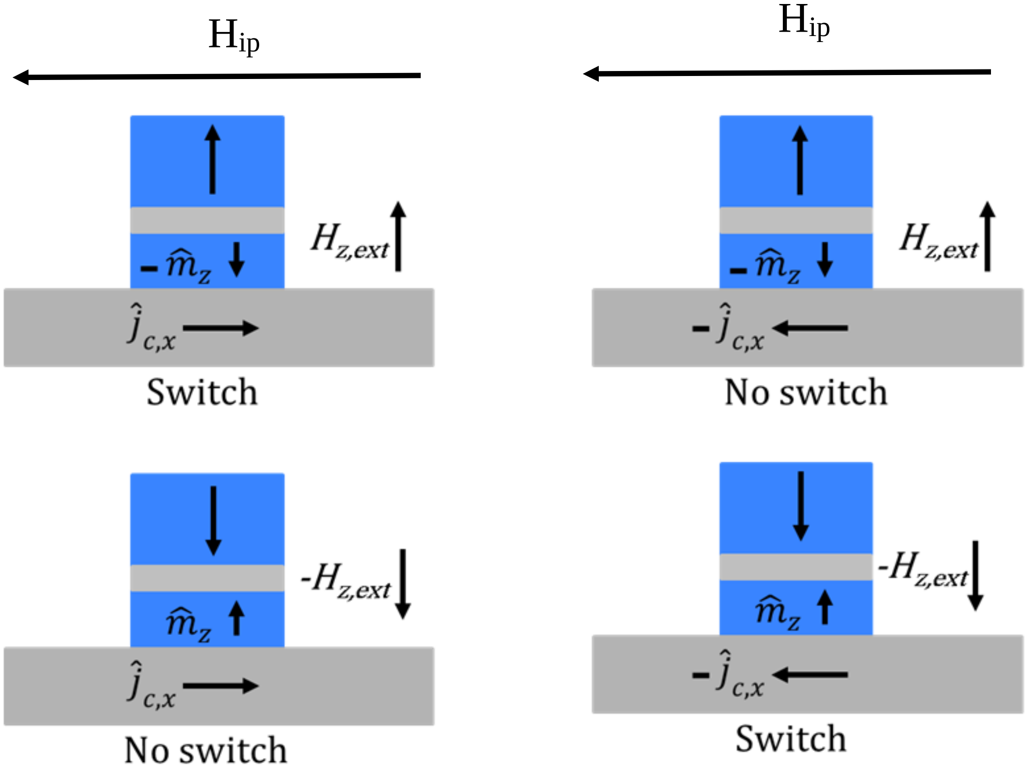

Figure 3-5. Spin orbit torque effects have built-in symmetries that can be tested to confirm switching was caused by SOT and not some other effect. With two possible directions for the SOT-generating charge currents and two directions for the fixed layer magnetization, there are two combinations that result in switching and two that do not. Figure taken from unpublished work by Mukund Bapna.

Since this MTJ film was deposited with the free layer on top, the magnetic layer switched with SOT had a very high energy barrier to switching. Ideally, the free layer would be on the bottom adjacent to the Ta leads. The fixed layer could not be switched using the maximum field output of the electromagnet of 1.3 kOe. The anisotropy of the nanomagnet could not be determined directly, but it was estimated using parameters measured for the top layer. The top and bottom layers in this film were the same material. The difference was that the bottom layer was thinner than the top layer—0.8 nm vs 1.5 nm. The effective anisotropy, K_{eff}, is given by the equation

$$K_{eff} = \frac{K_{int}}{t} - K_{bulk} - K_{shape}$$

where K_{int} is the interface anisotropy, t is the layer's thickness, K_{bulk} is the bulk anisotropy, and K_{shape} is the shape anisotropy. Assuming the only difference between the top and bottom CoFeB layers was the thickness, the bottom layer energy barrier to switching was 47±2 k_BT. In other words, the anisotropy field for the 0.8 nm thick layer was 14.3±1.3 kOe [32]. The data retention time for this nanomagnet would have been 1100-60000 years.

3.5 Summary

SOT switching was performed on the smallest diameter MTJ up to that time. The current density used was greater than that necessary for STT, but it was pulsed through low resistance metallic leads rather than a high resistance oxide tunnel barrier. The fabrication of this sample was one of the first times I used electron beam lithography and multiple layers of photolithography in the same process. It was also the first use of a separate signal path in the CAFM. Switching this high thermal stability MTJ would later motivate an attempt to control a low thermal stability MTJ using SOT.

Chapter 4 Superparamagnetic perpendicular magnetic tunnel junctions for true random number generators

This chapter consists of my paper published in AIP Advances [18]. Here I present a random number generator using a low thermal stability, perpendicularly magnetized MTJ. This was the first use of perpendicular MTJs for the random number generator application, and the first use of voltage controlled magnetic anisotropy to control the rate of random telegraph noise.

4.1 Introduction

Encryption is vital to protecting everything from personal data to financial transactions to national security information, and recent high-profile compromises of data security highlight the need for better encryption. Due to their limited speed, large area, and high-power consumption, it is not feasible to generate *true* random numbers fast enough for real-time encryption, hence hardware random number generators (RNGs) are used to seed *pseudo*-random number generating algorithms. The steady growth of processing power necessitates ever-larger encryption keys. Superparamagnetic perpendicular magnetic tunnel junctions (SP-pMTJs) offer a low power, dense alternative to current hardware RNG technology. Here we fabricate RNGs and test the randomness of their output.

The current technology for hardware RNGs is the free running oscillator ring. These RNGs use phase jitter arising from the changing temperature of the silicon in a series of NOT gates as a source of electronic noise that is thereby used to generate random bits [100]. The frequency of the ring oscillator is set by the capacitive lag as the gates of the MOSFETs charge in series. The output is read at a rate set by an external clock, which has its own inherent uncertainty. The variability of the frequencies in the ring oscillator and clock give rise to a random walk in their relative phase, with the frequency of each component being dependent on the temperature. These circuits are typically hundreds of square microns, consume milliwatts of power, and generate tens to hundreds of megabits per second [101]. Recent experiments in CMOS based RNGs have increased the speed to a few gigabits per second and reduced area by a factor of ten, but without significant reduction in power consumption [102].

Previous work on superparamagnetism has mainly focused on nanoparticles [46]. Recently, superparamagnetic magnetic tunnel junctions (SP-MTJs) have been proposed for use in RNGs. Experimental work has been done using in-plane SP-MTJs in which random bits were produced by 50 x150 nm^2 devices at a rate of 1.66 kHz and an energy cost of about 2.5 fJ/bit [103]. However, dense arrays of in-plane devices would have significant magnetostatic interactions that could compromise the randomness of their outputs. There has been some simulation work done to suggest that low thermal stability perpendicular MTJs (pMTJs) can be used to create highly parallel random number generators with small process size, high density, low power, and high throughput [104]. Perpendicular MTJs can be scaled down to 20nm or smaller [92] and can be patterned with smaller pitch/higher density [105]. Here we present experimental results from a 60nm hardwired SP-pMTJ used as a true random number generator with voltage tunable frequency.

4.2 Experimental Methods

Perpendicular MTJs were used to capitalize on voltage controlled magnetic anisotropy (VCMA). A film stack of Si/Ta(5)/Ru(10)/Ta(5)/$Co_{20}Fe_{60}B_{20}$(0.85)/MgO(~1.5)/ $Co_{40}Fe_{40}B_{20}$(1.5)/Ta(5)/Ru(8) was deposited by magnetron sputtering. Here the numbers in parentheses are the film thicknesses in nanometers. The film was annealed at 300°C for 10 minutes. 60 nm diameter MTJ pillars were defined by electron beam lithography and Ar ion milling, and leads and bond pads were defined by photolithography.

The sample was then placed in a chip carrier and wire bonded, in order to connect individual devices to a voltage source and ammeter. Bias was applied through the bottom lead while the top was grounded. Thus, for negative bias, electrons flow upward from the fixed reference layer toward the low thermal stability reference layer.

A MTJ-based RNG should spend equal amounts of time in the parallel (P) and antiparallel (AP) states, and therefore the stray field due to the fixed layer should be offset. In small diameter MTJs this field can be hundreds of Oe. The minor loop tunnel magnetoresistance as a function of magnetic field was measured to determine the magnitude of this stray field for a given device, and an external field in the opposite direction was then applied to cancel it. The data was acquired at an acquisition frequency of 100 MHz for 500 ms to get statistically significant number of switches.

4.3 Results and Discussion

Figure 4-1 shows some sample time traces collected at different bias values. The tunnel magnetoresistance (TMR) ranged from 10% at -1.3 V to 35% at -0.4 V. For a given voltage, the separation between the states was used to threshold and digitize the signal as ones (high resistance) or zeros (low resistance).

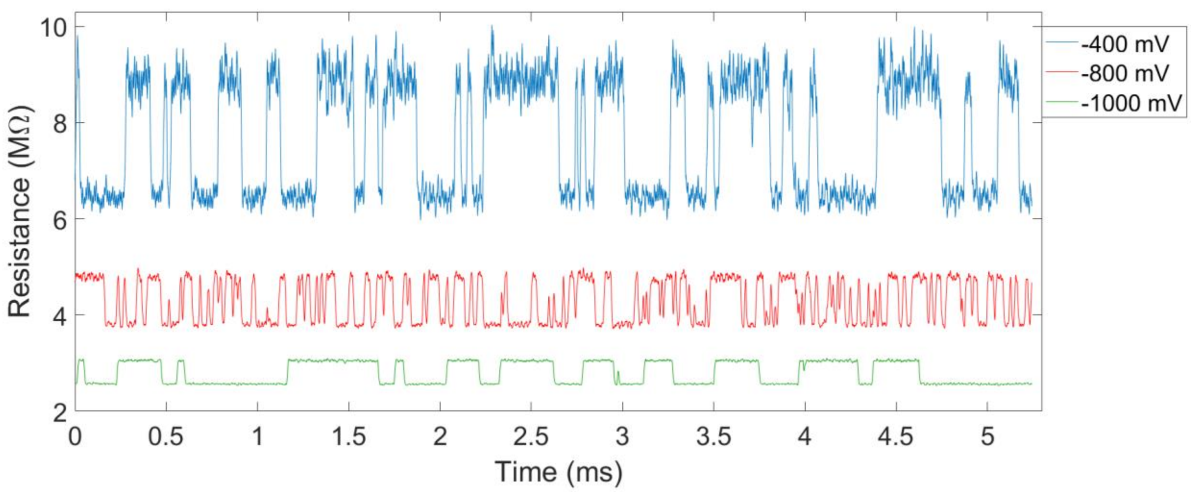

Figure 4-1. The time varying resistance of the MTJ changes amplitude and frequency as a function of bias. Here an external field of 15.6 Oe was applied to cancel the stray field.

Thermally driven magnetization reversal of a superparamagnet is described by a Néel relaxation model, with a relaxation time given by $\tau = \tau_0 \exp\left[\mathrm{Keff}\frac{\mathrm{V}}{\mathrm{kBT}}\right]$, where τ is the average time spent in the state, , τ_0 is the inverse of the Larmor precession frequency, K_{eff} is the effective anisotropy, V is the volume, k_B is the Boltzmann constant, and T is the temperature. For the SP-MTJ, the hopping process between P and AP state follows Poisson statistics and hence the distribution of time duration between switching events is exponential. From the fit of the exponential distribution, the lifetimes τ_P and τ_{AP}, corresponding to average times in the P and AP states, were obtained.

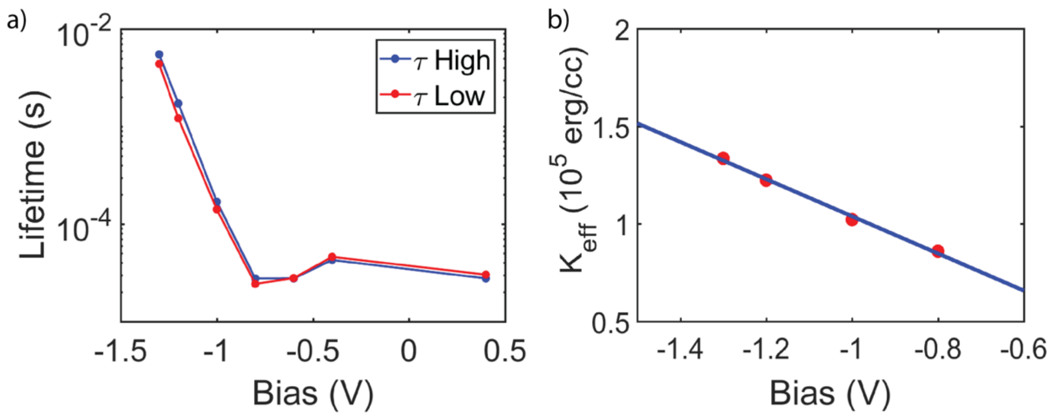

Figure 4-2. a) The lifetime of the high and low current states vary nonlinearly with bias. b) In the linear regime, the effective anisotropy changes with a VCMA coefficient of 21 fJ/Vm.

Figure 4-2a shows the lifetime of the high and low current states as a function of bias. The time the device spends in each state is a nonlinear function of bias. The trend is linear and steep for large negative bias, but relatively unchanging for bias values more positive than about -800 mV. Using the Néel relaxation model, we can calculate how the bias affects the thermal stability factor, Δ. Figure 2b shows that the thermal stability is tunable with bias from 14.7 at -1.3 V to 9.5 at -0.8 V. The voltage controlled magnetic anisotropy (VCMA) coefficient is 21 fJ/Vm. In the maximum efficiency case of -0.4 V, the device operates at a power of 27 nW and an average speed of 45 kHz, thus the device produces random bits at an energy cost of 600 fJ per bit. The -0.4V case also offers the highest signal with a TMR ratio of about 35%.

The data stream was then analyzed for randomness by a number of methods from the NIST Statistical Test Suite [106]. For the analysis of randomness, the data were sampled at intervals of $\tau = (\tau_P^{-1} + \tau_{AP}^{-1})^{-1}$. The left column of Table 4.1 lists the different tests. If a p-value >0.01 (significance level) is found for a particular test then the input bit stream is characterized as random as far as that test is concerned. For a RNG under test to qualify as a true RNG, a bit stream produced by it should pass through all the NIST STS tests.

An XOR whitening process was then applied to get rid of any bias for the device being in state 0 or 1. This bias in probability of the device being in P or AP state originate from the fact that the stray field from the bottom layer can favors P state over AP state. This bias can be large if the bottom layer is patterned [107], however, here the effect is small since the reference layer was not patterned through. In an actual device, this effect can be mitigated all together, for example, by having a synthetic antiferromagnet structure with the reference layer to cancel the stray field.

The effect of different XOR whitening process is shown in Table 4.1. The bit stream for each bias value was separated into equal pieces to be input into a logical exclusive or operation. For XOR2, the data is divided into two streams and fed into an XOR, and the output is then used for the statistical testing. XOR4 and XOR8 use four and eight inputs, respectively. In a real application, these inputs could come from different tunnel junctions in parallel. The p-value for each test is shown for the highest speed case (-800 mV) and the most energy efficient case (-400 mV). Bold values indicate passing the test for randomness. For our data set, XOR2 whitening is effective only for large negative bias values, XOR4 is successful for biases from -1.3 V to -0.8 V, and XOR8 is sufficient to yield random bit streams in all cases.

Table 4.1. The NIST STS tests for randomness were applied to the time-resolved resistance measurements with different degrees of whitening. Bold-faced p-values indicate a passed test.

		-800 mV		-400 mV		
Test	Failure Criteria [108]	XOR2	XOR4	XOR2	XOR4	XOR8
Frequency	Total number of 0's and 1's mismatch	**0.597**	**0.984**	**0.656**	**0.242**	**0.649**
Block Frequency	Number of 0's and 1's mismatch within a subset	**0.030**	**0.328**	0	**0.861**	**0.344**
Cumulative Sums Forward	Running sum deviates too far from half the length	**0.877**	**0.950**	**0.705**	**0.379**	**0.798**
Cumulative Sums Reverse	Same as previous, but in reverse direction	**0.419**	**0.939**	**0.345**	**0.194**	**0.862**
Runs	Too many sequences of consecutive bits of one type.	0	**0.889**	0	0	**0.982**
Longest Run	Too many consecutive bits of one type	0	**0.846**	0	0.010	**0.773**
Approximate Entropy	Bit sequence too unlikely	0	**0.801**	0	0	**0.800**
Serial	Multiple low entropy sequences in a row	0	**0.573**	0	0	**0.653**
FFT	Periodicity in bit stream	**0.544**	**0.745**	0	**0.876**	**0.032**

Figure 3a shows a resistance versus applied magnetic field minor loop. An applied magnetic field initialized the free layer in one resistance state and was then swept at a rate of 60 Oe/s until the free layer was stable in the other state. In the middle region of the figure, the free layer switches thermally between the two resistance states with the highest frequency of switching where the applied field exactly cancels the stray field of the fixed layer. The the average magnetization was controlled by the applied field, as shown in Figure 3b. Using an applied magnetic field range of just 60 Oe, we can tune the probability of reading the high resistance state from 0 to 1.

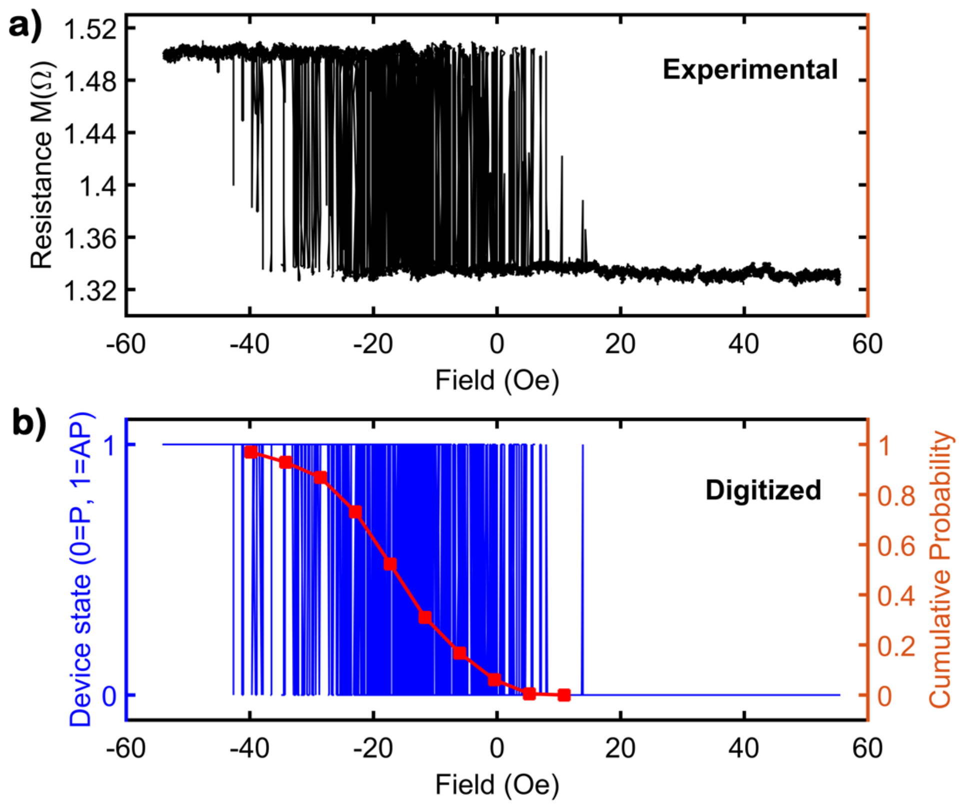

Figure 4-3. a) A minor hysteresis loop acquired at -1.3 V showing the coercivity (half width of loop) and stray field (loop center) of the device. The free layer is telegraphing throughout the measurement. b) The digitized minor loop with a superimposed average magnetization (sigmoid) found from integration of the minor loop. Using the applied magnetic field, we can make the device favor one state rather than being approximately unbiased as in the time-resolved measurements.

4.4 Conclusion

We have shown SP-pMTJs can be used as true random number generators. These RNG devices operate at much lower power than current CMOS oscillator-based technologies, opening up more possibilities for mobile applications. While the energy per bit is approximately a factor of three lower than cutting edge CMOS technology [102], the process size of the SP-pMTJ is orders of magnitude smaller. Increasing the temperature of SP-MTJs also increases the speed of magnetization reversal rather than slowing down like semiconductor RNGs [109]. As the magnetic volume of the SP-pMTJs decreases, the speed of magnetization reversal should increase exponentially. Assuming all other parameters remain constant, a 7 nm diameter MTJ would produce random bits at over 80 MHz at -800 mV. With a constant resistance-area product, such a small MTJ would have a resistance over 100 MΩ and thus reduce power consumption by an order of magnitude. Further, these types of devices can be used in probabilistic computing if the magnetoresistance can be controlled by a current or voltage.

`

4.5 Acknowledgements

This work was supported in part by C-SPIN, one of the six centers of STARnet, a Semiconductor Research Corporation program, sponsored by MARCO and DARPA under contract no 2013-MA-2831 and by NSF grant ECCS-1709845.

Chapter 5 Prototyping of Spin Transfer Torque Controlled Stochastic Bit

In this chapter, I present very low thermal stability in-plane MTJs controlled with STT. This work held the record for thermal reversal rate until 2021 [67]. The STT control of these MTJs fit the criteria for stochastic logic devices as predicted by theory. I fabricated and measured these devices and analyzed the data. Ahmed Abdelgawad did simulations to help explain the experimental result using software developed by Richard Evans. Thomas Wong also participated in the data analysis. This work was published in Phys. Rev. Applied [20].

5.1 Background

The stochastic, thermal reversal of magnetization was once a phenomenon to be avoided, particularly when designing magnetic data storage devices [33], [34]. High thermal stability magnetization was preferred for long-term data storage, though the retention time was balanced with data rate [35]. The advent of magnetic random-access memory (MRAM) necessitated an even more nuanced approach to thermal stability as write times and energy both needed to be minimized for working memory operation [36], with write times now in the 1-10 ns range while maintaining 60-100 $k_B T$ energy barriers [37]. Recent interest in stochastic computing has renewed interest in superparamagnetism as a source of random fluctuations [18,38–42].

Stochastic computing uses random fluctuations to sample the space of possible solutions. The stochastic elements are networked together with a feedback mechanism that promotes the device states that provide the minimum energy answer. The system is set up so that the correct answer to the problem corresponds to the minimum energy states, and they become more likely than the higher energy states over time. Stochastic computing devices will need to be instantaneously digital—a measurement taken each time the computer's clock cycles should yield a binary result—and analog in time average. They will need to electronically tunable and switch frequently such that the time average converges to the programmed value in a reasonable averaging window [86]. That is to stay the devices must switch frequently enough to accumulate a statistically significant sample of low-energy states and provide the correct answer faster than a more conventional computing system.

The band structure of a ferromagnet has a greater density of states for electrons whose spins align to the local magnetization. Electrons aligned to the magnetization are the majority charge carriers in the ferromagnetic material. Thus, electron current passing through the ferromagnet becomes spin polarized [110–112]. When the spin polarized current encounters another ferromagnet magnetized in the same direction, the majority spin carriers from the first ferromagnet can fill the majority states in the next ferromagnet. Parallel magnetizations result in low electrical resistance. However, if the second ferromagnet is magnetized in the opposite direction, the majority spin carriers from the first ferromagnet have only the minority spin states to fill in the second ferromagnet, limiting the electron flow. Antiparallel magnetizations result in high electrical resistance because of the mismatch in the density of states. Figure 5-1 shows a schematic of the density of states model. This is the principle behind giant magnetoresistance (GMR), where the two ferromagnets are separated by a thin, nonmagnetic metallic spacer [3]. Placing a tunnel barrier between the two ferromagnets instead of a metallic spacer further enhances the spin polarization of the current, and thus the difference in electrical resistance of the two magnetic configurations. Conduction across the tunnel barrier occurs through evanescent states, which exponentially suppresses transport by electrons lacking specific symmetry characteristics [113], [114]. The is effect is known as tunnel magnetoresistance (TMR).

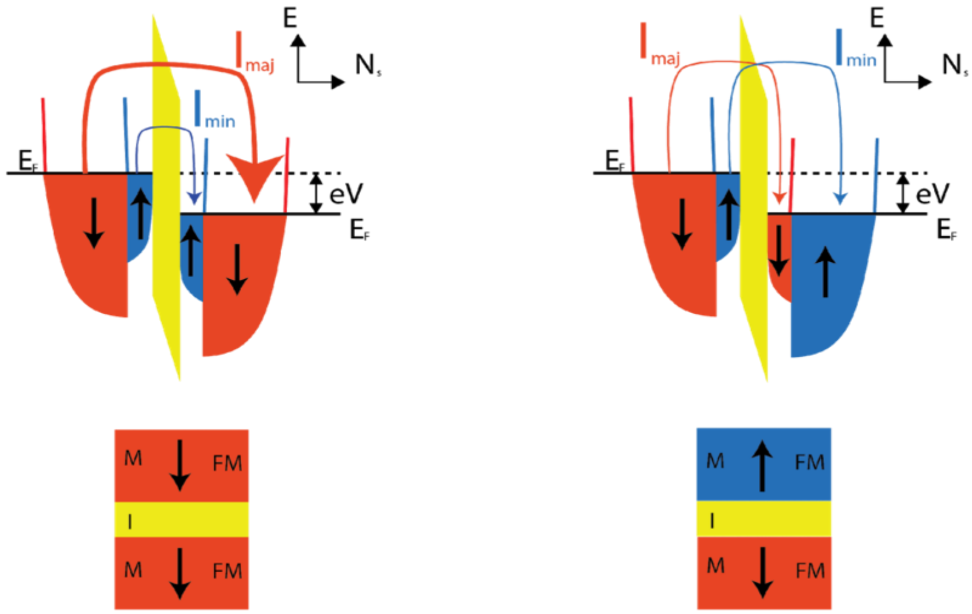

Figure 5-1. The number of available states for a tunnelling electron to occupy depends upon the alignment of the magnetic moments. When the moments are parallel, the majority carriers on the incident side have a large number of states available on the transmitted side, resulting in a low resistance. When the moments are antiparallel, the majority carriers have a small number of available states on the opposite side of the tunnel barrier, leading to high resistance.

Spin transfer torque (STT) switching uses spin polarized electrical current to reverse magnetization. In a magnetic tunnel junction (MTJ), the fixed layer ferromagnet spin polarizes the electron current before the electrons cross the tunnel barrier. After crossing the tunnel barrier, the electrons become spin polarized again by the second ferromagnetic layer. To re-polarize the electrons, the second ferromagnet exerts a torque on the electrons. This produces an equal and opposite torque on the free layer magnetization to switch from antiparallel to parallel. To switch from parallel to antiparallel, the current flows in the opposite direction. The current is spin polarized by the free layer magnetization before crossing the tunnel barrier. The current polarized parallel to the fixed layer magnetization continues to pass through the device, but the antiparallel polarized current is reflected into the free layer due to the lack of available states for the minority spin carriers in the fixed layer. The excess of antiparallel current in the free layer causes a torque that reverses the free layer magnetization [47–49]. The magnetization reverses in either case when the spin polarized current density exceeds the critical current density. The critical current density at zero temperature can be estimated by

$$I_c = \frac{2\alpha e \mu_0}{P\hbar} M_s V (H + H_k + 2\pi M_s),$$

where α is the damping constant, e is the electron charge, μ_0 is the permeability of free space, P is the spin polarization factor, $\hbar$ is the reduced Planck's constant, M_s is the saturation magnetization, V is the volume of the free layer, H is the magnetic field on the free layer, and H_k is the anisotropy field [49], [115]. Using α=0.01, P=0.45, and M_s=800 emu/cm^3, I_c at zero temperature for our system is 2.4 mA. Thermal noise makes the magnetization reversal process probabilistic [116], and the critical current becomes a distribution rather than single valued [117]. When the energy barrier to switching becomes comparable to the thermal energy, the distribution of critical current becomes broad enough to manipulate the probability of finding the device in each state.

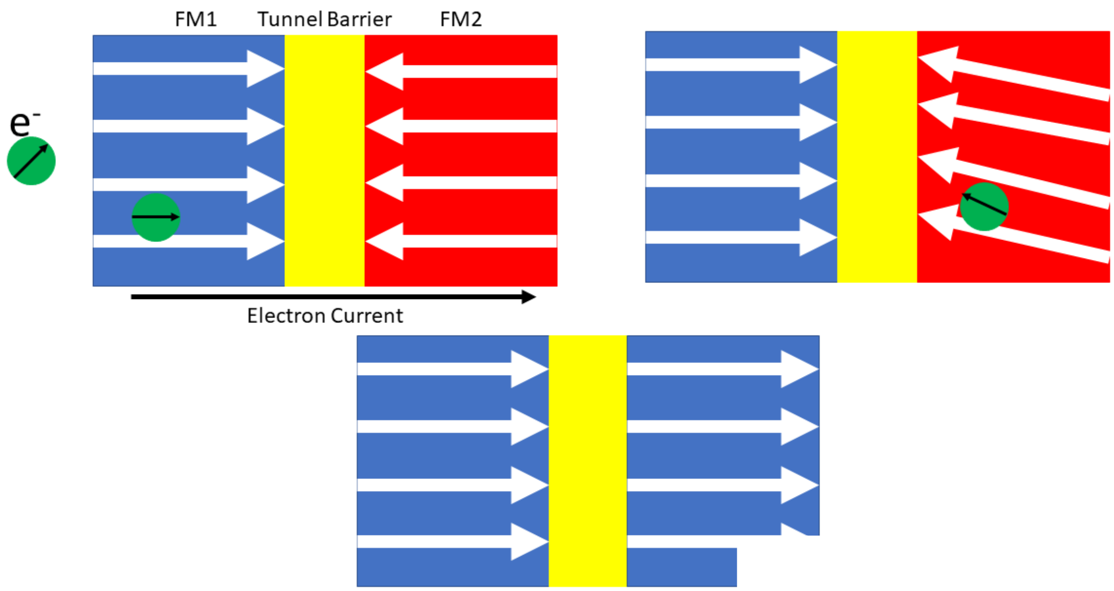

Figure 5-2. As electron current encounters a ferromagnetic material, the incoherent electrons become spin polarized. After the majority spin-carrying electrons cross the tunnel barrier, they become polarized again to align to the new local magnetization. The second ferromagnet reverses the direction of the electrons' spin polarization by applying a torque, and an equal and opposite torque is imparted on the ferromagnetic material. With a great enough density of electron current, the direction of the second magnetization can be reversed.

5.2 Nanofabrication

The film stack was grown by Everspin Technologies [88], and consists of SiO_2/Ta(50)/PtMn(20)/ CoFe(2)/Ru(0.8)/CoFe(3)/MgO(1)/CoFeB(2.5)/Ta(10)/Pt(5), where the numbers in parentheses are thicknesses in nanometers. The thick Ta layer was chosen to provide adhesion and a smooth seed layer for the PtMn antiferromagnet. The

PtMn pinned the magnetization direction of the adjacent CoFe layer. The thin Ru layer acted as a spacer to promote dipolar coupling between the two CoFe layers, greatly increasing the stability of the 3 nm CoFe fixed layer. The 1 nm MgO provided the resistance-area product of 5.4 $\Omega \cdot \mu m^2$ [73], making these devices suitable for STT switching as a current density on the order of 10^6 A/cm^2 can be driven across the barrier with a bias lower than the dielectric breakdown voltage. The low intrinsic anisotropy of the in-plane magnetized CoFeB layer gave this free layer a low energy barrier to thermal switching. The 10 nm Ta layer adheres the Pt cap, which provides a conductive contact without risk of oxidation.

Added to this film was a SiN_x layer used as a hard mask for later ion milling. Circular nanopillars were then defined by electron beam lithography using a hydrogen silsesquioxane (HSQ) resist in an FEI Sirion 600 scanning electron microscope with Nabity nanometer pattern generation system (NPGS) software. The HSQ pattern was transferred to the SiN_x hard mask layer by CF_4/CHF_3 reactive ion etch in a PlasmaTherm PT 790 and further transferred to the metallic film by argon ion milling in a Commonwealth ion mill with mass spectrometry of the etched material indicating where to stop the etch. The MTJ pillars were half-patterned, meaning that the ion milling was stopped at the MgO layer, according to the endpoint detection, as shown in Figure 5-3. Half-patterning was chosen for these devices to minimize the magnetostatic field from the fixed layer acting on the free layer [29]. The pillars had nominal diameters of 20, 30, 40, 50, 60, 70, and 80 nanometers and a spacing between pillars of 250 nm.

5.3 Conductive AFM Measurement

Electronic transport measurements were performed in atmosphere at room temperature using an RHK 350 conductive AFM system with an R9 control box. The R9 can digitize and record the current flowing through the MTJ pillar while simultaneously controlling the external magnetic field as well as the applied bias. Figure 5-3 shows the MTJ film and measurement setup. A film of 5 nm of Ta and 200 nm of Pt was sputtered onto Pointprobe silicon AFM tips from Nano World to facilitate electrical conduction and improve wear characteristics. The R9 is also capable of recording current transients, where the time resolution of about 20 μs is limited by the analog to digital converter.

I modified this system by adding a parallel analog voltage output from the transimpedance amplifier. I soldered the center wire of a BNC cable to the positive signal out terminal of the data cable connecting the output of the preamplifier to the analog to digital converter and the shield wire of the BNC to the negative signal terminal. Since I just soldered an extra wire to the pin, the signal to the R9 box is not interrupted. The parallel signal is sent to a Red Pitaya STEM board featuring a native oscilloscope function and, most importantly, a much faster analog to digital converter. The modification delivers a 250-fold improvement in time resolution for currents in the microamp to milliamp range, with the transimpedance amplifier now serving as the limiting element. The system can now resolve microamp currents with dwell times of around 70 ns. Photos and a schematic will be included in the appendices.

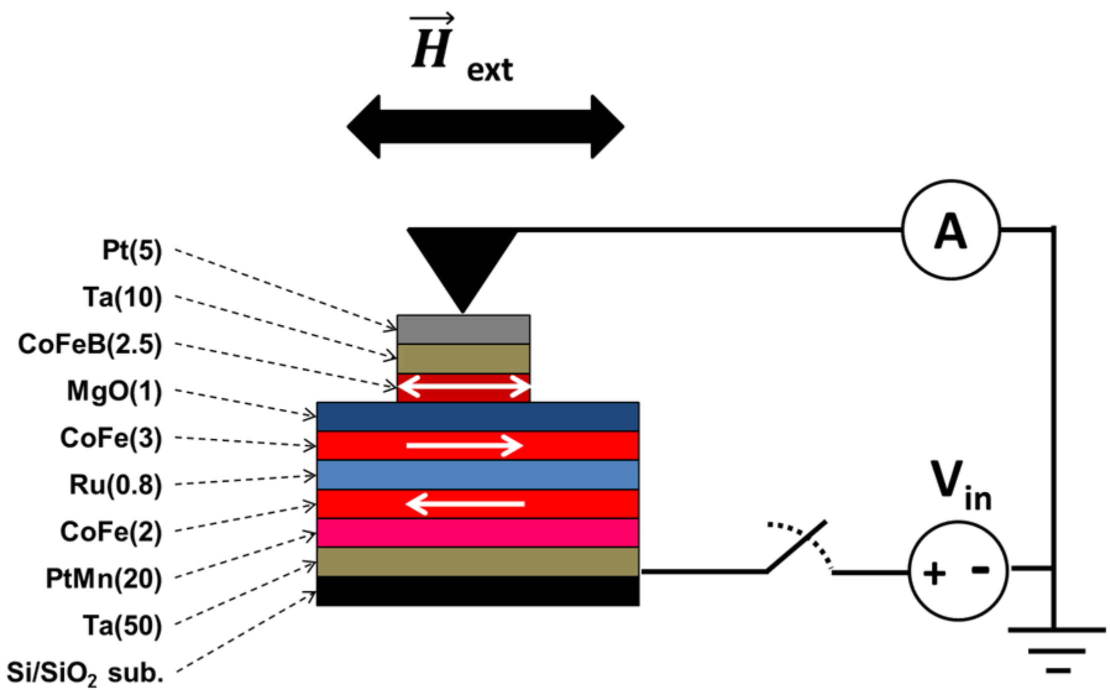

Figure 5-3. The Everspin Technologies film stack was half-patterned into MTJ pillars and measured in the RHK 350 conductive atomic force microscope. Figure taken from [29]**.**

5.4 Electronic Control of Magnetization

Spin transfer torque current was used to tune the state of the MTJ. Figure 5-4 shows the resistance of a 60 nm MTJ pillar as a function of applied bias. The MTJ is switched due to STT current, but the measurement is reported in terms of bias because it was a voltage-controlled measurement. In Figure 5-4A, the device is operating without an applied external field. At negative bias, with electrons flowing from the fixed layer to the free layer, the free layer magnetization remains parallel to that of the fixed layer. At a small positive bias of about 75 mV, with electrons flowing from the free layer to the fixed layer, the magnetization begins to reverse occasionally, but still spends most of its time in the parallel state. As the bias increases, the device spends more and more time in the antiparallel state, reaching the midpoint around 200 mV. The resistance favors the antiparallel state beyond that point until saturating around 350 mV. After reaching its maximum value, the bias repeats the sweep in reverse. The reversed bias sweep shows the tuning process is reversible with no apparent hysteresis. Note that the direction of electron flow and the preferred magnetization direction agrees with the earlier description of deterministic STT switching.

Figure 5-4B shows the bias sweep measurement repeated, now with a 14 Oe field applied to cancel out the stray magnetic field from the fixed layer. Cancelling the field moves the midpoint to 50 mV. A negative bias of -125 mV is necessary to saturate in the parallel state, while it saturates in the antiparallel state at less than 250 mV. The overall shape of the time-averaged resistance in both cases of Figure 5-4 was sigmoidal. The shape is slightly skewed by the nonlinear resistance of the tunnel barrier, particularly when the MTJ is in the antiparallel state. Since the potential encountered by the tunnelling electrons is not symmetric about the tunnel barrier, there is a quadratic dependence of the resistance on the applied bias. When the MTJ is in the parallel state, the potential is symmetric and the resistance is mostly linear in applied bias [118]. The resistance of the antiparallel state drops as bias voltage increases, potentially resulting in a resolution problem between parallel and antiparallel at sufficiently high bias. However, in the zero net field case of Figure 5-4B, it was not necessary to exceed 250 mV bias voltage to pin the device antiparallel. The antiparallel resistance at 250 mV was sufficiently greater than the parallel resistance to remain well-resolved.

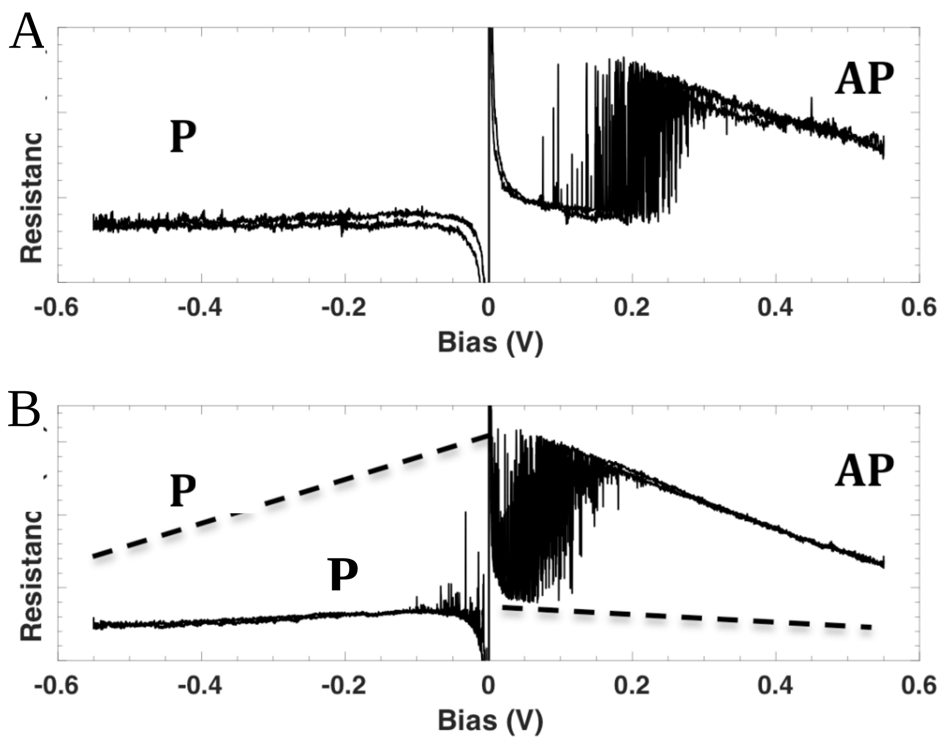

Figure 5-4. The resistance of the MTJ can be tuned from always parallel to always antiparallel using the applied bias voltage. Here the MTJ is 60 nm in diameter, and the voltage ramp rate is 0.5 V/s. A) With zero external field, the center of the switching region is around 200 mV. B) The switching region can be moved up and down in bias voltage using a constant external field to counter the magnetostatic field of the fixed layer, here 14 Oe. The discontinuity near zero bias is due to small offsets in the R9 system. Figure taken from [20]**.**

Time-domain measurements were performed at various bias voltages and are shown in Figure 5-5. The time-averaged current is reported here to give a sense of the critical switching current. This device transitions from saturated parallel to saturated antiparallel over a current range of just 253 µA. At -18 µA, the device is effectively saturated in the parallel state, with occasional, brief spikes to antiparallel. At 96 µA the time average of the resistance is about halfway between the parallel and antiparallel resistances. The average dwell time of the magnetization under these conditions is 2.7 µs. At 235 µA, the device is effectively saturated in the antiparallel state, again with short, unresolved spikes. In each case, the resistance is instantaneously parallel or antiparallel, but the time average can be tuned continuously.

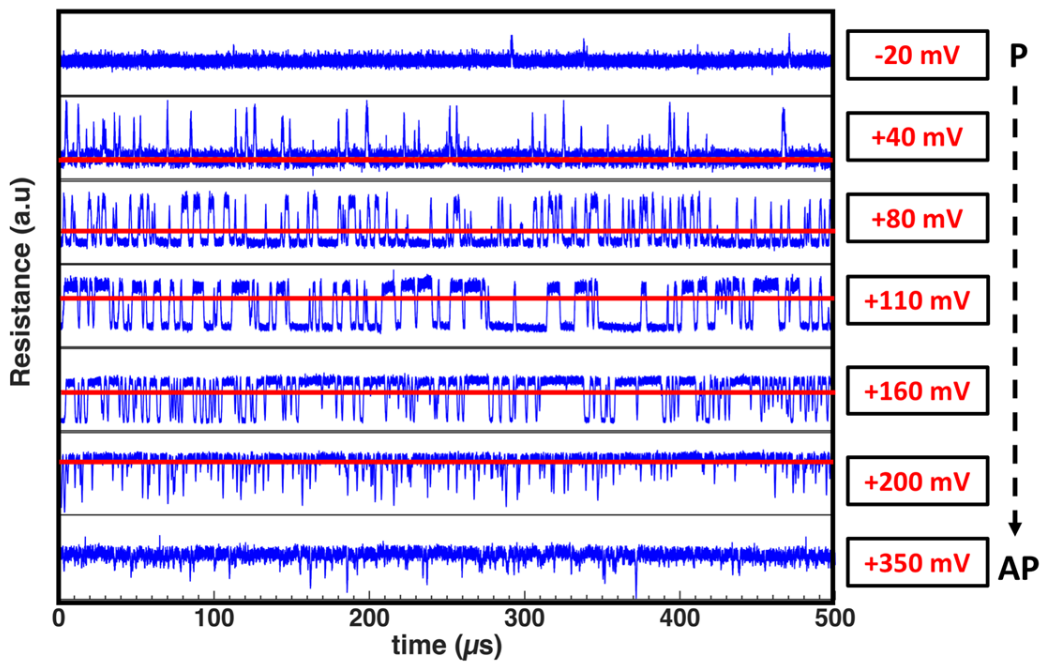

Figure 5-5. In the time domain, holding constant bias and cancelling the stray field results in magnetic telegraph noise that favors one state or the other based upon the amount of STT current. The red line shows the time average of the fluctuations shown in blue. The time-averaged current is shown on the right. Figure taken from [20]**.**

Figure 5-6 shows how the dwell times in the two resistance levels vary relative to one another as the STT current changes. At small negative current, the parallel dwell time is orders of magnitude larger than the antiparallel dwell time. The MTJ is effectively pinned in the parallel state. As the current increases, the dwell times exponentially increase and decrease for the parallel and antiparallel states, respectively. At 96 µA, the two dwell times are nearly equal, indicating that the probabilities of being in either of the two states are approximately equal. As the current continues to increase, the parallel state dwell time falls below the time resolution of the measurement, and the MTJ is effectively pinned antiparallel. The ability to tune the relative dwell times demonstrates the ability to tune the time-averaged resistance as well as to program the probability of parallel or antiparallel state in an instantaneous measurement.

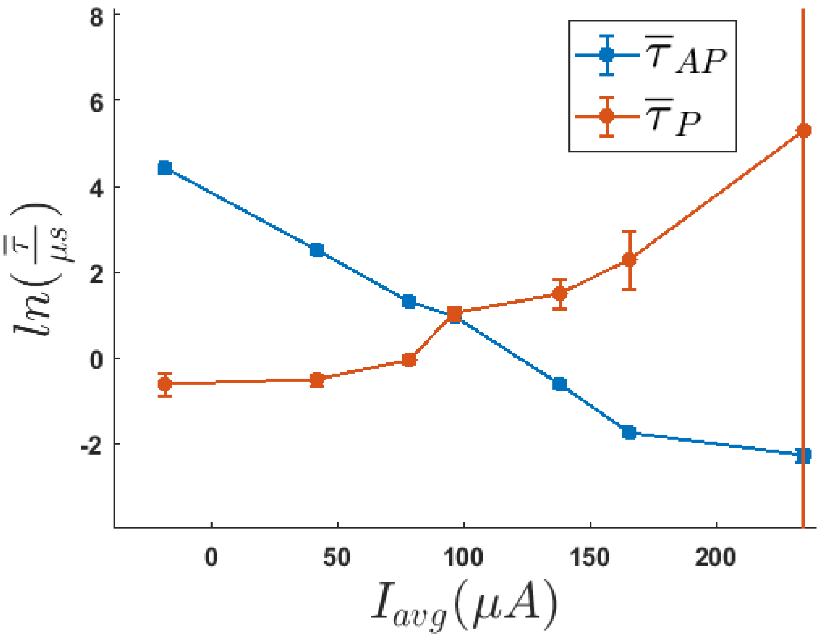

Figure 5-6. The average retention times in the parallel and antiparallel states are complements of one another. The crossing point of the retention times, or where the time averaged resistance is halfway between the parallel and antiparallel resistances, is approximately 100 µA. Figure taken from [20]**.**

5.5 Comparison to Theory

The control response of the MTJ device under test meets the requirements of the ideal MTJ-based stochastic logic device [38]. Figure 5-7 shows the properties of the device proposed in [38]. The state of the device is indicated here in terms of voltage out rather than resistance, but this is a simple matter of adding a comparator to the circuit. Figure 5-7A shows the sigmoidal time-averaged output response to the input bias voltage. The device switches stochastically between the two states, but it is influenced by the input bias such that the time-averaged state can be tuned from pinned parallel to pinned antiparallel with continuous, analog control between. Figure 5-7B shows the time domain signal switching between the parallel and antiparallel output voltage levels for different input biases. While the device stochastically switches between the two states for all three inputs shown, the time-average of the signal (shown in red) varies in a controllable way.

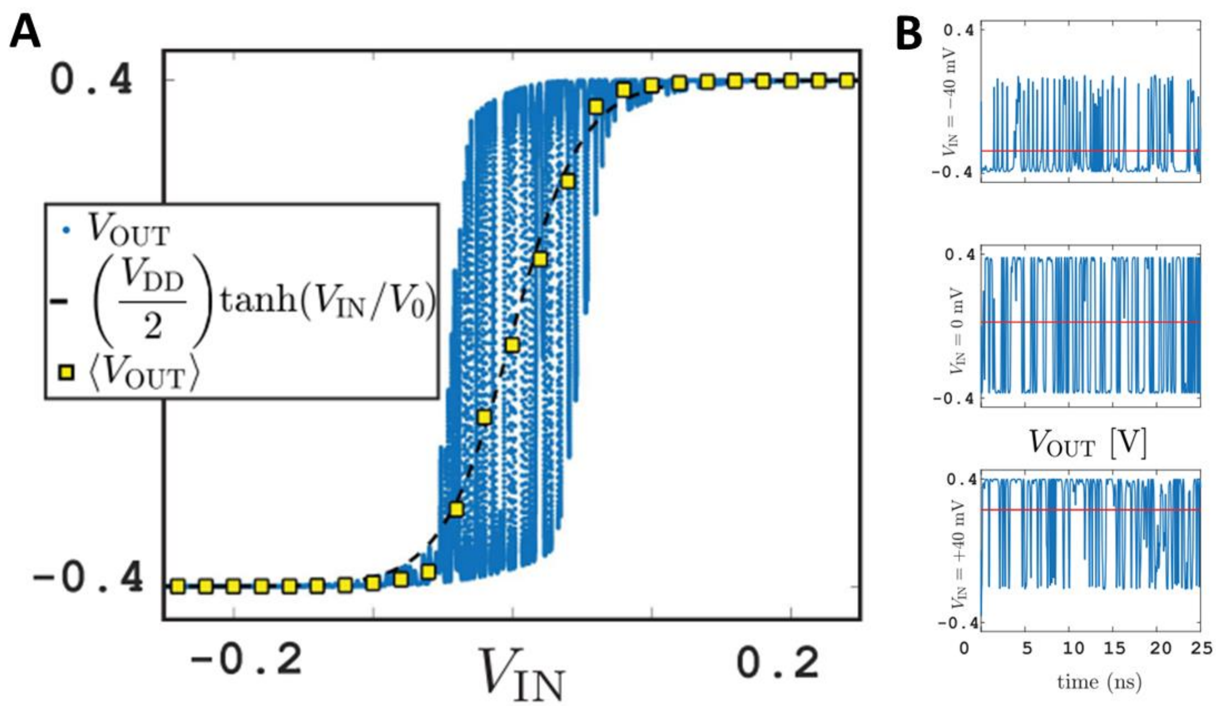

Figure 5-7. A) The voltage out vs voltage in for an ideal MTJ stochastic logic device. The device fluctuates stochastically, but the time-averaged voltage out follows a sigmoidal curve. B) Time domain simulations of the state of the MTJ show a fluctuating output with a stable time-average, shown in red. Figures taken from [38]**.**

5.6 Summary

Spin transfer torque was used to influence the preferred direction of magnetic telegraph noise in superparamagnetic MTJs. The STT control enabled analog control of the time-averaged magnetization direction of the magnetic free layer in the low-thermal stability MTJs while maintaining a well-resolved, two-state system in instantaneous measurement. These stochastically switching MTJs, influenced by STT current, fulfill the requirements for stochastic logic elements laid out by previous theoretical work [38]. The development of these two-terminal stochastic logic devices is an important milestone on the road to developing a stochastic computing architecture.

Chapter 6 Spin Transfer Torque and Spin Orbit Torque Control of a Stochastic Bit

This chapter compares pure STT control to hybrid STT/SOT control in a single superparamagnetic in-plane MTJ. I fabricated the device, performed the electronic measurements, and analyzed the data. This device again fit the requirements for stochastic logic put forth by theory. I determined that STT and SOT were roughly equivalent in this sample due to the low spin polarization in the film and the fact that STT and STT act in the same way on in-plane magnetized MTJs. This work was presented at the MMM/Intermag joint conference in Washington DC in January 2019.

6.1 Background

Spin orbit torque (SOT) is a catch-all term for the methods of using a charge current and the spin-orbit coupling in a metallic layer to generate torque on the magnetization in an adjacent layer [119]. Among these are the spin Hall effect and the Rashba effect [56,57]. In both cases, charge current passing through high atomic number metals experiences scattering due to the spin-orbit interaction. The spin-dependent scattering can be used to switch an adjacent ferromagnetic metal [50], [120]. The distinction between the two effects is largely between a bulk effect, the spin Hall effect, and an interface effect, the Rashba effect. The spin Hall effect generates spin current throughout the bulk of the conductor as the charge current passes through high atomic number metals [56]. Electrons are differentially scattered due to their spin interacting with the spin orbit coupling in the material. Since the charges scattered are equal, there is no charge current. However, there is a net spin current. The spin current dissipates over the material's spin coherence, or spin-flip, length, normally a few nanometers [6], [7]. The Rashba effect generates non-equilibrium spin densities in the surface states of the metal [57]. In either case, the torque acting on the adjacent ferromagnetic metal is proportional to the charge current density in the high spin orbit coupling metal [1], [2].

Spin transfer torque (STT) uses the spin polarization of the charge current passing through a magnetic tunnel junction (MTJ) to switch to magnetization direction of the free layer [47–49]. SOT offers many advantages over STT. Driving the high density STT current across a tunnel barrier can be highly dissipative, while the charge current for SOT passes through lower resistance metallic leads. Eliminating the need to drive large current densities across the tunnel barrier would improve energy efficiency and increase the possible number of write cycles before shorting the tunnel barrier due to the high current densities. SOT control also offers the advantage of separate read and write paths, so reading the state of device minimally effects the state itself.

Superparamagnetism is a phenomenon that occurs when the temperature of magnetic particles small enough to be monodomain is high enough so that the magnetization equilibrates on timescales that are short compared to the magnetization measurement [44]. In other words, the energy barrier to changes in the magnetization direction is no longer large compared to the thermal energy. When the energy barrier is sufficiently small, thermal fluctuations dominate the magnetization dynamics [45]. This description can be extended to patterned thin films, with the patterned island of ferromagnetic material now acting as the particle [55]. The electronic signature of a uniaxial superparamagnetic spintronic device was first measured in giant magnetoresistance (GMR) recording heads, and it resembled a type of noise found in other electronic systems called random telegraph noise [7,61]. In random telegraph noise, the signal randomly fluctuates between two levels, resembling the non-repeating off/on signal of a telegraph. When the random telegraph noise is produced by magnetization reversal, the signal switching is Poisson process. The more time that elapses since the previous switching event, the more likely a switch will occur.

Spin orbit torque has been studied as a means of influencing thermal magnetization fluctuations using optical methods [121]. The authors used Brillouin light scattering to observe magnetic fluctuations in a patterned permalloy disc on top of a current-carrying Pt lead. Using current densities on the order of 10^7 A/cm^2, they were able to drive switching modes on the order of gigahertz with a combination of Joule heating and spin current input. The authors were also able to separate equilibration of the magnetic disc to spin current from thermal equilibration. The spin current effects occurred on times scales shorter than 20 ns, while the thermal effects had a characteristic time around 90 ns.

Stochastic computing uses non-deterministically switching elements to sample the solution space of a given problem [40,122]. Stochastic computing offers advantages over deterministic computing in solving problems, such as prime factorization, which are extremely resource intensive using current computing paradigms [39,40,86,87]. To achieve stochastic computing, a logic element that is instantaneously digital but analog on average is needed [38]. In our previous work, we have shown that that spin transfer torque can be used to control the average resistance of a low thermal stability uniaxial magnetic tunnel junction. Those measurements showed thermal magnetization reversal rates on the order of megahertz with a current density on the order of $10^5 A/cm^2$ [20]. We have also shown deterministic SOT switching of 20 nm diameter perpendicularly magnetized MTJs. Here we show a comparison of spin transfer torque and spin orbit torque (SOT) control of random telegraph noise in in-plane magnetized superparamagnetic MTJs.

6.2 Nanofabrication

Xixiang Zhang's group at KAUST, particularly his post-doc Bin Fang, deposited films consisting of SiO_2/Ta (5)/CoFeB (2.5)/MgO (1)/CoFeB (2.5)/Ru (0.85)/CoFe (2.5)/IrMn (8)/Ru (10) where the numbers in parentheses are the thickness in nanometers. The IrMn layer pins the top CoFe layer which in turn pins the CoFeB reference layer. A 20 nm silicon nitride hard mask layer was added on top of the MTJ film for processing. The MTJ nanopillars were defined by electron beam lithography in a Sirion 600 SEM using hydrogen silsesquioxane (HSQ) resist. The pattern was transferred into the silicon nitride layer using CF_4/CHF_3 reactive ion etch, and then transferred to MTJ film by argon ion milling with endpoint detection. The Ta leads were defined by photolithography using AZ 4110 resist and then etched by argon ion milling. Wire bond pads were then defined by photolithography and deposited with 10 nm of Ta and 200 nm of Pt. With the free layer on the bottom of the tunnel barrier, we can control the magnetization of the free layer using SOT by passing a charge current through the bottom Ta layer while retaining the ability to switch by STT.

6.3 Conductive Atomic Force Microscope Measurements

The sample was measured in a RHK UHV 350 conductive atomic force microscope (CAFM), operated in air, with R9 control box. The tip of CAFM was coated with 10 nm of Ta for adhesion and 200 nm of Pt for electrical conduction and improved wear characteristics. The Pt wire bond pads were connected to platinum coated silicon chips that were soldered to macroscopic wires, one leading to the bias source for the R9 and the other to ground. A switch was placed in the path from the Ta lead to ground. A variable resistor, a decade box, was placed in the read path of the CAFM. Figure 6-1 shows a schematic of the CAFM, the MTJ pillar, and the measurement circuits.

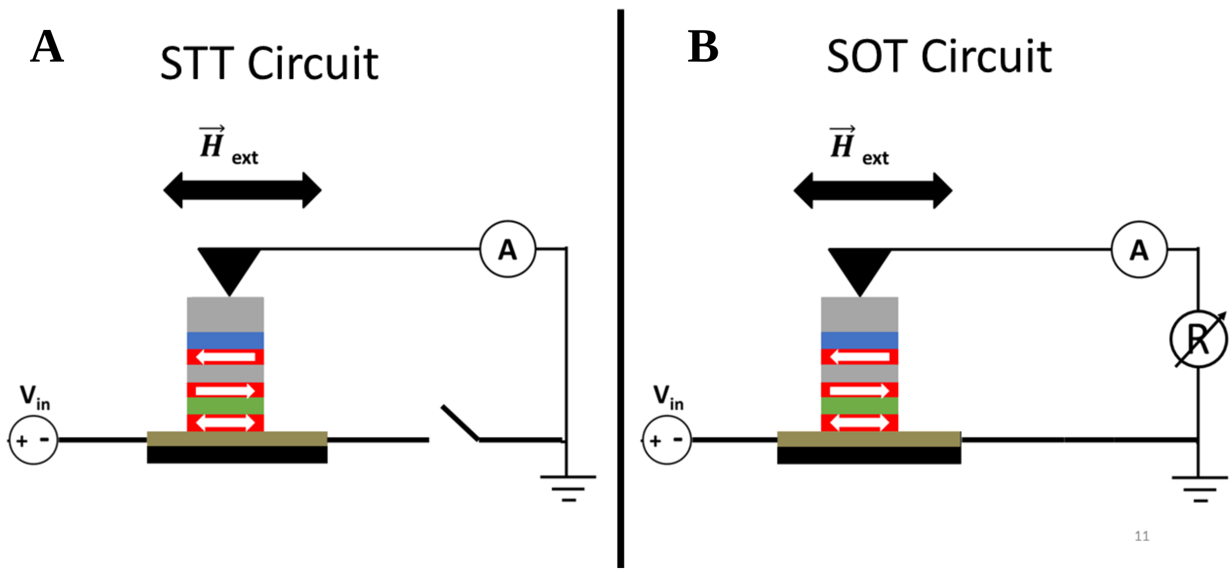

Figure 6-1. Electronic transport measurements were performed using a conductive AFM. A) In the STT case, voltage is sourced at the Ta bottom lead and the current passing through the MTJ to ground is measured. B) In the SOT case, voltage is again sourced at the Ta bottom lead, but now a variable resistor is placed in series with the MTJ and the opposite end of the Ta bottom lead is connected to ground. The resistor limits the read current through the MTJ and helps maximize the current density in the Ta bottom lead.

6.4 Magnetic Field Switching

Magnetic field switching measurements, like the one shown in Figure 6-2, were performed to determine the magnetostatic coupling between the fixed layers and the free layer. The magnetostatic coupling shifted the center of the magnetization loop, and thus influenced the free layer dynamics. The magnetostatic field was then cancelled using an external field during the STT and SOT switching experiments. Magnetic telegraph noise was also apparent near the switching fields, indicating that the energy barrier to switching this MTJ was low enough for the stochastic switching experiment.

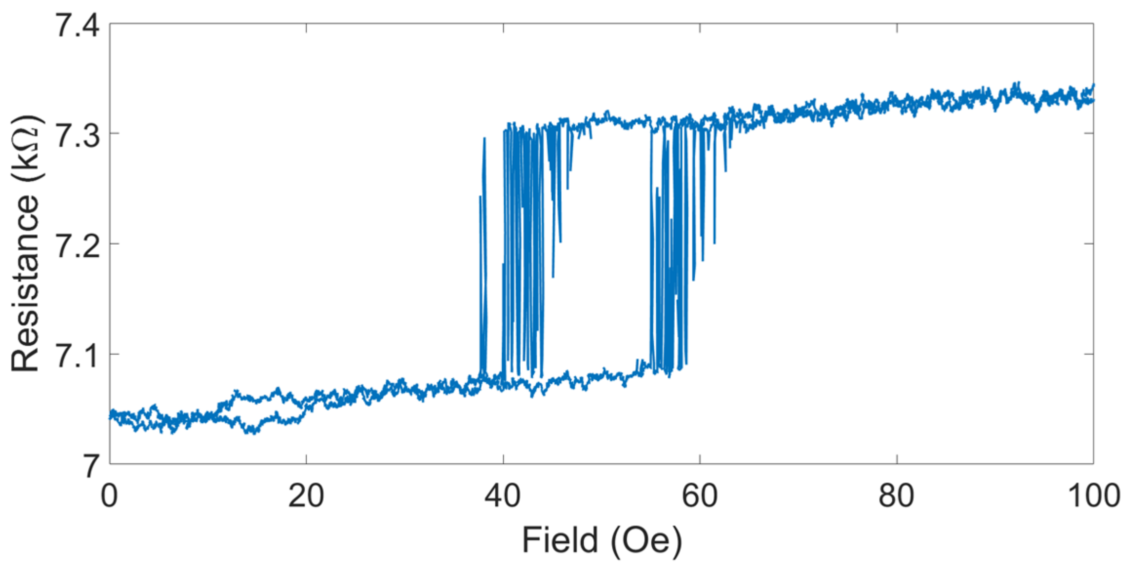

Figure 6-2. Field switching experiments are performed to determine the magnetostatic field from the fixed layer acting on the free layer. The field at the center of the hysteretic region, about 50 Oe, gives the magnitude of the magnetostatic field. That field will later be cancelled out using an electromagnet during electronic switching measurements.

6.5 Spin Transfer Torque Switching

With the magnetostatic field cancelled by the external field, the bias voltage was swept from +1.8 V to -1 V. As shown in Figure 6-3, the STT current drove the free layer magnetization from saturated parallel at high positive bias to a telegraphing condition with the midpoint of the average resistance at about +100 mV. There was a small range near zero where the difference between the parallel and antiparallel states was indistinguishable. This had no real effect on the average resistance because the magnetization dynamics were dominated by the intrinsic energy barrier of the device free layer; the current density in the MTJ was too small to drive the free layer magnetization. As the signal returned at negative bias, the moving average of the resistance continued to trend up to the antiparallel level. The resistance ultimately saturated at the antiparallel level at around -800 mV.

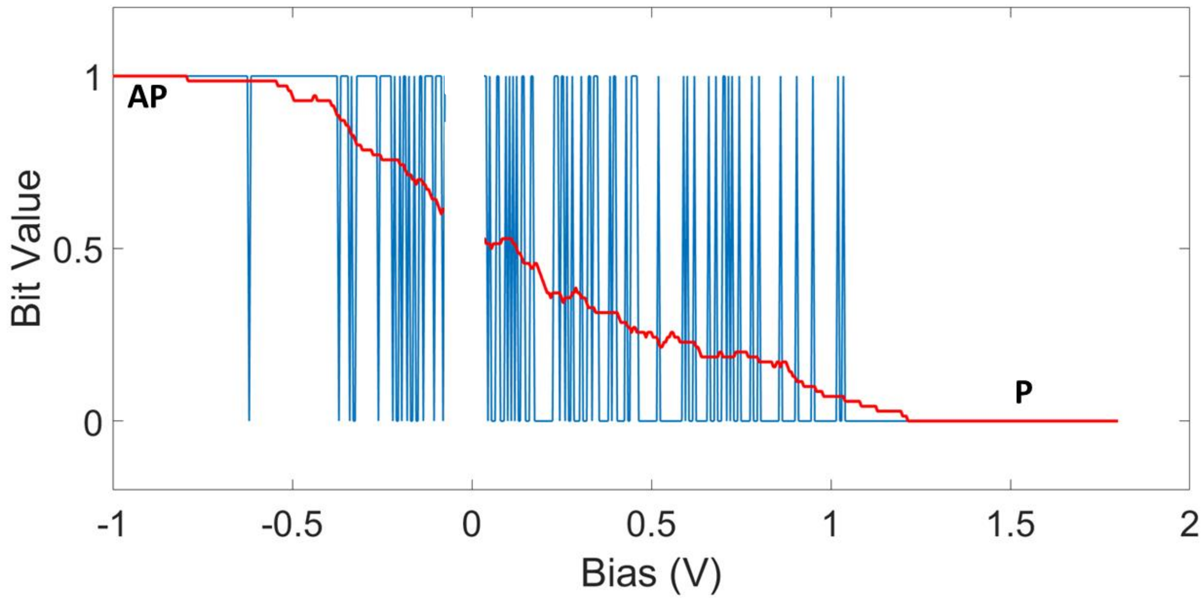

Figure 6-3. STT control drove the free layer magnetization from pinned antiparallel to pinned parallel over a range of about 2 V. The red line indicates the moving average.

6.6 Spin Orbit Torque Switching

Next, SOT switching was performed under the same field conditions as the STT switching. Figure 6-4 shows the result of the SOT experiment. Once again, the free layer magnetization favored the parallel direction when positive bias was applied and the antiparallel direction with negative applied bias. As with the STT experiment, there was a range near zero applied bias for which the signal was too small to measure. Unlike the STT case, the device was never pinned in the parallel or antiparallel state, despite using a much higher applied bias range, -8 V to +8 V. The resistivity of the bottom Ta lead was the primary factor limiting the use of SOT. In order to pin the device parallel or antiparallel, it was necessary to exceed the critical current density, J_c. The bias voltage, V_c, needed to achieve the critical current density can be found by Ohm's law.

$$V_c = I_c R = J_c A \times \frac{\rho l}{A} = J_c \rho l$$

where R is the lead resistance, I_c is the critical current, A is the cross-sectional area of the lead, ρ is the resistivity of the lead material, Ta in this case, and l is the length of the lead. The length of the Ta lead was reduced as much as practical, but the resistivity of the Ta was still too great for the available power supplies.

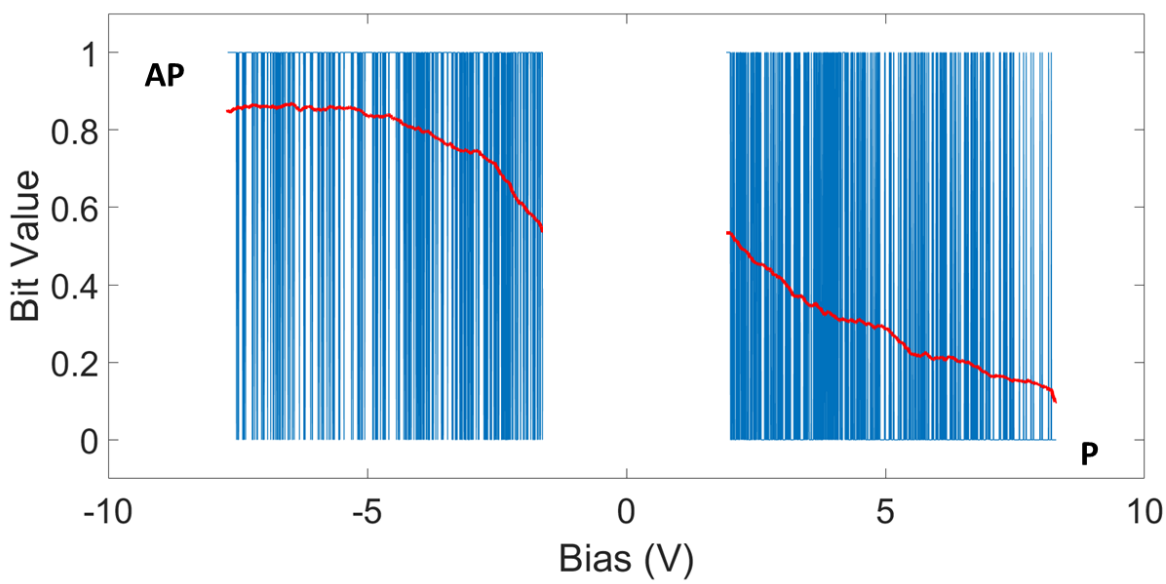

Figure 6-4. SOT control required higher bias voltage than STT to achieve critical current density, and the magnetization could not be fully saturated with the available power. The red line indicates the moving average.

Despite the inability to pin the MTJ into either state with SOT, a comparison was made using two different probabilities of finding the MTJ in the 1 (antiparallel) state. To achieve a probability of 0.85 using STT alone, the current density through the MTJ was $(1.35\pm0.06)\text{x}10^6\text{A/cm}^2$. In the STT/SOT hybrid case, the current density through the MTJ was $(1.11\pm0.04)\text{x}10^6\text{A/cm}^2$ and the current density through the Ta lead was $(2.26\pm0.02)\text{x}10^5\text{A/cm}^2$. For a probability of 0.2, the STT control mechanism used a current density of $(2.09\pm0.07)\text{x}10^6\text{A/cm}^2$ through the MTJ, while the hybrid mechanism used $(1.71\pm0.08)\text{x}10^6\text{A/cm}^2$ through the MTJ and $(2.84\pm0.02)\text{x}10^5\text{A/cm}^2$ through the Ta lead. For both the 0.85 probability and the 0.2 probability, the hybrid switching method achieved modest reductions in STT current density, approximately equal to the current density in the Ta lead. This is consistent with previous experiments which have found the critical current density for SOT to be roughly equivalent to that for STT [32], though it is at odds with others that have found a lower critical current density for STT switching [123].

6.7 Summary

The comparison of pure STT switching and hybrid STT/SOT switching found modest reductions in the current density needed to achieve equal probabilities of finding the MTJ in the antiparallel state. While the STT current density is reduced in the hybrid case, the reduction is too small to warrant the increased fabrication and measurement complexity of a three-terminal device. This experiment did provide another example of effective STT control of a stochastically switching MTJ, this time in a new film stack with the free layer on the bottom and the pinning antiferromagnet on top, in addition to our previous experiment [20]. It also determined the way forward for the next stochastic computing experiments in which we integrated two-terminal, STT controlled MTJs into logical circuits with feedback.

Chapter 7 Demonstration of Stochastic AND Gate with Hardware Feedback

Here I present an invertible stochastic AND operation performed using in-plane magnetized superparamagnetic MTJs as stochastic bits. This operation was performed successfully in both the forward and inverse directions, meaning that the output of the operation could be written and the inputs read to find the possible combinations leading to the desired output. This was all performed using hardware feedback rather than software and at much faster thermal reversal rates than others. It was also performed with the input bit probabilities skewed in a realistic manner rather than operating on purely random noise. I fabricated these devices and measured them with the assistance of Hao Chen. I completed these measurements in the basement of my home while the university was shut down for COVID-19. Hao Chen and Haolin Pan built the feedback circuit. Hao Chen also developed the pairwise comparison coefficient presented in this chapter. This work is currently in preparation for publication.

7.1 Background

Magnetic tunnel junctions (MTJs) are structures consisting of two ferromagnetic metals separated by an insulating tunnel barrier. MTJs leverage the tunnel magnetoresistance (TMR) effect to encode data. MTJs are two-level systems in which the electrical resistance is low when the two ferromagnetic layers' magnetic moments are parallel and high when the moments are antiparallel. High thermal stability MTJs are currently in use in the read/write heads of magnetic hard drives, in which the two resistance states of the MTJ are used as logical 1 and 0. Low thermal stability MTJs have been proposed for use in stochastic computing due to the thermodynamic nature of magnetization reversal, and their random telegraph noise output signal [38,40,61,86,87,107,124].

MTJs are said to have low thermal stability when the energy barrier to magnetization reversal is low compared to the thermal energy. Low thermal stability MTJs switch between the antiparallel and parallel states stochastically on timescales that are relevant to measurement [33,44,45,63,125]. The relevant timescales can be years for data storage applications, seconds for magnetometry measurements, or sub-milliseconds in spin logic. The time an MTJ spends in one state, called the dwell time, depends exponentially on the energy barrier to switching. The energy barrier to switching can be modified using voltage controlled magnetic anisotropy [18,126] and hard axis magnetic fields.

MTJ switch stochastically between two resistance levels, so the resistance is instantaneously digital yet analog in time average. The digital values are fixed to the parallel and antiparallel resistances, but the analog time average resistance can be controlled using any of the typical spintronic means of controlling magnetization, namely spin transfer torque (STT) [29], spin orbit torque (SOT), and external magnetic field [24]. Each control mechanism has its advantages and disadvantages. STT uses high current densities driven across the MTJ’s tunnel barrier to reverse the magnetization [47–49]. STT devices are subject to faster degradation than those using other control mechanisms, because driving large current densities across the high resistance tunnel barrier eventually results in dielectric breakdown [36,66]. The advantage of STT is that it can be used in any two-terminal MTJ that can sustain the high current densities required to switch, on the order of 10^6 A/cm^2, and the bias voltage required to drive them across the tunnel barrier. SOT requires specific material choices, namely high atomic number metals directly adjacent to the ferromagnetic free layer, with large charge current density passing through the heavy metal perpendicular the MTJ, hence three terminal device architecture [32,50,56,57]. The advantage of SOT is that it does not require large current densities to be driven across the high-resistance tunnel barrier. Similar current densities are required in the heavy metal leads to perform SOT switching, but there is no high resistance tunnel barrier contributing to Joule heating loss. External magnetic fields are difficult to confine to individual devices at the densities needed in commercially viable products, and field-controlled devices require four terminals due to the separate read and write paths. Field-controlled devices also do not require high current densities in any part of the device [19,24,107].

The invention of the AND gate is credited to Walther Bothe for his method of detecting coincident particles in a Compton scattering experiment [127]. His coincidence circuit required high voltage at all inputs for it to output high voltage. Similarly, the logical AND operation takes two binary inputs and provides a single binary output. For the AND to return 1, or "true", both inputs must be 1. Otherwise, the AND gate returns 0. Since the operation uses three bits, two inputs and an output, there are 2^3 possible combinations. The four possible states not included in the truth table are error states. The AND gate truth table is shown below in Table 7.1

Table 7.1. The AND gate truth table contains four possible combinations of two inputs and one output. The AND gate returns 1 only when the two inputs are both 1. Otherwise, it returns 0. The remaining four possible combinations not shown here are error states.

Input 1	Input 2	Output
0	0	0
1	0	0
0	1	0
1	1	1

In stochastic logic, the output is represented by a physical bit just like the two inputs [38,86]. All three bits switch stochastically according to Poisson statistics [33]. The dwell time of each bit in a particular state, τ, is given by

$$\tau = \tau_0 \mathrm{e}^{\frac{\Delta}{\mathrm{k_B} T}}$$

where τ_0 is the time between reversal attempts, 1 ns in this case, Δ is the energy barrier to switching, k_B is the Boltzmann constant, and T is the temperature. The preference of each physical bit for either logical value is independently controlled. The stochastic switching is used to sample the space of possible combinations of the three bits. For a stochastic AND gate, a feedback circuit networks the bits together in such a way that the four error states all have higher energy than the four states in the AND gate truth table. The modification of the relative energies of the total system states also enables invertible logic. In a traditional Boolean logic operation, the inputs are written, and the output is read. In invertible logic, the output is written, and the inputs are read. The inputs stochastically switch between the different combinations that can result in the written output [86]. It is this invertibility that makes stochastic logic so potentially powerful.

The ability to sample the space of possible input combinations that lead to a particular output enables some of the computing operations normally associated with quantum computing [40,128–131]. In quantum computing, adiabatic optimization is used to solve combinatorial search problems that expand factorially or exponentially with the addition of each bit [128,129]. Adiabatic optimization uses a similar mechanism as that described above with the ground state of the total system prepared as the desired output and the states of the individual quantum bits representing the combinations that result in the desired output [128]. A quantum computer should be less prone to becoming trapped in a metastable, high energy state than a stochastic computer because the quantum bits can tunnel through an intervening energy barrier [132]. Quantum bits sample the entire solution space simultaneously. In practice, the low-lying excited state problem persists in quantum computing and necessitates performing the quantum calculation many times to arrive at a statistical result, as is the case in stochastic computing [133]. Stochastic computing offers a less sophisticated, but also much less expensive, means of solving combinatorial search problems in a classical system at room temperature [38,86]. Here we present a result for one such invertible stochastic logic circuit using low thermal stability MTJs as the stochastic element with STT write and feedback control.

7.2 Nanofabrication

Films consisting of SiOx/Ta (5)/CoFeB (2.5)/MgO (1)/CoFeB (2.5)/Ru (0.85)/CoFe (2.5)/IrMn (8)/Ru (10), where the numbers in parentheses indicate the film thickness in nanometers, were deposited by Xixiang Zhang's group at King Abdullah University of Science and Technology (KAUST). The magnetic layers were magnetized in-plane, with the IrMn pinning the CoFe layer. The CoFe and top CoFeB layer formed a synthetic antiferromagnet, thus fixing the reference layer. The bottom CoFeB acted as the free layer. The film was patterned into 60 nm by 90 nm ellipses by electron beam lithography and argon ion milling, with the long axis of the ellipse parallel to the pinning direction of the antiferromagnetic IrMn layer. The elliptical shape was intended to ensure a two-state system while the low aspect ratio kept the energy barrier to switching small enough for the MTJ to thermally switch. The bottom Ta layer was patterned into cross-shaped leads before the whole stack was passivated with SiN_x. Photolithography and reactive ion etching were used to expose the Ru top electrode and a small area at the end of each of the bottom Ta leads. Pt leads were then deposited to form the read and write paths. Figure 7-1 shows a schematic of the as-deposited film and a finished device.

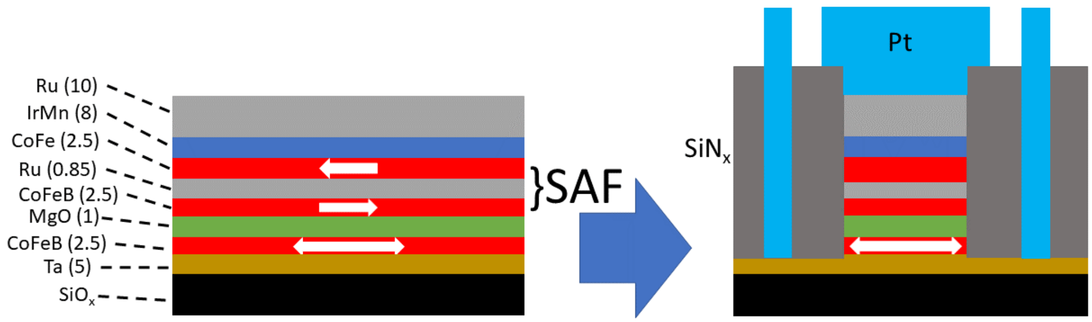

Figure 7-1. The MTJ film was deposited by Xixiang Zhang's group at KAUST. The films were fabricated into hardwired MTJs with Pt leads and SiN_x passivation.

7.3 Modular Circuit

The test circuit for the invertible logic was modular in design such that it could be scaled to many bits. The MTJ unit consisted of a subtractor to set the input bias, a Wheatstone bridge to sense the state of the MTJ, and a comparator to digitize the signal. Figure 7-2 is a schematic of one of these MTJ modules. The circuit work in this experiment was done primarily by Haolin

Pan, a summer exchange student from the University of Science and Technology of China (USTC), and Hao Chen, another graduate student in the group.

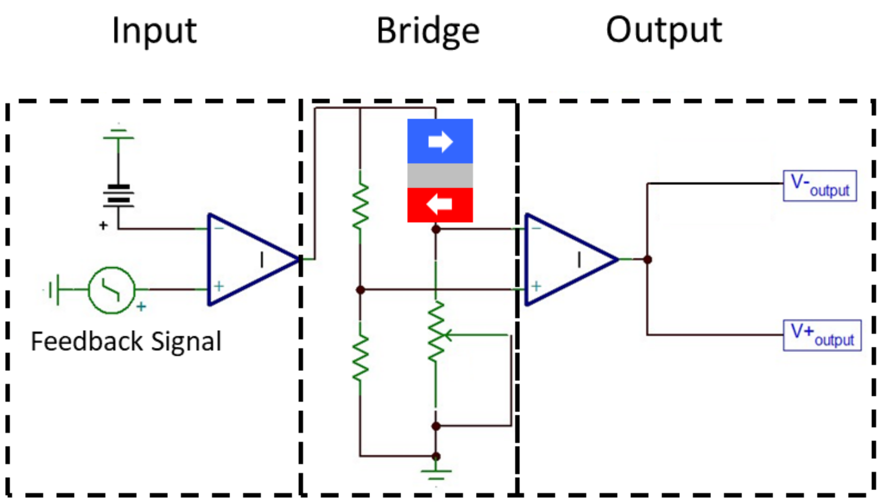

Figure 7-2. The modular circuit consists of a subtractor to combine the programming bias with the feedback signal, a Wheatstone bridge to sense the device state, and a comparator to digitize the output.

The MTJ dies were clamped in position and connected to their circuit modules. The MTJs were placed in the field of a NdFeB permanent magnet applied perpendicular to the MTJ easy axis. This perpendicular field was used to further destabilize the magnetic free layer of the MTJ. As shown in Figure 7-3, the average dwell time of one device was tuned from 200 μs to 1.65 μs using a small external field of 26.5±0.1 Oe to achieve the shortest dwell time. This corresponded to a reduction of the energy barrier to switching from 18 k_BT to 7.4 k_BT. The average dwell time would need to be further reduced by several orders of magnitude to achieve the speeds used in the theoretical literature [38,124], and this perpendicular field method may be one method to achieve those speeds. Others have recently achieved thermal magnetization reversal with dwell times as short as 8 ns [67].

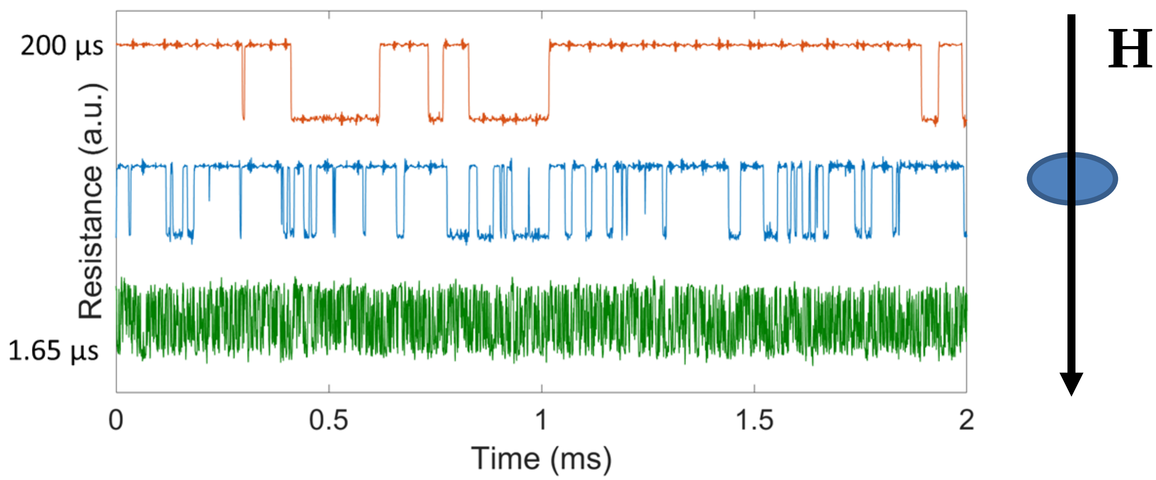

Figure 7-3. A small hard axis magnetic field reduced the resistance dwell time by more than two orders of magnitude. Using a constant field of 14 Oe, the average dwell time was 200 µs. Increasing the field to 26.5 Oe reduced the average dwell time to 1.65 µs.

The MTJ resistance data was read out simultaneously by triggered measurement using Red Pitaya STEMLab boards. Figure 7-4 shows a schematic of the triggered measurement circuit. Upon receiving the voltage pulse, the STEMLab boards recorded the output of the MTJ modules using their onboard oscilloscope function. The boards were set up using Standard Commands for Programmable Instruments (SCPI) protocol and ran a data recording program written by Thomas Wong, a former undergraduate in our group. The device state was recorded for various input bias values to establish the voltage control sigmoid for each device.

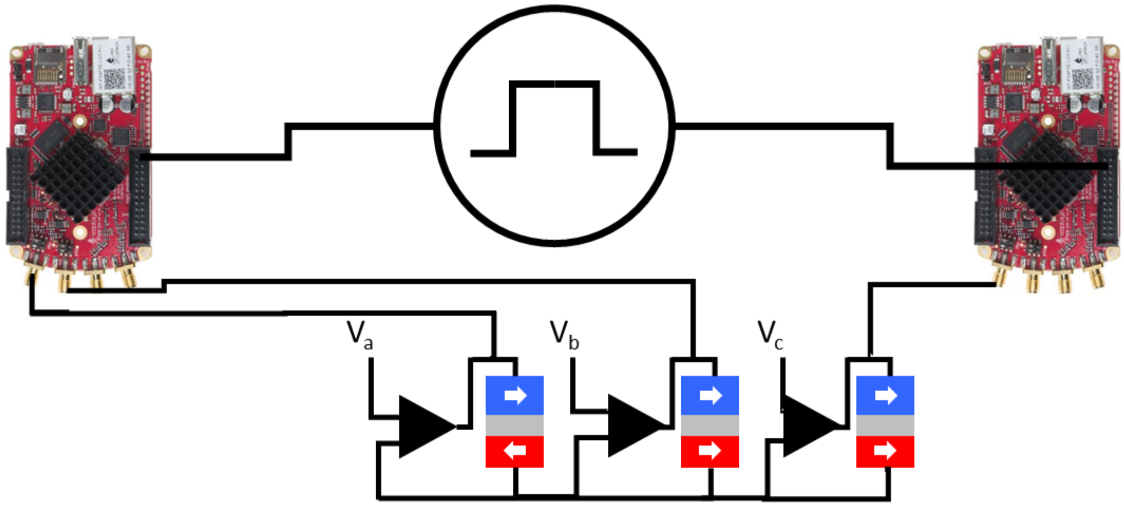

Figure 7-4. The time domain measurements of the two or three devices states were measured using Red Pitaya STEMLab boards. The signals were collected simultaneously by triggering the boards using a pulse generator.

The MTJs used in this experiment exhibited sigmoidal control using STT control. A fixed programming bias was applied to the device to set the probability of finding the device in the logical 1 state. A 50 mV feedback bias signal was added to or subtracted from the programming bias, as shown in Figure 7-5. The feedback signal moved the probability of the logical 1 up and down the sigmoid as necessary to satisfy the AND condition. Data was collected for a given programming bias value both with and without the feedback connected.

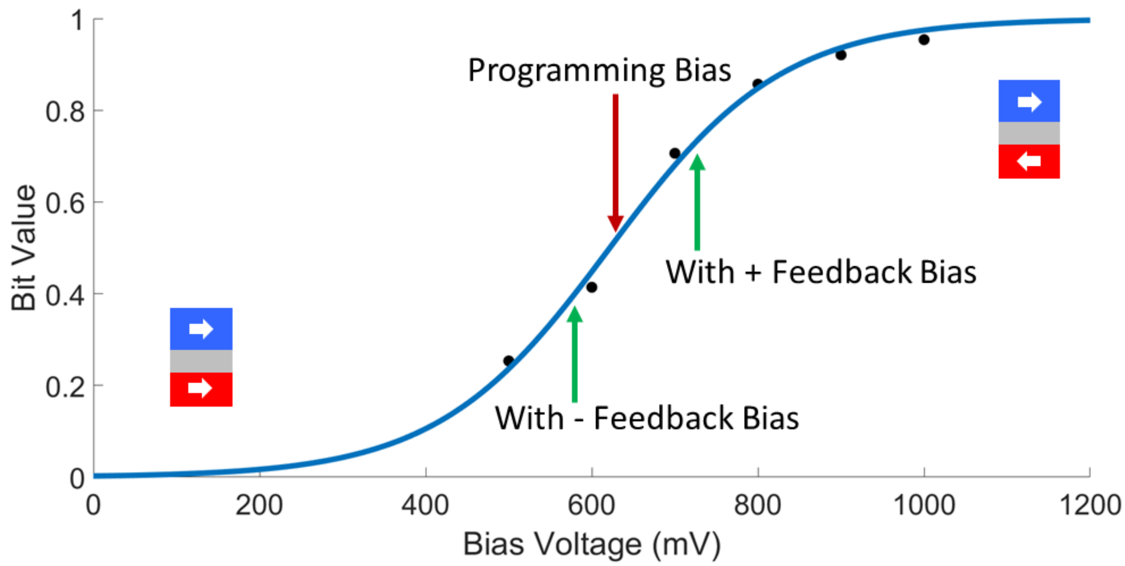

Figure 7-5. The programming bias set the averaging state of the device by choosing a bias along the MTJ's control sigmoid to which the 50 mV feedback signal was added or subtracted. The MTJ's parallel state was defined as logical 0 and the antiparallel state as logical 1. The error bars in this measurement are smaller than the points in the plot because of the large number of measurements used in the calculation.

Controlled NOT Measurement

To test the effectiveness of the feedback, two MTJ modules were connected such that they would prefer to be in opposite states from one another. This may be called a controlled NOT gate. This controlled NOT differs from an XOR in the number of bits involved. An XOR in this scheme would require three bits, two inputs and an output. The truth table of an XOR would include both true and false results. This controlled NOT can be thought of as an XOR where the output is fixed to true. The truth tables for an XOR and a controlled NOT are shown below in Table 7.2.

Table 7.2. An XOR is a logic gate that has two binary inputs and a binary output. The XOR returns "true", or 1, when the two inputs are different and "false", or 0, when the inputs are the same. A controlled NOT is a two bit operation in which feedback is used

XOR			Controlled NOT	
Input 1	Input 2	Output	Bit 1	Bit 2
0	1	1	0	1
1	0	1	1	0
0	0	0	N/A	
1	1	0	N/A	

The controlled NOT worked by directly connecting the inverting output of each bit to the feedback input of the other, as shown in Figure 7-6. When one bit jumps to the antiparallel state, the voltage from the inverting output drops to the low voltage pole. The low voltage input to the feedback of the next module shifted the bias across the MTJ lower, toward the parallel state. The output from the second module's inverting output was then high. The high voltage input to the feedback terminal of the first device shifted the bias across the first MTJ higher, toward the antiparallel state.

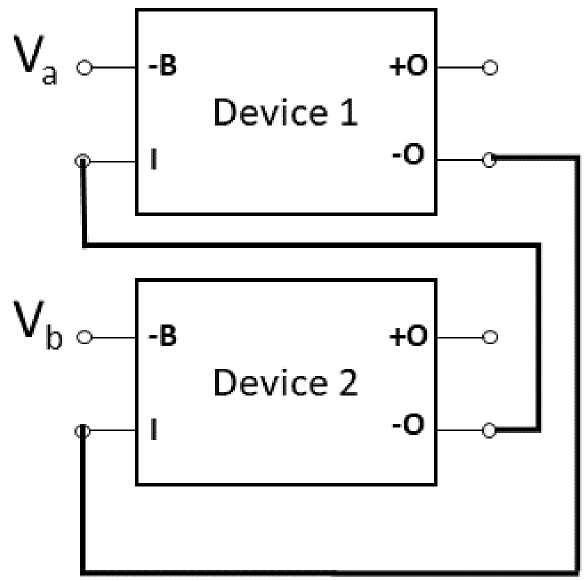

Figure 7-6. The controlled NOT operation was performed by connecting the inverting outputs of each MTJ module to the feedback input on the other module.

First, the module outputs were measured in the time domain with the feedback off. The two uncoupled devices reversed thermally on different time scales, as shown in Figure 7-7. Device 1 had greater electronic noise in the parallel state than device 2. When the feedback was turned on, the device outputs showed the opposite states with very little lag time between them. The coupled devices' outputs were strongly correlated because of the bias voltage feedback mechanism. Even the electronic noise in device 1 was coupled to device 2 and appeared in both coupled output signals. The two coupled devices spent 98.2% of the time of the measurement satisfying the NOT condition. The average duration of errors in the controlled NOT was 2.3±0.3 μs. Given the short error duration and small error rate, an averaging time of ten times the error duration, or 23 µs, should be sufficient to arrive at a statistical conclusion. With the effectiveness of the feedback confirmed, the next operation to study was the AND gate.

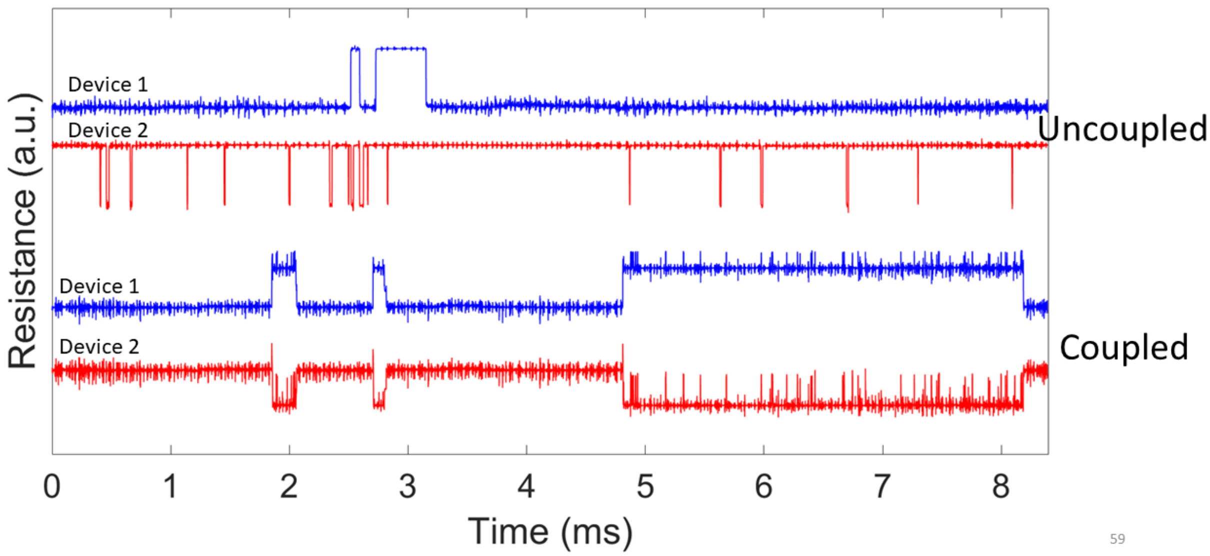

Figure 7-7. The controlled NOT test showed the effectiveness of the feedback mechanism. When the devices are uncoupled (top), they fluctuated independently on different timescales. When the devices are coupled by the feedback signal (bottom), their states were strongly correlated.

7.4 AND Gate Measurement

Three of these MTJ modules were connected by a logic circuit that generated the feedback signal between the MTJs, as shown in Figure 7-8. The three modules' programming biases were controlled independently while the feedback amplitude was fixed to 50 mV for all devices. The three modules were labelled x_1, x_2, and y. The x_1 and x_2 modules were the input bits to the AND operation, and the y module was the output. The modules had inverting and noninverting outputs, labelled -O and +O in Figure 7-8. The inverting output was the opposite of the noninverting output. The inverting output of module x_1 and the non-inverting output of module x_2 were input to a CMOS NOR gate. A NOR gate outputs 1 when both inputs are 0 and 0 for all other cases. The output of - x_1 NOR x_2 was 1 if x_1=1 and x_2=0; otherwise, the NOR returned 0. The output of x_1 NOR x_2 was input to an XOR with the noninverting output of module y. An XOR returns 1 when the inputs are opposite of one another and 0 when they are the same. Thus, the output of this XOR was 1 when x_1=1, x_2=0, and y=0, for example. Likewise, the output of the XOR was 0 for x_1=1, x_2=0, and y=1. The output of this XOR was then connected to the feedback input of the module. Logical 1 at the XOR output corresponded to +50 mV feedback, and logical 0 corresponded to -50 mV. Therefore, in the example case of 1, 0, 0, the feedback would add 50 mV to the programming bias of the x_1 module, maintaining it in the 1 state. In the 1,0,1 case, the feedback would subtract 50 mV from the programming bias and drive the device toward the 0 state. The feedback circuit was constructed similarly for the other two modules as shown in Figure 7-8.

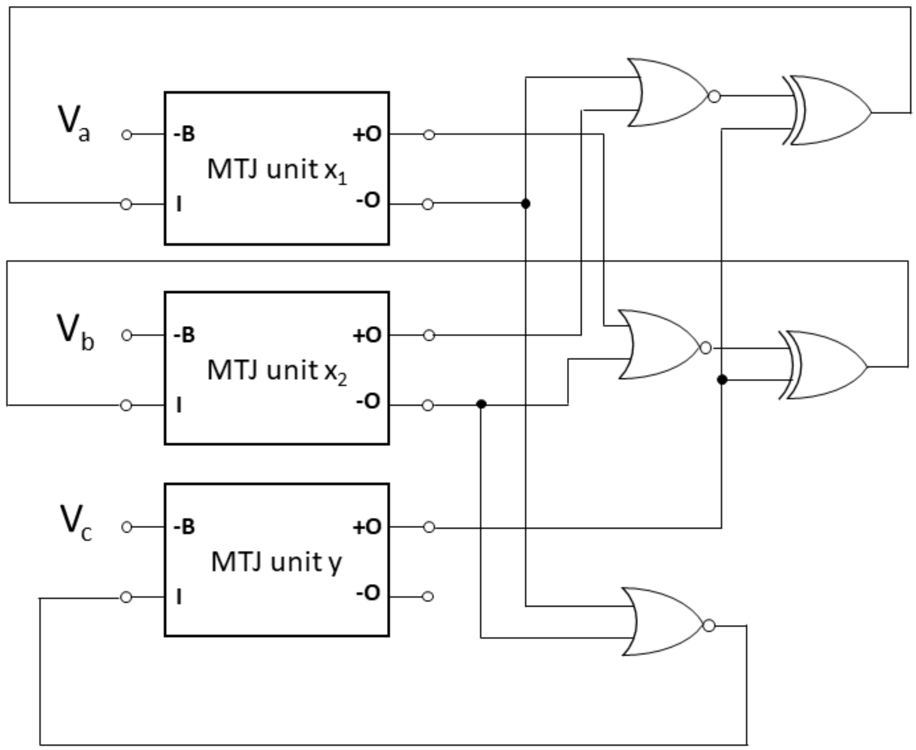

Figure 7-8. The MTJ modules were further connected to a feedback network with independently controlled programming biases for each module. The programming bias is input with opposite sign to the port labelled -B. It was subtracted from the feedback signal, input at port I, as shown in Figure 7-2. The +O port was the non-inverting output from the MTJ module, and the -O port was the inverting output.

Three 60 x 90 nm CoFeB MTJs were connected to the logical circuit, and their resistances over time were measured simultaneously using the triggered Red Pitaya STEMLab boards as with the controlled NOT demonstration. The results of some of these measurements are shown in Figure 7-9 with AND gate feedback on. The three-bit system spends most of its time satisfying the AND condition (shown in green) with less time spent in other states (shown in red). The system began the measurement in the 110 state, which is not an element of the AND gate truth table. After some lag time, likely increased here compared to the controlled NOT measurement by the added feedback components, x_1 switched to 0 under the influence of negative feedback bias, satisfying the AND condition. Module x_2 then thermally switches to 0. This released the negative feedback on module x_1 and allowed it to freely switch between 1 and 0 since 100 and 000 are both elements of the AND gate truth table. About 17 μs into the measurement, module y switched to 1 almost simultaneously with x_2 switching to 1. This maintained the AND condition. At about 19 μs, module y returns to the 0 state, putting the system in 110. Module x_1 then switches to 0 to return to a state in the AND truth table. This proved to be unstable, so x_1 returned to 1. Module y then switched to 1, and the system remained in the metastable 111 state for more than 10 μs. Module x_1 then thermally switched to 0, putting the system in 011. The feedback then forced x_1 back to 1. At about 43 μs, module y thermally switched to 0. There was again a lag time before x_1 switches to 0. The measurement finished with a brief thermal switch of x_1 to 1 before returning to 0. Overall, the system spent 67% of the measurement time in AND states.

The times for which the system was not satisfying the AND condition, the times when the system was in error, were more clustered than the times for which the system was satisfying the AND condition. For the data shown in Figure 7-9, the average time spent in an instance of an AND error state was 2.6±1.7 μs. This average time may have been the approximate lag time in the feedback circuit, particularly since it so closely matches the error duration from the controlled NOT. The variance in these times was caused by the variance in MTJ energy barriers to switching, and therefore the steepness of the control sigmoid. The fact that the error states all occurred with x_2=1 indicates that the programming bias for x_2 was higher than the midpoint of its control sigmoid.

The three modules slewed between 0 and 1 on different timescales, yet the total system spent most of its time satisfying the AND condition. The different timescales were important because they helped to show that the three bits were indeed switching stochastically rather than being driven in a forced oscillation. If the timescales were too closely matched, it would have been difficult to argue that the switching was truly stochastic except the influence of the feedback network rather than driven by a clock signal with a much larger amplitude than the 50 mV feedback used here.

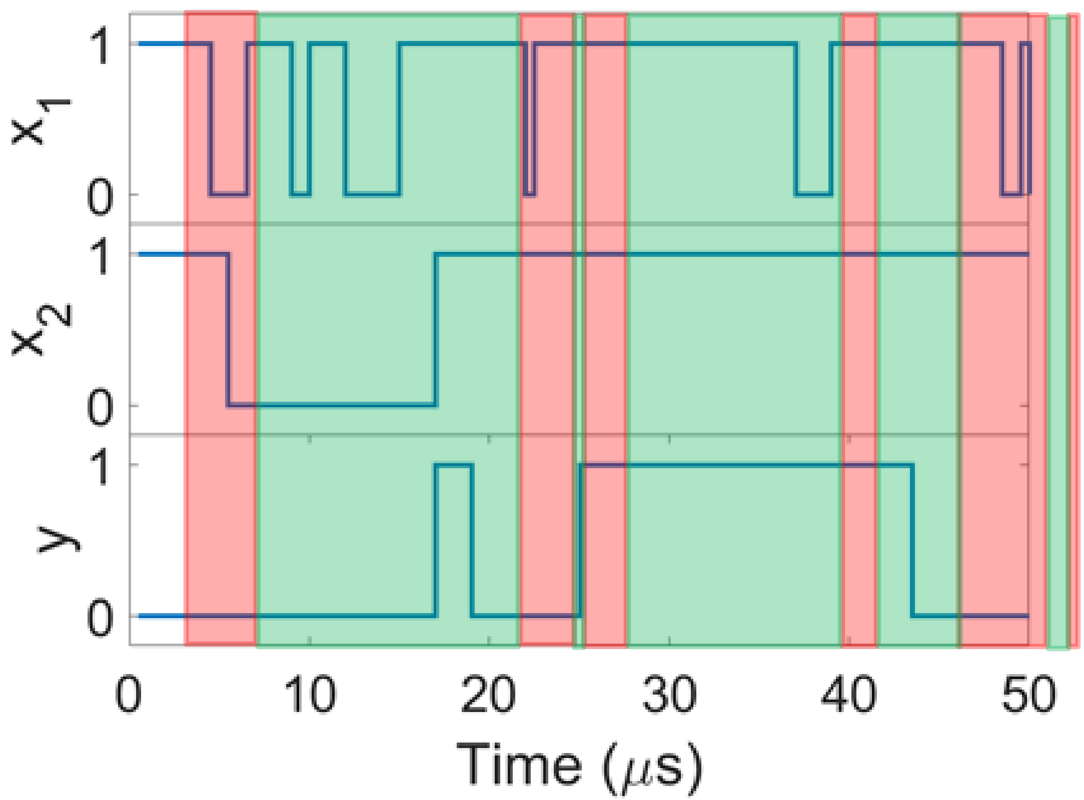

Figure 7-9. The binary outputs of three superparamagnetic MTJs connected to a logical circuit were read simultaneously with sub-microsecond time resolution. The data shown here was collected with feedback connected, but with the output bit, y, allowed to fluctuate. The three devices spend most of the time satisfying the AND condition (green) with less time spent in error states (red).

Stochastic logic has some unique errors. A certain amount of noise and write error is a necessary part of stochastic logic. The probabilistic results require time averaging over many stochastic switches before converging to the correct end state or set of end states. To be useful for real problems, the logic circuit must be able to operate with arbitrary probabilities set on each of the stochastic bits. However, if the preference of any single bit for one logical value becomes too great, the entire circuit can become trapped in one metastable state for long periods of time. The likelihood of errors increases as more bits are added to the operation. Note the deterministic nature of the controlled NOT shown in Figure 7-7 compared to the 33% error states shown in Figure 7-9. Measuring the relative probability of system states rather than their absolute probability can help to overcome the effect of individual bit preference while also suppressing the effect of write errors [40].

The probabilities P of the eight possible microstates (x_1,x_2,y) were defined as the ratio of the total time spent in the given state divided by the total measurement time. The probabilities were analyzed pairwise. We denoted by (0,0) the state 000 that was consistent with the truth table of an AND gate together with 001 that was not. The preference for 001 relative to 000 was defined by the function

$$\mathrm{C}(\mathrm{x}_1 = 0, \mathrm{x}_2 = 0) = \frac{P(x_1=0,x_2=0,y=1)-P(x_1=0,x_2=0,y=0)}{P(x_1=0,x_2=0,y=1)+P(x_1=0,x_2=0,y=0)} .$$

After connecting feedback, when $\mathrm{x}_1 = x_2 = 0$, P(000) will increase and P(001) will become smaller, effectively decreasing C(0,0). The condition would be the same for C(0,1) and C(1,0) but not C(1,1), since P(111) increases but P(110) decreases. Figure 7-10 shows experimental results with the feedback connected, showing a statistical preference for valid AND gate states. A more negative C(0,0) value indicates P(000) was greater than P(001). Similarly, a more negative C(0,1) was a result of P(010)>P(011), and a negative C(1,0) means P(100)>P(101). C(1,1) should have been positive because P(111)>P(110), and that was the measured result. The weakest effect of the feedback was C(1,0)=-0.1. This was again a result of x_2's programming bias favoring the x_2=1 state. However, the fact that C(1,0) was still negative despite the skewed x_2 probability showed the ability of the feedback scheme to operate in realistic conditions. If the AND gate only worked with all inputs set to 0.5, it would not be useful for real calculations in which the inputs favor one value or the other.

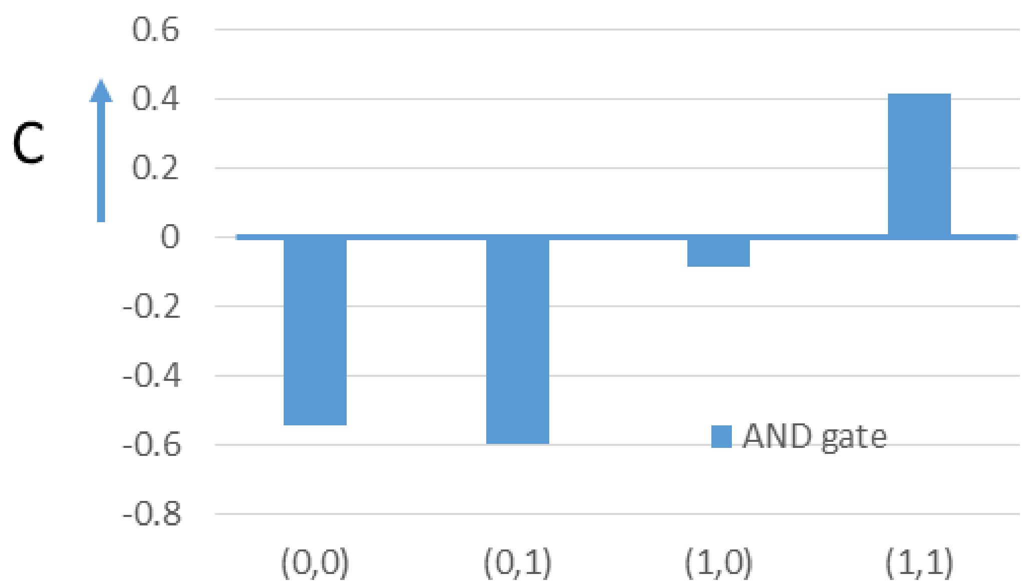

Figure 7-10. When the output bit, y, can fluctuate freely, all four states in the AND gate truth table become more likely. The three negative C values indicate the y=0 states became less likely for C(x_1,x_2) than the corresponding y=1 states. The positive C value represents the one y=1 state in the AND gate truth table, 111.

7.5 Invertibility

Invertibility is based on what happens when the output is pinned to a particular value. The output bit, y, was pinned by applying a programming bias near the ends of the control sigmoid like the one shown in Figure 7-5. When the average bit value was set to less than 0.1 or greater than 0.9, the module was said to be "pinned" to 0 or 1, respectively. Pinning the output and measuring the inputs amounts to asking, "Given the output of 1 or 0, what are the most likely combinations of inputs?" This can be further modified to finding the marginal probabilities for different combinations of inputs given known probabilities for some of the inputs, set by the programming bias at the input bits. Pinning y to 1 increased the probabilities for all the states with y = 1 (Figure 7-11a), while pinning y to 0 increased the probability for all the states with y = 0 (Figure 7-11b).

Only one state in the AND gate truth table has y=1, the 111 state. In Figure 7-11a, C(1,1) dominates because the 111 state was by far the most likely in the measurement. The three-bit system spent most of its time in the 111 state. C(0,0) and C(1,0) became positive in this measurement because the effect of pinning y to 1 was stronger than the 50 mV feedback. In a broader application, thresholding or a ratio of C values would be used to find that 111 was the correct answer to the y pinned to 1 problem. The y pinned to 1 case has only one appropriate input combination, but this was not the case when y was pinned to 0.

The y pinned to 0 case is more interesting than the y pinned to 1 case because there are three y=0 AND states rather than the one y=1 AND state. When y was pinned to 0, the probability of all the y=0 states increased. The feedback circuitry further increased the probability of the y=0 states in the AND gate truth table and suppressed the one y=0 state that is not in the truth table. Figure 7-11b shows the result of the y pinned to 0 measurement. The C values for the first three pairs of states, C(0,0), C(0,1), and C(1,0), were all less than -0.8. The more negative C values indicate a higher probability of the AND states 000, 100, and 010 than their pairwise counterparts. C(1,1) also became negative because 110 became more likely than 111 with y pinned to 0. However, C(1,1) is sufficiently greater than the other C values that thresholding or a comparison of C value ratios would provide sufficient contrast for a machine to exclude the 110 state as a reasonable answer to the y pinned to 0 problem.

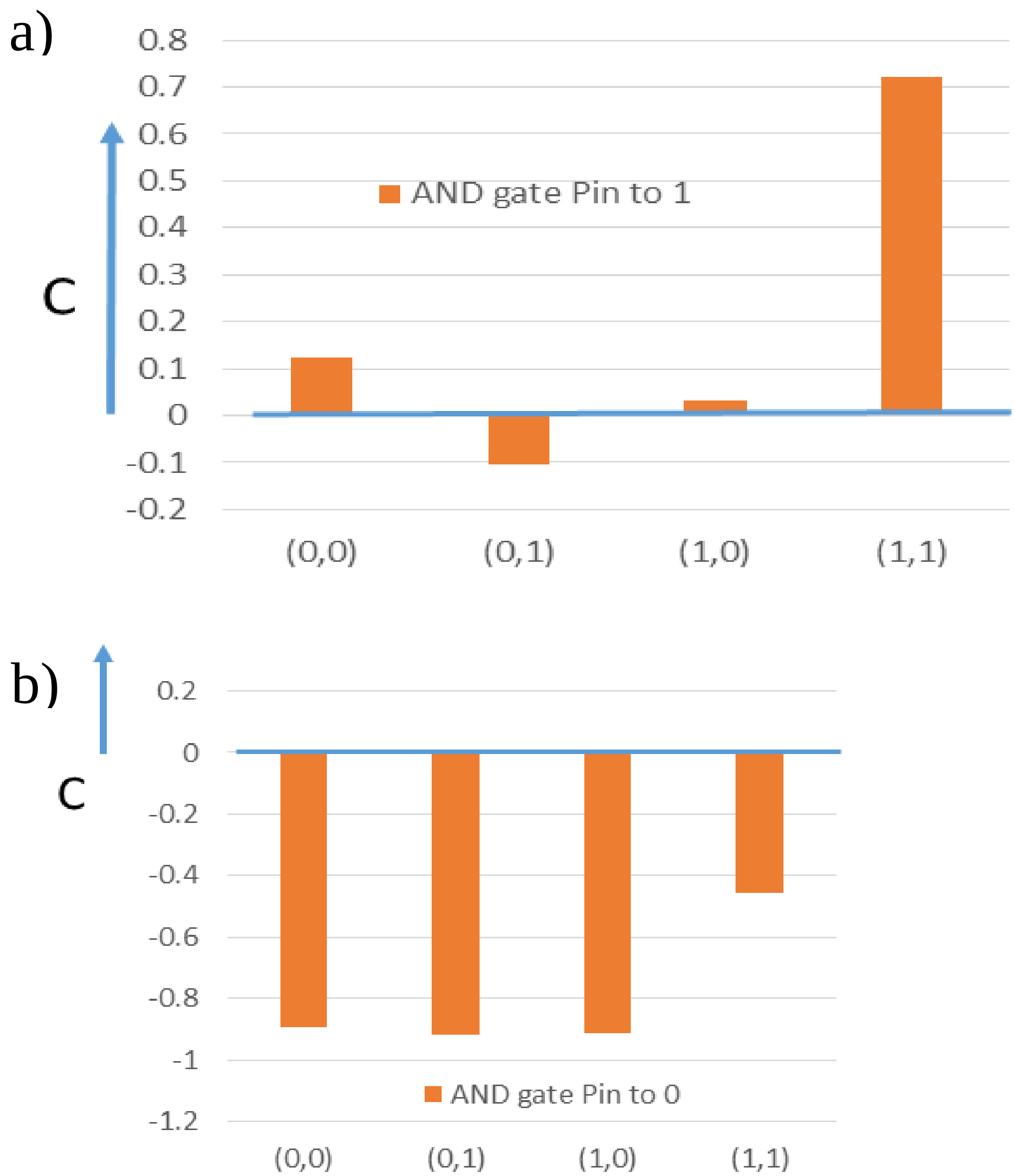

Figure 7-11. Invertibility was demonstrated by pinning the output bit, y, to the 1 state (a) and the 0 state (b). When y is pinned to 1, C(1,1) becomes much larger than the other C values, indicating that $x_1=x_2=y=1$ dominates. When y is pinned to 0, C(0,0), C(0,1), and C(1,0) all become more negative than C(1,1). This indicates that the AND states corresponding to y=0 become much more likely than their pairwise counterparts. C(1,1) also became negative, indicating that P(110)>P(111).

The STT feedback promoted and suppressed circuit states by raising the energy of error states and lowering the energy of proper AND states. Figure 7-12 shows a qualitative diagram of the relative energy levels for the eight possible three-bit system states in the stochastic AND operation. With all three modules set to the midpoint of their control sigmoid, so that their time-average bit value was 0.5, the feedback would have maintained all four AND states at the same low energy level. The 011, 101, and 110 states would have been on the same higher energy level with 001 being the highest energy state. Since the time average of x_2 was greater than 0.5, the x_2=1 states would have lower energy, and the x_2=0 states would have higher energy. With y pinned to 0, all of the y=0 states decreased in energy while the y=1 states increased in energy. The three AND states with y=0 become the desired system states and 111 was suppressed. The feedback raised the energy of the 111 AND state and reduced the energy of the 110 error state so that 110 became more likely than 111, but still less likely than the y=0 AND states. With y pinned to 1, all of the y=1 states decreased in energy so that 111 was the new ground state. The energy of all of the y=0 states increased so that the three y=0 AND states had higher energy than the 011 and 101 error states. However, the 111 state is the desired system state for y pinned to 1, and it is the ground state in this case. The experimental results for the stochastic AND qualitatively agree with the energy diagram in Figure 7-12.

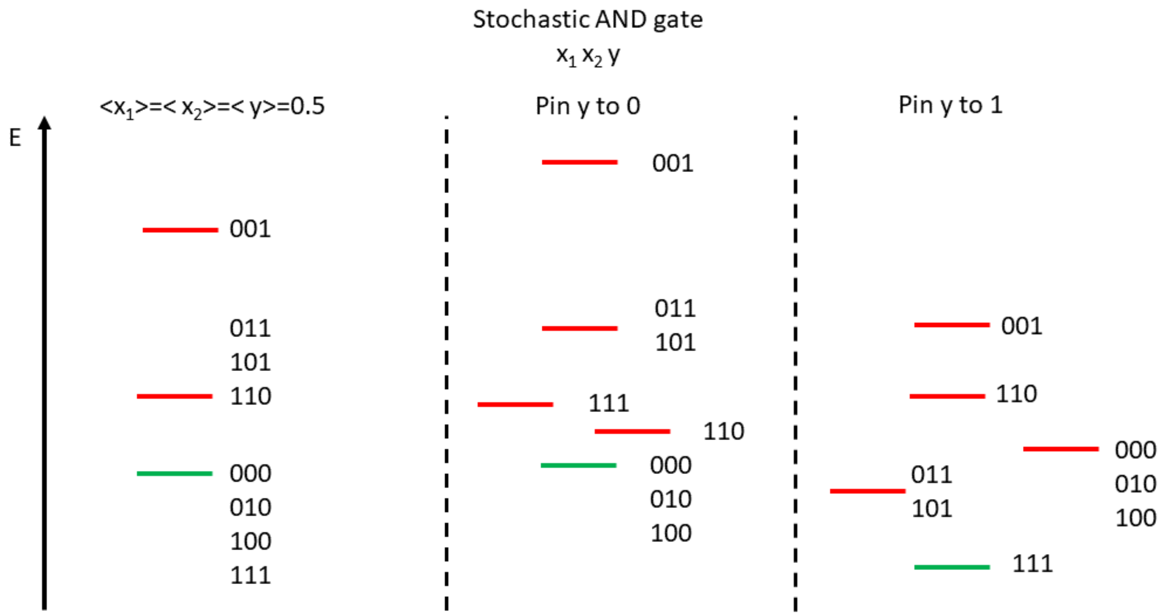

Figure 7-12. The relative energies of the different three-bit states were set by the STT feedback. With all three bits' programming biases set to the midpoint of their control sigmoids (left), the four AND states were on the lowest energy level. With the output bit, y, pinned to 0 (middle), the three AND states with y=0 remained at the same energy. The y=1 AND state was driven to higher energy, above even the 110 error state. With y pinned to 1 (right), the 111 and state decreases in energy to became the new lowest level while the other three AND states maintained the same energy. Pinning y to 1 also lowered the energy of the 011 and 101 error states below the y=0 AND states. This figure was modified from one presented by Hao Chen.

While this work was ongoing, Borders et al. published a result demonstrating an invertible AND gate using STT-controlled, stochastically switching MTJs [39]. In that work, the authors used STT control of stochastically switching MTJs to perform an invertible AND operation similar to the results presented here. In that work, the authors fed output of their MTJ circuits to a microcontroller that used software to calculate the feedback signal that was then sent to the MTJs. The use of the microcontroller introduced a significant lag time between the change of the system's state and the change of input signal. The lag time was not significant for their experiment, however, because the average dwell time of their MTJs was in seconds rather than microseconds.

The authors of [39] also connected their MTJs into an adder circuit that could also be inverted to factor numbers. In the invertible adder, the output was pinned to define the number to be factored, and the input bits stochastically switched between combinations of the prime factors of the pinned output. This was a major achievement in stochastic computing, but much greater speed is necessary before stochastic computing can overtake traditional computing for prime factorization.

7.6 Summary

An invertible stochastic AND gate was successfully demonstrated. The operation was performed using STT controlled low thermal stability MTJs in scalable, modular circuits. The modular circuits were influenced using hardware-based feedback calculated in real time on microsecond or smaller timescales using commercial off the shelf logic chips. An application of the external magnetic field tuning of MTJ dwell times, presented in the next chapter on angle-dependent field switching, was also demonstrated here. This work was the culmination of years of research on mechanisms to control the magnitude of the MTJ energy barrier to switching and to influence the preferred direction of a nanometer scale stochastically switching magnetic moment.

Chapter 8 Angle Dependent Magnetic Field Switching of a Patterned Thin Film Ferromagnet

This chapter presents a more rigorous treatment of an effect I discovered while working on the stochastic AND gate. I found that I could use a hard axis magnetic field to manipulate the thermal reversal rate of the MTJs. After completing that experiment, I then went back and performed angle-resolved magnetic field switches on one of the MTJs to find trends in the switching field of the device as a function of angle. I found an unexpected cubic component of the magnetic anisotropy where I expected a purely uniaxial anisotropy. I also found that the device reversed its magnetization through two jumps rather than one near the hard axis. This work is in preparation for publication.

8.1 Background

Stoner and Wohlfarth famously studied the angle dependent response of the magnetic moment in thermally stable ellipsoidal magnetic nanoparticles [134]. They considered a particle with uniaxial anisotropy in a purely rotational magnetization reversal regime. Their theory led to the Stoner-Wohlfarth astroid, shown in Figure 8-1, that appears in magnetism texts. The Stoner-Wohlfarth theory was extended to more complex cases, such as combinations of cubic and uniaxial anisotropy and multi-jump magnetization reversal [135], and the more complex dynamics were studied experimentally in nanoparticles and thin film magnets [136,137]. Spin currents have also been used to bias thin film magnets in one direction during the angle-dependent magnetic field reversal experiment [138].

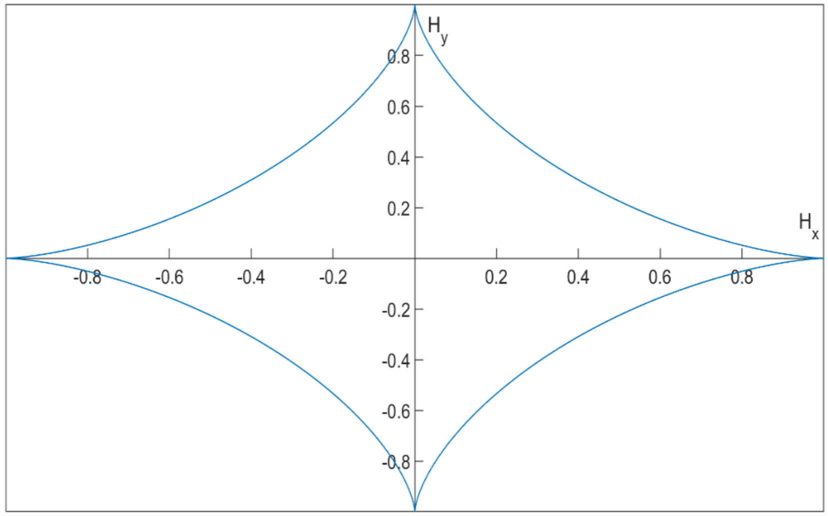

Figure 8-1. The classic Stoner-Wohlfarth astroid describes the purely rotational magnetization reversal in a uniaxial magnetic nanoparticle. The deterministic switching field is shown in blue in units of the anisotropy field, H_k. In this case, a field applied at 45° to any axis would result in the lowest observed switching field.

The thermal stability of nanomagnets has been studied in the field of magnetic random-access memory (MRAM) [59] [139] with the goal of finding a way off the horns of the MRAM trilemma: the balancing of longevity, data retention, and write error rate [36]. In particular, the continuing trend toward smaller and smaller magnetic tunnel junctions (MTJs) has fueled a desire for new means to increase thermal stability [66,140]. This would seem to conflict with the field of stochastic and neuromorphic computing.

The rise of stochastic and neuromorphic computing has led to research interest in decreasing thermal stability in a controlled way in order to improve the speed and efficiency of stochastic logic elements [18,29,42,141]. Stochastic computing operations have recently been demonstrated using spintronic devices [39]. The concept of these devices is to influence magnetic telegraph noise, the square pulse electronic signature of stochastic magnetization reversal, using an external control mechanism such as external magnetic field, spin transfer torque (STT), or spin orbit torque (SOT). The goal is to perform a classical analog to quantum computing's adiabatic optimization [40] with the statistics of many of these classical operations, performed in series or parallel, standing in for the inherent probabilistic nature of quantum mechanics. To that end, the stochastic computing elements must be fast and/or energy efficient to compete with a quantum computer. That is to say that the energy barrier to switching the stochastic element must be minimized as much as possible while maintaining a well-resolved two-state system.

Hard axis fields have been used to break the symmetry of perpendicularly magnetized MTJs in spin orbit torque (SOT) switching experiments [32,50,142]. They have also been used as a source of randomness. A hard axis field can be applied to an MTJ so that the free layer magnetization aligns to the applied field. The field is then removed, and the magnetization realigns parallel or antiparallel with equal probability [65].

Industry has demonstrated proficiency in producing MRAM with 10-year data retention, longevity of 10^{10} write cycles, and write error rates less than 10^{-6} [37]. MRAM is becoming a mainstream technology as the utility of stochastic computing is just being realized. A means of temporarily turning stable MRAM devices into stochastic logic elements for specific applications, such as producing random numbers or factoring large numbers in a cryptographic application, could constitute a disruptive technology in the field of stochastic computing. Here we present a simple, reversible means of destabilizing

MTJs to produce magnetic telegraph noise with retention times on the sub-millisecond time scale.

8.2 Nanofabrication

Films consisting of SiOx/Ta (5)/CoFeB (2.5)/MgO (1)/CoFeB (2.5)/Ru (0.85)/CoFe (2.5)/IrMn (8)/Ru (10), where the numbers in parentheses indicate the film thickness in nanometers, were deposited at KAUST. The magnetic layers were magnetized in-plane, with the IrMn pinning the CoFe layer. The CoFe and top CoFeB layer formed a synthetic antiferromagnet, thus fixing the reference layer. Another 10 nm of Ru was deposited at CMU prior to patterning to increase the MTJ pillar height and thus help prevent exposing the bottom lead during the later top via back etch process. A bilayer hard mask consisting of 70 nm of carbon and 10 nm of SiN_x was then deposited. The carbon layer in this hard mask helped later in the process when oxygen plasma was used to selectively etch the carbon and not affect the passivating SiN_x. The top SiN_x was chosen for its properties as an electron beam lithography substrate. The film was patterned into 60 nm by 90 nm ellipses by electron beam lithography to form trenches in the PMMA resist, with the long axis of the ellipse parallel to the pinning direction of the IrMn layer. Cr was then deposited onto the sample and lifted off by sonicating at 140 kHz in acetone. This left Cr ellipses on top of the bilayer hard mask to act as a mask for the reactive ion etch (RIE), using first CF_4/CHF_3 then O_2/Ar to transfer the ellipse pattern into the C/SiN_x. The C/SiN_x then acted as a mask for Ar ion milling to transfer the ellipse pattern into the MTJ film, with the etch stopping when the mass spectrometer attached to the ion mill showed the top of the final Ta layer was reached. The MTJ pillars were then passivated with 200 nm of SiN_x. Next, the cross-shaped bottom leads were defined by photolithography, and the remaining Ta was etched away. A via, a conductive pathway to the metal layer buried under insulator, to the top of the MTJ was defined by photolithography and etched by CF_4/CHF_3 RIE until the carbon cap was exposed. The carbon was then etched by O_2/Ar so that the bottom part of the via was the same size as the MTJ. This helped prevent shorting by a parallel connection. Vias to the bottom lead were then defined by photolithography and etched by CF_4/CHF_3 RIE. The final lead pattern was then defined using photolithography and the sample was loaded for sputter deposition. Just before deposition, the sample was exposed a sputter etch plasma to remove any native oxide that would reduce the quality of the electrical connections. Without breaking vacuum, the platinum leads were deposited on top of a tantalum adhesion layer. After liftoff, the sample was diced into dies of 25 MTJs. The dies were mounted in chip carriers and wire bonded to macroscopic leads.

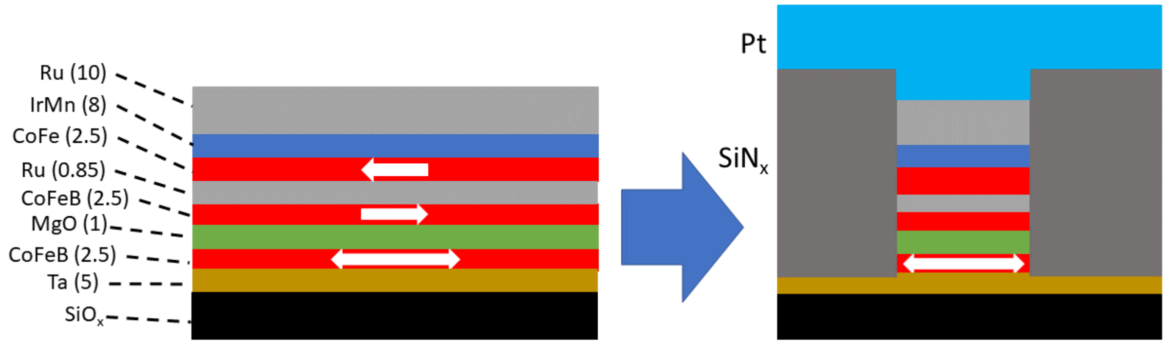

Figure 8-2. The MTJ film was grown at KAUST and patterned into hardwired MTJs at CMU. The MTJ film was fully etched to the bottom Ta leads and passivated with silicon nitride before being connected by Pt leads.

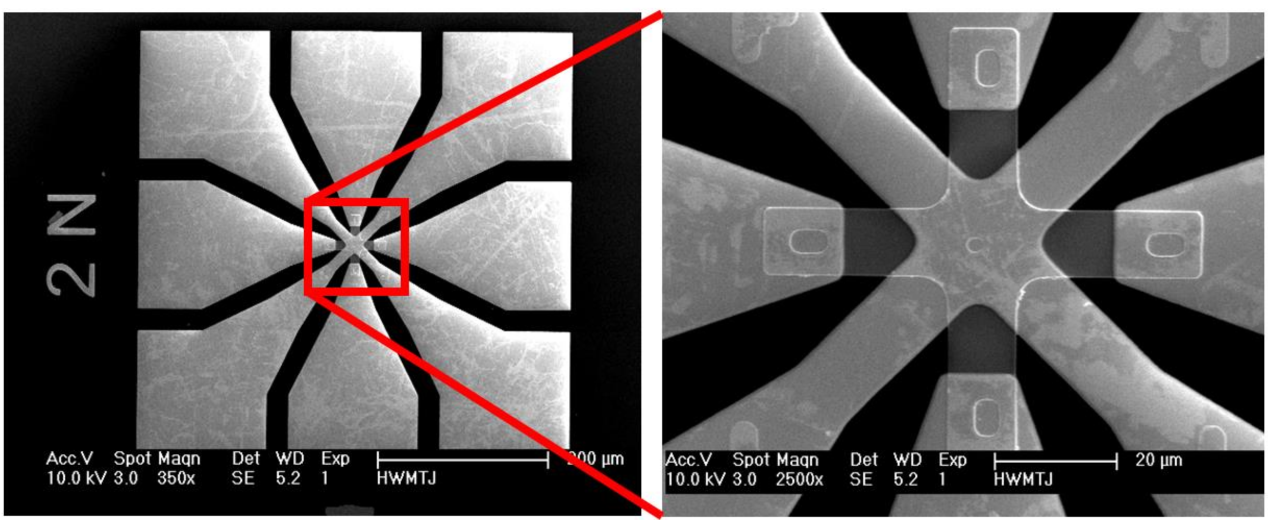

Figure 8-3. The patterning process for these MTJs includes an electron beam lithography layer and five photolithography layers. The vias are visible in the SEM image on the right. The dark cross shape is the bottom Ta lead. The lighter gray areas are the Pt leads. The ellipses near the ends of the cross are the vias to the bottom Ta lead, and the round hole in the center is the via to the top of the MTJ pillar.

8.3 Electronic Measurements of Hardwired Devices

The sample and its chip carrier were mounted in a machined acrylic holder which was mounted to a rotating base. The base had angle graduations and a Vernier scale for more accurate angle measurement. That apparatus was placed between the two pole-pieces of an in-plane electromagnet with a field range of up to 500 Oe. The electromagnet was driven by a computer-controlled power supply while the current passing through the MTJ was read by the same computer. Magnetization loops were recorded every 5 degrees of field angle through most of the circle and every 1 degree near the hard axis. Figure 1 shows a schematic of the MTJ with its easy axis, applied field, and magnetic moment. The relevant angles are labelled for reference later.

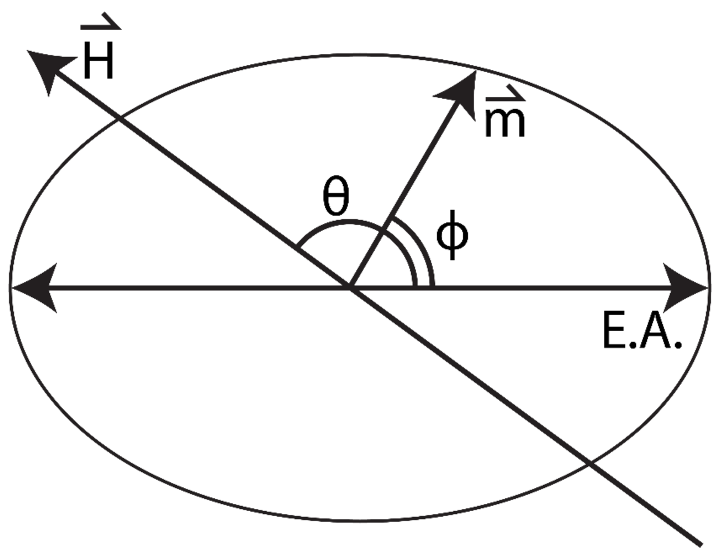

Figure 8-4. This schematic shows the easy axis (E.A.) and the directions that will be discussed in this paper. The angle θ represents the angle between the easy axis in the positive x direction and the applied field. The angle φ represents the angle between the easy axis in the positive x direction and the MTJ free layer's magnetic moment.

Figure 8-5 shows the easy axis magnetization loop taken at an angle, θ, of 0 degrees. As with all the magnetization loops shown, the measurement begins at the maximum positive field shown, 500 Oe in this case. As the field decreases at a rate of 250 Oe/s, the resistance is single valued, within the root mean square (RMS) electronic noise of 0.18 Ω, until it reaches -41±0.5 Oe. At that point, the resistance increases sharply to another resistance level that remains constant while the field continues to decrease to the minimum field of -500 Oe. The field sweep rate then reverses, and the resistance switches back to the previous, low-resistance value as the field reaches 41±0.5 Oe. The easy axis coercivity is 41±0.5 Oe with deterministic switching; there is no thermal reversal near the switching fields nor in the hysteretic region. The angle between the magnetization direction and the easy axis is calculated from the measured electrical resistance using the formula $\phi = \cos^{-1}\left(\frac{\bar{R}-R}{\Delta R/2}\right)$, where $\bar{R}$ is the average of the parallel and antiparallel resistances, R is the measured resistance, and ΔR is the difference between the antiparallel and parallel resistances. In Figure 8-5, ϕ switches between 0° and 180°.

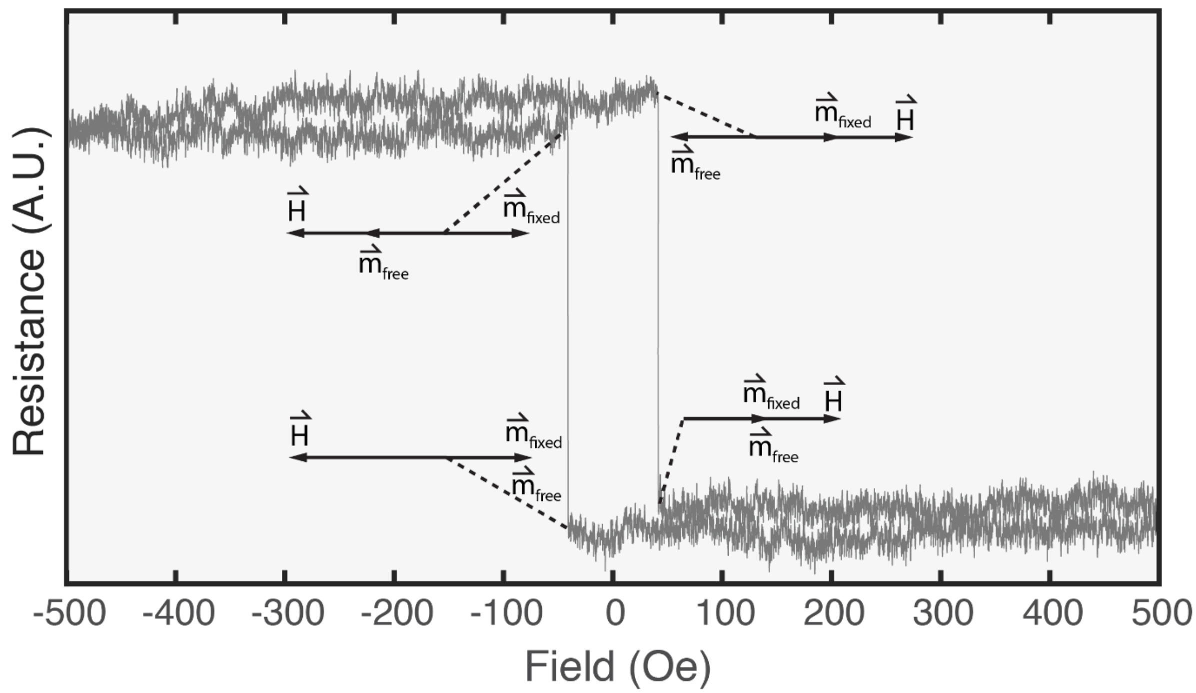

Figure 8-5. The easy axis loop is the familiar loop we see with a uniaxial MTJ. The major axis loop has the lowest coercivity at 41 Oe, and always switches between parallel and antiparallel.

When the field is applied along the perpendicular direction, as shown in Figure 8-6, the resistance shifts continuously toward higher resistance as the applied field decreases before suddenly jumping the final approximately 20% to the high resistance level at 110±18 Oe, the angle ϕ jumping from about 120° to 180°. Continuing in the negative direction, the resistance conducts the same 20% switch in reverse at -153±2 Oe. The resistance then gradually decreases until the negative field reaches -388±4 Oe where it jumps down about 15% of the total resistance difference, from ϕ=60° to ϕ=40°, and maintains that level until the minimum field of -500 Oe is reached. On the increasing branch of the loop, the resistance relaxes to the minimum level and remains there across zero applied field. The resistance then begins increasing as the applied field becomes more positive until completing another ~15% switch at 381±4 Oe, from ϕ=40° to ϕ=60°. Thermal reversal was observed around the 110 Oe switch in 10 out of the 20 magnetization loops collected at this angle.

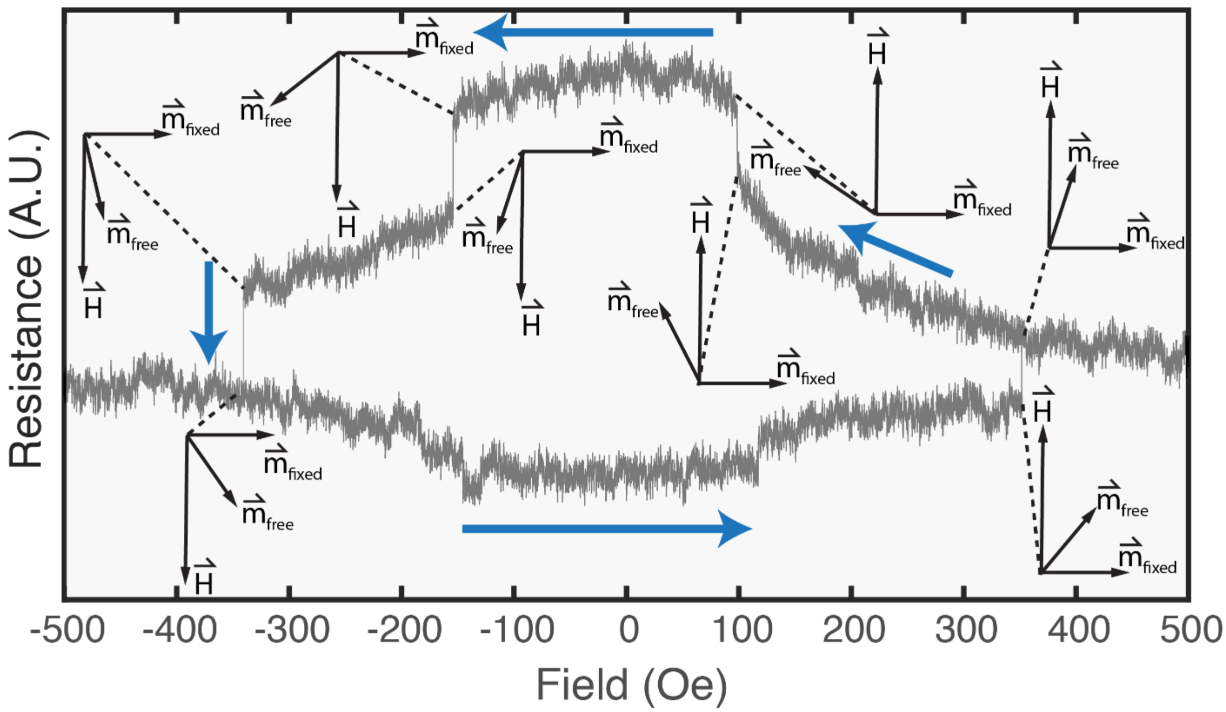

Figure 8-6. The hard axis loop shows a slow alignment of the magnetization with the applied field until a switch of less than half the total magnetization. Here the free layer magnetization is only parallel or antiparallel around zero field.

When the field angle is increased two more degrees (Figure 8-7), the decreasing branch then follows the low resistance path. The resistance decreases gradually to the low resistance level before beginning to increase again around -200 Oe. At -358±5 Oe, the resistance sharply increases by about 15%, much like the drop at -388 Oe in the previous magnetization loop and stays at that level to the end of the decreasing branch. As the field increases from the most negative value, the resistance then gradually increases to the maximum level. At 176±6 Oe, the resistance drops by 37%, from ϕ=135° to ϕ=90°, with thermal reversal in every observed case. The resistance then gradually decreases until another small downward switch of 19% at 357±8 Oe. The fact that the path followed by the decreasing and increasing branches of the magnetization loop reverses between Figure 8-6 and Figure 8-7 indicates the magnetic hard axis is somewhere within this two-degree range.

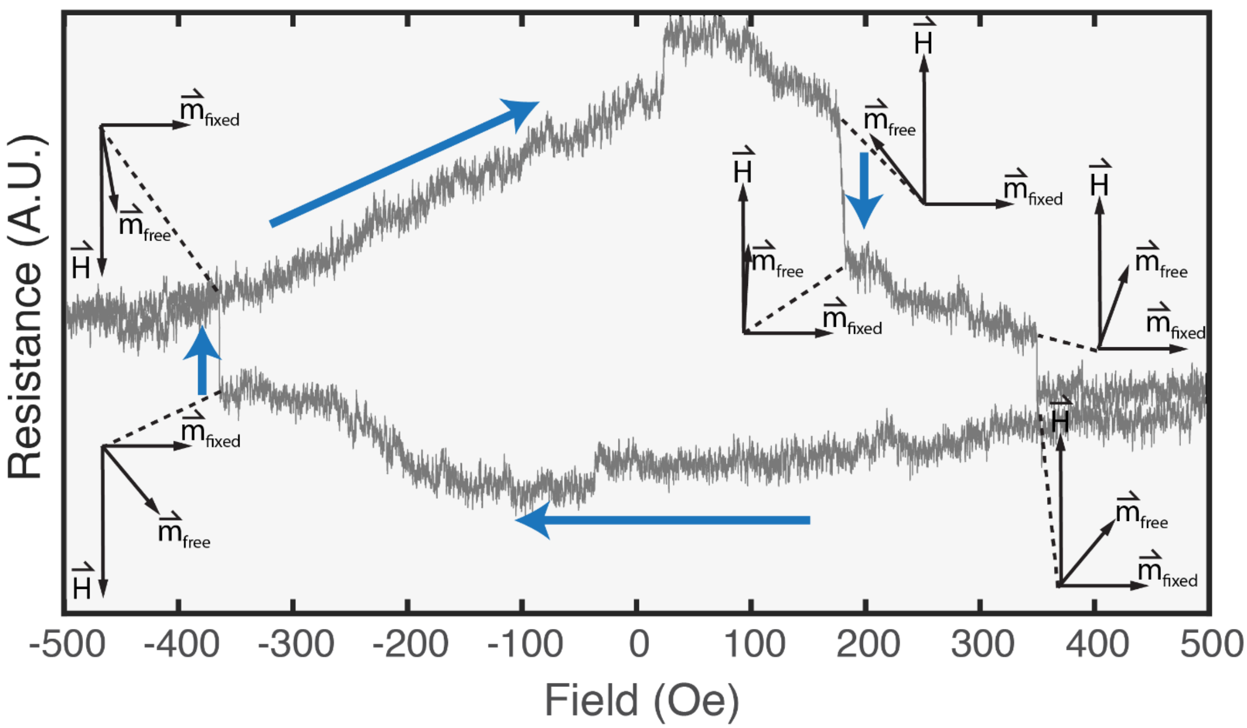

Figure 8-7. The resistance levels at the magnetic field extremes have reversed compared to Figure 3. This indicates that the applied field has passed the minor axis of the ellipse.

The loop measured at an angle between those for Figure 8-6 and Figure 8-7, shown in Figure 8-8, begins with the decreasing field branch in the low resistance level. The resistance is relatively constant until the field reaches about -27 Oe, where the resistance begins to slowly increase to the saturation level. As the field begins increasing, it traces the same path, within error, until reaching -27±18 Oe, where it sharply and deterministically increases across 88% of the resistance range. The resistance then relaxes to the high resistance level at zero field. The resistance decreases as the field becomes positive until dropping 41% of the range at 166±5 Oe, from ϕ=100° to ϕ=145°. Here again, thermal magnetization reversal is observed in every case of this switch. The resistance then gradually decreases until the measurement ends at the maximum field. While the resistance jump between the level at the end of the measurement and the beginning of the measurement is never observed, every one of the 20 magnetization loops measured begins in the low resistance level and ends at an intermediate resistance. The intermediate resistance level at 166 Oe in Figure 8-8 corresponds to an angle between the magnetization and the free layer easy axis of 85°, indicating that the magnetization is switching between roughly antiparallel to the fixed layer and roughly aligned to the external field.

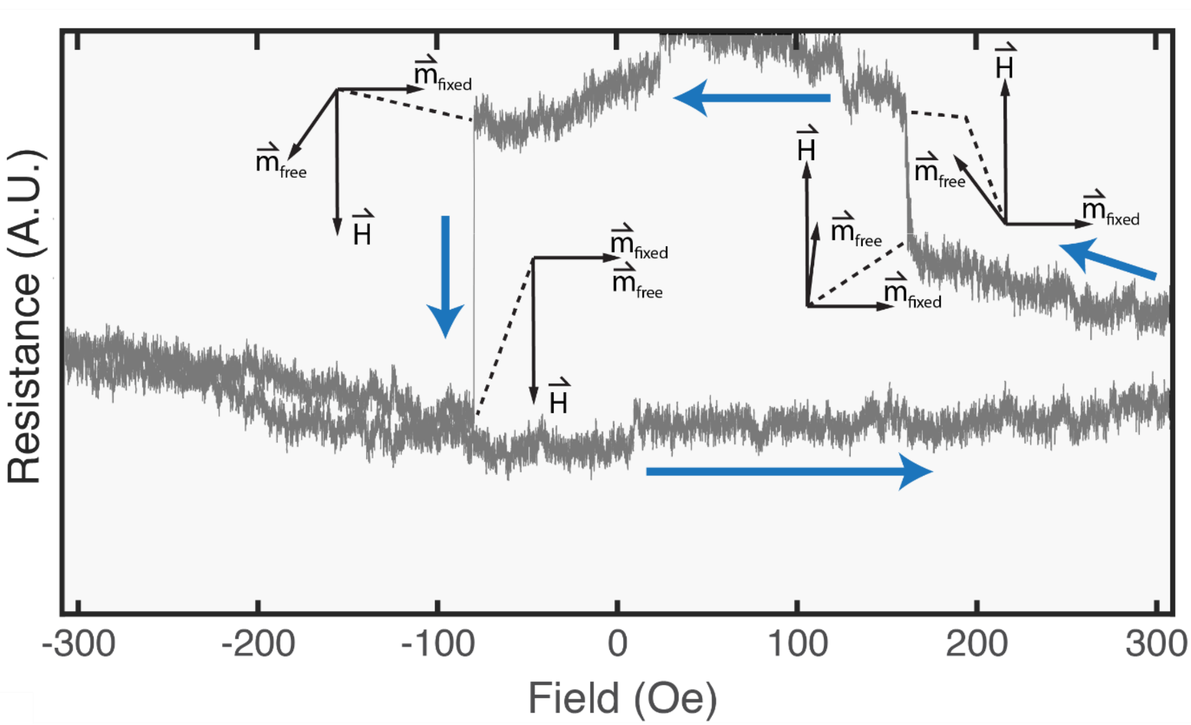

Figure 8-8. With the field applied along the direction halfway between the previous two figures, the magnetization rapidly switches between antiparallel and an intermediate resistance when positive field is applied.

8.4 A More Complex "Astroid"

After averaging the switching fields for each jump in magnetization observed in the magnetization loops, the aggregate results were used to create an astroid. Figure 8-9 shows the decomposition of the average magnetic switching field into Cartesian components. Here H_x is along the major axis of the ellipse, the expected magnetic easy axis of the device. Within 15° of the MTJ ellipse's minor axis, the magnetization switches via two-jumps rather than the one-jump switching at angles closer to the major axis. The top plot shows the single jump and the higher field two-jump switches, red, and the lower field two-jump switches, blue, together to get a sense of the difference between them.

The middle plot in Figure 8-9 shows the single jump switches as well as the higher-field switches for the two-jump case. The switching field slowly decreases as the applied field is rotated away from the easy axis with a local minimum at 30°. The switching field then increases to a local maximum at 35°, co-located with a local maximum in switching field variability. The overall magnitude of the switching field tends to increase as the angle increases through the first quadrant until dropping somewhat after the applied field angle passes the minor axis of the MTJ ellipse. The switching field remains lower throughout most of the second quadrant while the uncertainty in the switching field remains higher than in the first quadrant. As the applied field angle approaches the ellipse's major axis, the switching field once again increases to a local maximum, here at 140°. This local maximum is again collocated with a local maximum in the switching field variability. The switching field then decreases again until reaching 210°, the antipode of the first quadrant minimum. The third quadrant is basically symmetric with the first quadrant, including the highly variable local maximum opposite the one observed in the first quadrant and the sudden drop in switching field as the angle approaches the ellipse's minor axis. The fourth quadrant shares less symmetry with the second than the third does with the first, though they share increased switching field uncertainty. There is again a local maximum in switching field as the applied field approaches the major axis antipodal to the local maximum observed in the second quadrant. This fourth quadrant maximum is broader than the other three, though all the points in this local maximum exhibit large uncertainty. The switching field then decreases once again, maintaining continuity with the first quadrant measurements. Unlike the uniaxial case, this astroid shows significant local minima near the H_x axis, and the concavity of the curve in each quadrant is opposite of the classic case. There is also an asymmetry along the H_y axis. The local minima in the switching field near the x-axis with the switching field increasing as the angle moves away from the axis suggests the four-lobe shape of a cubic anisotropy, which will be discussed later. The concavity of the curve may be the result of a combination of uniaxial and cubic components in the magnetic anisotropy. The asymmetry in switching field between the positive and negative y-axis is similar to observations made with the nanomagnet under the influence of a spin current [8]. While the current density passing through the MTJ in this measurement is approaching that required for STT switching, this switching field asymmetry is perpendicular to the polarization direction of the spin polarized current. A spin polarized current would shift the switching field along the polarization direction. Instead, this is more likely an exchange bias effect caused by the non-collinear spins in the pinning IrMn layer.

The bottom plot in Figure 8-9 shows the one-jump switches as well as the lower-field two-jump switches. The local minima and maxima near the major axis remain the same as in the other plots of Figure 8-9. Almost all the new points from the low-field two-jump switches have larger variance than the higher-field switches. The black dots on the points near the positive y-axis indicate conditions under which magnetic telegraph noise was observed. There is an asymmetry along the minor axis, with the switching field much lower along the negative y-axis than the positive y-axis. Likewise, telegraphing was observed only near the positive y-axis, not for the symmetric points in the opposite direction. The sharp decreases in switching field around 80° and 100° highlight the cubic contribution to the anisotropy as the field angle gets closer to the major axis. The four lobes of the cubic anisotropy are much clearer in this low-field switch picture than in the high-field case.

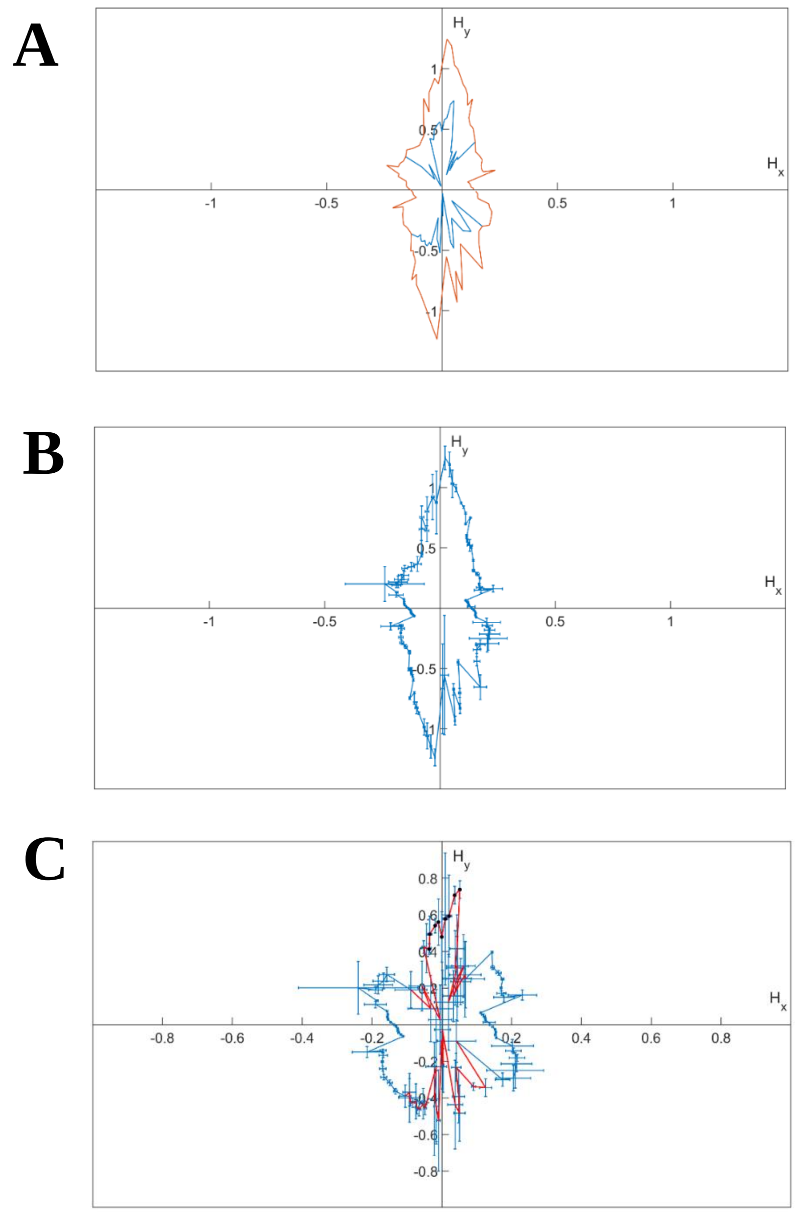

Figure 8-9. The switching fields are decomposed into their Cartesian components. H_x lies along the θ=0 direction, and H_y lies along the θ=90 direction. A) The higher field switches are shown in red, and the lower field switches are shown in blue for the cases where there are two-jump magnetization reversals. Error bars are omitted for clarity. B) The single jump switches and the higher field two-jump switches are shown with error bars. C) The single jump switches and the lower field two-jump switches are shown with error bars. The red line indicates the two-jump reversal case. The points with black dots show the conditions under which telegraph noise is observed.

Like Figure 8-9 showed the effect of the applied field angle on the switching field, Figure 8-10 shows the effect of the angle between the applied field and the major axis (θ) on the angle between the intermediate metastable magnetization direction in the two-jump case and the major axis (φ). φ peaks when the magnetic field is applied near the MTJ's minor axis, reaching over 90 degrees. The intermediate magnetization direction in the case of a two-jump reversal seems to be a combination of the free layer demagnetizing field and the external applied field. The position of the intermediate states tends to be consistent in the first and third quadrants, which much more variability in the second and fourth quadrants. However, the positions of the intermediate states when they first appear at 75° and 255° and when they finally disappear at 125° and 315° are remarkably consistent.

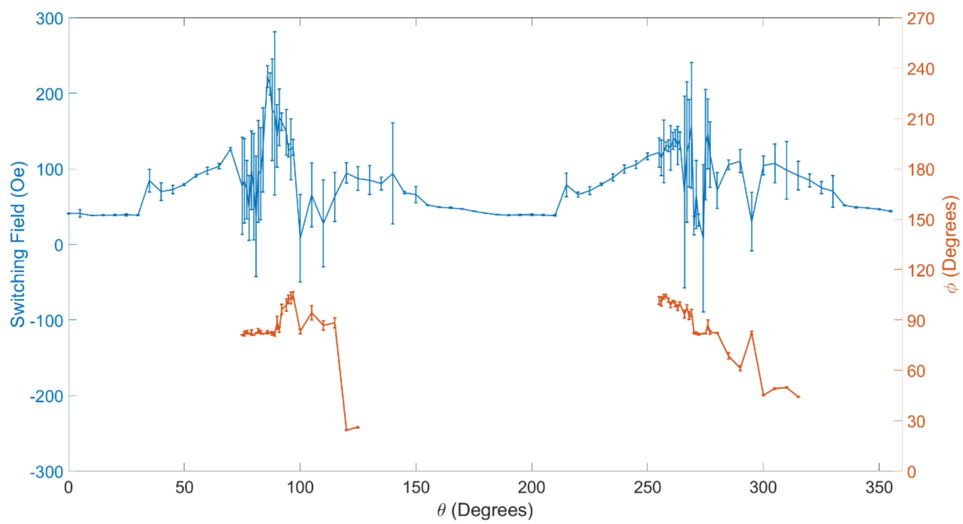

Figure 8-10. The switching field from Figure 8-9B is shown here in blue. The angle (ϕ, shown in red) between the intermediate metastable magnetization direction, when the magnetization reversal occurs through two jumps, and the major axis varies with the applied field direction, peaking around the minor axis of the MTJ ellipse.

A magnetic field was applied along the hard axis and the magnetic telegraph noise was measured in the time domain. Figure 8-11A shows the result of those measurements. Using a constant 183 Oe hard axis field and 480 mV bias, applied so that electron current flows from the fixed layer to the free layer, the device has gone from a stable, deterministic MTJ to a stochastic device with an average dwell time of 588 μs. Figure 8-11B shows a proposed energy schematic for the system when the external field is applied along the hard axis. This model assumes a combination of cubic and uniaxial magnetic anisotropy to account for the two-jump switches such as those shown in Figure 8-6, Figure 8-7, and Figure 8-8. This assumption is also supported by some computational work on IrMn, the antiferromagnetic pinning layer in our film stack, which found that the noncollinear spins in IrMn contribute a cubic-like component to the anisotropy [143]. While cobalt ferrite also has a cubic anisotropy, the same kind of training procedure used in oxide exchange bias experiments [20] was attempted, but no indication of oxide was found. That assumption of cubic anisotropy results in an energy picture with two minima near each other, with the energy proportional to $(\sin\phi\cos\phi)^2$ along with the uniaxial minimum, which shifts to 15° from 0° due to the cubic anisotropy. The energy barrier between the two metastable states in the conditions shown in Figure 8-11A was experimentally determined to be 13.3 k_BT. Using an anisotropy energy density of 3.58×10^5 erg/cm^3 and a saturation magnetization of 597 emu/cm^3 [70], this uniaxial and cubic anisotropy model yields an energy barrier approximately equal to the experimentally determined barrier, 13 k_BT calculated vs 13.3 k_BT measured, between the two states at at φ=104° and φ=180° and a larger barrier between $\varphi=104°$ and $\varphi=0°$. The anisotropy energy density used in this model is about seventeen times lower than experiments have found for IrMn at room temperature, 6.2×10^{6} erg/cm^{3} [144] and about three times greater than the anisotropy expected from shape anisotropy in the CoFeB layer, 1.17×10^{5} erg/cm^{3}. The cubic anisotropy contribution in this model being larger than the shape anisotropy of the CoFeB indicates that this cubic term is not simply a higher-order contribution from the elliptically patterned CoFeB. Given that the electronic signal measured here arises from the alignment of the two CoFeB layers adjacent to the MgO tunnel barrier, it is reasonable that the dynamics are dominated by the CoFeB anisotropy, albeit modified by the IrMn.

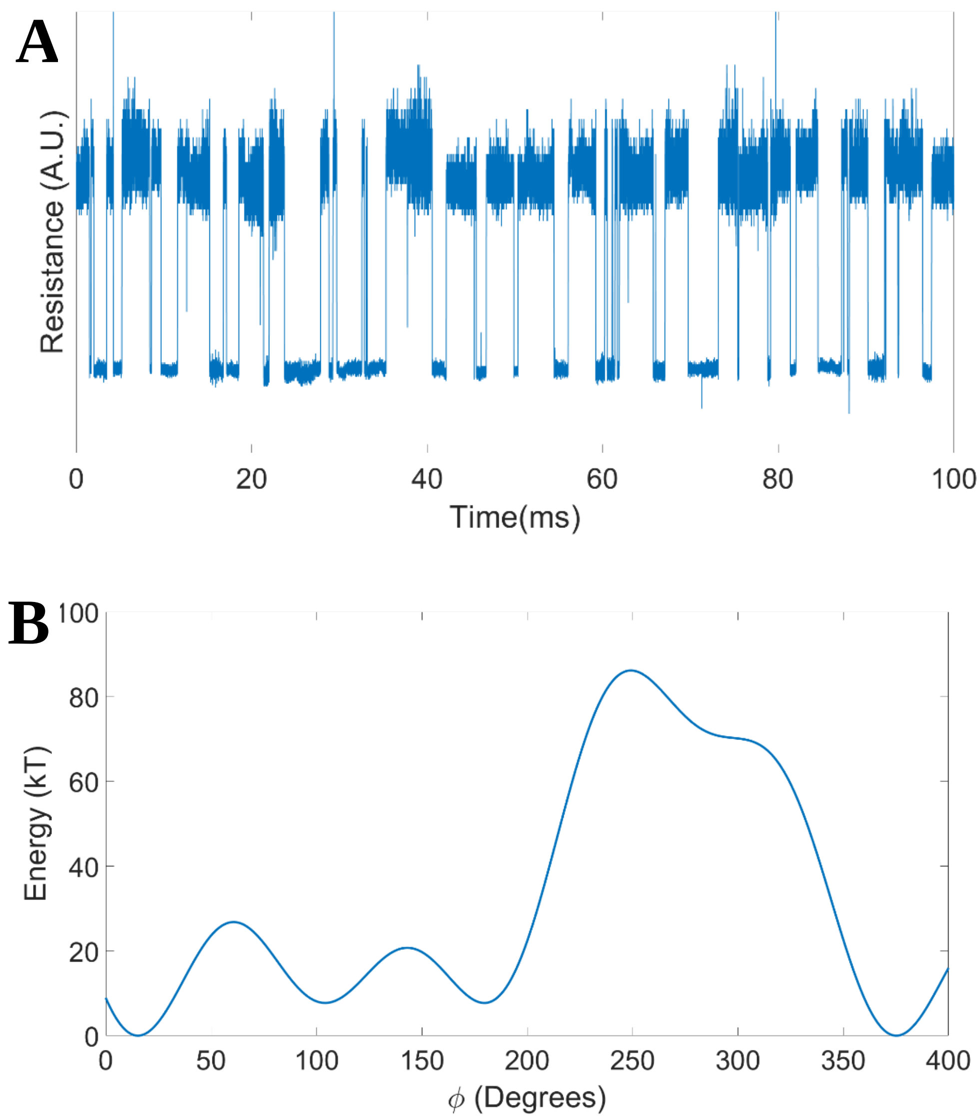

Figure 8-11. A) The resistance across the MTJ varies in time as the magnetization stochastically switches between the two metastable states identified in the minor axis magnetization loop. The transport data was collected at 480mV bias with 183 Oe hard axis field. B) The cubic anisotropy results in two metastable states close together in angle with a small energy barrier in between.

Previous theoretical work suggests this cubic behavior is caused by the IrMn antiferromagnetic pinning layer [143]. The same IrMn layer may also cause the difference in switching fields between positive and negative H_y fields in Figure 8-9. The uncompensated spins at the interface of IrMn and CoFe may have added to the local field and resulted in the loop shifts observed in magnetization loops near the minor axis of the ellipse. The exchange bias effect is only observed in one direction because the maximum field applied in the experiment is much smaller than that needed to reverse the IrMn.

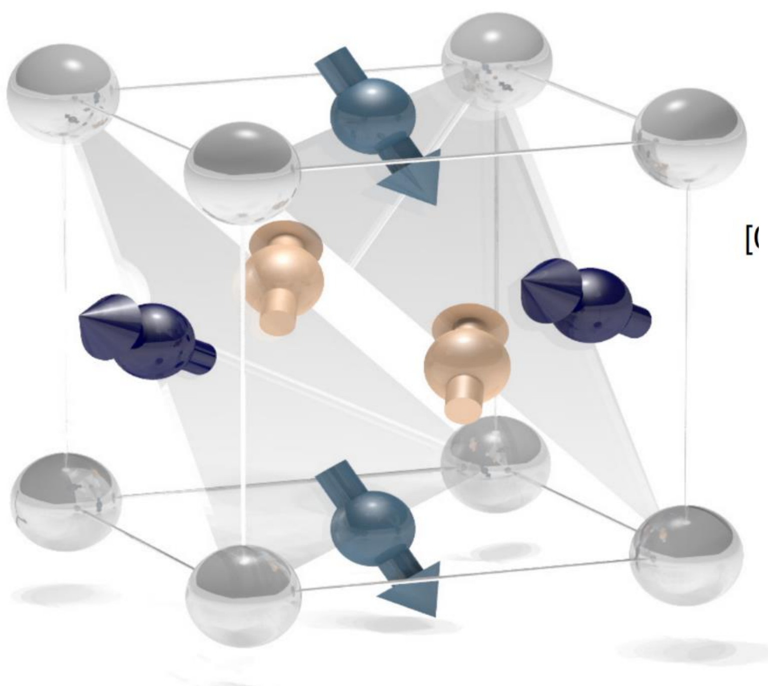

Figure 8-12. The ground state of $L1_2$-IrMn features non-colinear spins. The uncompensated spins at the interface of IrMn and CoFe could result in an exchange bias. Figure taken from [143]**.**

8.5 Summary

We have shown the energy barrier to switching of stable MTJs can be decreased to the point of spontaneous thermal reversal on timescales as short as 588 μs using a constant magnetic field. Our MTJ system exhibits cubic-like anisotropy both by the fact of the two-jump reversal for a range of angles near the ellipse's minor axis as well as the local maxima of switching field near the major axis. There also appears to be an exchange bias effect along the minor axis of the MTJ ellipse.

As the angle of the applied field approached the major axis again after recording the magnetic telegraph noise along the minor axis, the switching behavior of the device once again became deterministic. This shows that the destabilizing effect of the minor axis field is reversible. MRAM devices could use a minor axis magnetic field to destabilize the free layer magnetization and then influence the magnetization direction by STT to create an ad-hoc stochastic computing device.

APPENDIX A Process Flow for Hardwired MTJ Devices

This appendix describes the process flow for making hardwired MTJ devices. They are passivated with SiN_x and electrical connection is made to either Pt or Au leads connecting to the top and bottom of the devices.

The process described here was adapted by Samuel Oberdick from a process originally developed by Matt Moneck and modified by Masaki Furuta. Stephan Piotrowski helped print the masks used for photolithography. I have further adapted the process to enable fabrication of a wider range of devices and accommodate different materials.

The process flow described below can use either 4 or 5 photomasks. A separate step using electron beam lithography is used to define the devices with HSQ or PMMA with an extra deposition step.

The etch times and thickness of hard mask layers used in the process flow will vary depending on the particular thicknesses in the MTJ stack. You should calculate your own deposition and etch times based on rate runs and modify this process to fit your film stack. The etch rates for ion milling given in Appendix A of Samuel Oberdick's thesis are useful in determining etch times and hard layer thickness for a specific stack. Etch rates can vary between tools, targets, and reactant gases. Some rates are given here, but you should use the most recent available rate from rate run tests.

I recommend carefully inspecting the sample with an optical microscope between steps to ensure everything is going well. Do not remove the sample from the clean room until the full process is completed.

Process Flow

Step 1. Preparing MTJ stack for electrical contact and hard mask with additional sputtered layers.

- Typical MTJ stacks have structures similar to Si||Ta/Ru/Ta/CoFeB/MgO/CoFeB/Ta/Ru.
- A 10-30 nm Pt or Ru layer may be deposited on the MTJ stack first. This layer is helpful for making electrical connection to the top of the MTJ devices through backetched vias at the end of the process flow. The thickness of this layer can be adjusted based on the exact MTJ stack, but a relatively thick conducting layer is almost necessary for making good electrical contact when backfilling vias in Step 8. I usually use Ru when it is available in the #4 and deposit at the same time as the hard mask.
- A Cr/C/SiN_x layer is sputtered next as a hard mask for defining the MTJ devices after e-beam lithography. An adhesion layer is necessary to stick C to Pt.
- At least 52.5 nm of C is sputtered using 5T #4, DC 150 W, 5 mTorr Ar. Deposition rate is 2.16 nm/min. Too much hard mask can deform the shape of the final devices. 72.5 nm of C has been effective for patterning 60 x 90 nm ellipses.
- 7.5 nm of SiN_x is sputtered using 5T #4, RF 300 W, 3.5 mTorr Ar + 1.5 mTorr N_2. Deposition rate is 3.9 nm/min.

Step 2. Photolithography to define alignment marks for electron beam lithography (L1 mask). This step is needed if you plan to do the electron beam write in the SEM. This is not necessary for writing with the Elionix e-beam writer!

- Spin on HDMS resist, pre-spin at 600 RPM for 6 seconds, spin at 4000 RPM for 45 seconds.

- Spin on AZ4110 resist, pre-spin at 600 RPM for 6 seconds, spin at 4000 RPM for 45 seconds.
- Pre-bake resist at 95°C for 4 minutes.
- Expose using MA6 contact aligner for 175 seconds.
- Develop in 4:1 H_2O:AZ Developer for 1.6 minutes.
- (Optional but recommended) Descum the sample in the PT790 using Mr. Pink recipe.
- Sputter Ta to define e-beam alignments marks. Tantalum can be sputtered with the 5T#5.
- After deposition, lift-off step reveals the alignment marks on the substrate. 8 minutes of sonication in acetone at 140 kHz and 100% power is sufficient to lift off AZ resist.

Step 3a. Electron beam lithography to define pillars using HSQ resist

- Spin on HSQ resist (XR-1541 from Dow Corning, 2% by volume in MIBK) , pre-spin at 600 RPM for 6 seconds, spin at 3500 RPM for 60 seconds.
- Pre-bake at 190°C for 2 minutes.
- Make scratches at each corner of substrate (focus for Direct Stage Control later) and load into Sirion 400 or 600. This is only necessary for writing in the SEM. The Elionix has its own laser for measuring working distance and calculating plane correction.
- Follow usual e-beam lithography procedure. Different batches of HSQ will take different electron doses to write. 7500 $\mu C/cm^2$ is a good dose with which to start testing. Be sure to test before investing in this write.
    - For writing in the Sirion SEM systems:
        - The write is done at 30 kV, spot 1 and a working distance of 5.5 mm in the Sirion systems. For optimal alignment click on "stage setup" and ensure the backlash correction is turned off.
        - To start the write, find the alignment marker labeled "1L" in the array of devices that will eventually become the first die. Process the appropriate run file after focusing on the "1L" alignment marks at a mag of 1650x.
        - The whole process is automated from this point. The write can take 3-5 hours and will likely require you to manually realign the SEM to the alignment marks several times.

  - In the Elionix, use 100 kV and 1 nA beam current to write well-separated pillars with dimensions greater than 30 nm. You may need to use lower beam currents for smaller or denser features. The entire write takes about 40 minutes using 1 nA for all features. You may choose to use higher beam current for the photo alignment marks to speed up the process.
- After lithography is finished, unload sample and develop in MF-CD-26 developer in wet bay for 40 seconds.
- Rinse with acetone + IPA 3x and dry with N_2.

Step 3b. Electron beam lithography to define pillars using PMMA resist. This has only been performed in the Elionix. Note that the photomasks for magnetic field control lack device labels, so it would be a good idea to write the labels here at the same time as the alignment marks. Make a separate, high beam current layer to write the large features.

- Spin on PMMA A4 resist, pre-spin at 500 RPM for 5 seconds, spin at 4000 RPM for 60 seconds for 200 nm thick resist. Spin curves are available online for the various PMMA formulations. The PMMA should be at least 5x as thick as the metallic mask deposited at the end of this step.
- Pre-bake at 180°C for 90 seconds.
- Follow usual e-beam lithography procedure for the Elionix. Use 100 kV and 1 nA beam current to write well-separated pillars with dimensions greater than 30 nm. You may need to use lower beam currents for smaller or denser features. The entire write takes about 40 minutes using 1 nA for all features. You may choose to use higher beam current for the photo alignment marks to speed up the process.
- After lithography is finished, unload sample and develop in 4:1 IPA/MIBK developer in wet bay for 2 minutes.
- Rinse with DI water and dry with N_2.
- Deposit 10 nm of Cr, Ta, Ti, or Ru onto the developed PMMA.
- Lift off the PMMA by sonicating at 140 kHz and 100% power for 8-10 minutes.

Step 4. RIE, Ion milling and passivation of MTJ devices

- The patterns defined by electron beam lithography are now transferred into the C/SiN_x hard mask using RIE.
    - Recipe: BPSINC.
    - Chuck: Al.
    - SiN_x etching rate is about 9 nm/min.
    - C etching rate is about 10 nm/min.
- The C/SiN_x hard mask is used to transfer the patterns into the MTJ/Pt stack with ion milling. SIMS is used to monitor the etch until the appropriate etch depth is reached.
    - Ion milling is done using the Commonwealth Scientific Ion Mill.
    - 40 mA, 500 V (500 eV Ar^+ ions).
    - First mill: Angle of 22.5 degrees and endpoint/SIMS assisted, look for MgO signal to drop away entirely for indication that tunnel junction has been milled through.
    - Second mill: Angle of 85 degrees and 28 seconds, used to clean up redeposition on the sides of the devices.
- After milling, quickly deposit at least 100 nm of SiN_x using 5T #4 (recipe above) – this will act as a passivating layer for the MTJ devices. Taller pillars will require thicker passivation layers. It is best to move the sample directly from the ion mill to the sputtering chamber to prevent excessive oxidation of the pillars.
- The SiN_x deposited on top of the MTJ devices needs to be planarized after the passivating deposition step. This is done with a long Argon ion milling step at glancing incidence relative to the plane of the substrate. Followed by a briefer mill at normal incidence.
    - 40 mA, 500 V (500 eV Ar^+ ions).
    - First mill: Angle of 272.5 degrees for 20 minutes. Taller pillars will need more planarization time.
    - Second mill: Angle of 0 degrees for 30 seconds

Step 5. Photolithography and ion milling to define bottom leads (L2 mask). This electrically separates all of the MTJ devices.

- Spin on HDMS resist, pre-spin at 600 RPM for 6 seconds, spin at 4000 RPM for 45 seconds.
- Spin on AZ4110 resist, pre-spin at 600 RPM for 6 seconds, spin at 4000 RPM for 45 seconds.
- Pre-bake resist at 95°C for 4 minutes.
- Expose using MA6 contact aligner for 175 seconds.
- Develop in 4:1 H_2O:AZ Developer for 1.6 minutes.
- (Optional but recommended) Descum the sample in PT 790 using Mr. Pink recipe.
- RIE to define bottom leads in top SiN_x layer. Etch through the entire deposited thickness of SiN_x.
  - Recipe: SKPSIN.
  - Chuck: Carbon.
  - Rate: 9 nm/min
- Ar ion milling with endpoint detection to mill to bottom Si/SiO_x layer beneath MTJ stack:
  - 40 mA, 500 V.
  - Mill until SIMS signal shows bottom metal layers have been etched away.
  - Angle: 45°
- Remove AZ resist by sonicating substrate for 8 minutes in acetone. Rinse with IPA and blow dry with N_2.

Step 6. Photolithography and RIE for defining vias to MTJs (L3 mask)

- Sputter 150 nm of SiN_x using 5T #4 (recipe above). This will set the separation distance between top and bottom leads, and thus affect the device capacitance, so think about the timescales of your experiment.
- Spin on HDMS resist, pre-spin at 600 RPM for 6 seconds, spin at 4000 RPM for 45 seconds.
- Spin on AZ4110 resist, pre-spin at 600 RPM for 6 seconds, spin at 4000 RPM for 45 seconds.
- Pre-bake resist at 95°C for 4 minutes.

- Expose using MA6 contact aligner for 60 seconds.
- Develop in 4:1 H_2O:AZ Developer for 2 minutes.
- (Optional but recommended) Descum the sample in the PT 790 using Mr. Pink recipe.
- RIE to etch via down entirely to top of MTJ device. Be very careful with this step. I usually etch through only the thickness of SiN_x deposited at the beginning of this step.
    - Recipe: SKPSIN.
    - Chuck: Carbon.
    - Rate: 9 nm/min.
- Remove AZ resist by sonicating substrate for 5 minutes in acetone. Blow dry with N_2.
- IMPORTANT: At this point it is imperative to do SEM to see if the vias have been etched down far enough to expose the carbon cap on top of the MTJ devices. If the etch has gone far enough, you should see the carbon pointing up above the level of the backetched SiN_x. The contrast here can be subtle. It is also possible to see the carbon despite it being buried under a few nanometers of SiN_x. The best practice I have found is to perform the oxygen plasma etch and check for an inversion of the edge contrast. The MTJ's should be found in a similar location in each cross/via junction.
- If the MTJs are visible, then proceed to step 8.
- If they are not visible, then alternatingly etch 20 nm of SiN_x across the whole sample and inspect with SEM until the tops of devices are visible. Careful attention at this step will ensure good electrical connection to the MTJ devices through the top electrodes!!!
- Once the carbon cap on the MTJ is exposed, use oxygen plasma to remove the carbon cap and expose the top of the MTJ.
    - Recipe: BPO2.
    - Chuck: Al.
    - Rate: 10 nm/min.
    - Do not be afraid to over etch. You need to get all the carbon out, and the metal below won't be hurt by O_2 plasma.
- Check again in the SEM to ensure the edge contrast has inverted, indicating that the feature has changed from a pillar of carbon pointing up out of the SiN_x to a hole in the SiN_x. If the contrast does not invert, etch another 10 nm of SiN_x and repeat the oxygen plasma etch. Check again in the SEM. If the contrast still isn't changing, consider other methods of diagnosing the problem, such as AFM to determine if you've got a pillar or a hole or just a smooth surface.

<u>Step 7</u>. Photolithography and RIE for defining vias to bottom leads (L4 mask)

- Spin on HDMS resist, pre-spin at 600 RPM for 6 seconds, spin at 4000 RPM for 45 seconds.
- Spin on AZ4110 resist, pre-spin at 600 RPM for 6 seconds, spin at 4000 RPM for 45 seconds.
- Pre-bake resist at 95°C for 4 minutes.
- Expose using MA6 contact aligner for 60 seconds.
- Develop in 4:1 H_2O:AZ Developer for 2 minutes.
- (Optional but recommended) Descum the sample in PT 790 using Mr. Pink recipe.
- RIE to define via in top SiN_x layer:
    - Recipe: SKPSIN.
    - Chuck: Carbon.
    - Rate: 9 nm/min.
- Remove AZ resist by sonicating substrate for 8 minutes in acetone. Rinse with IPA and blow dry with N_2.

<u>Step 8</u>. Photolithography for defining top leads (L5 mask). If want to use patterned leads for magnetic field control, use the L5 mask that omits two of the bottom lead connections.

- Spin on HDMS resist, pre-spin at 600 RPM for 6 seconds, spin at 4000 RPM for 45 seconds.
- Spin on NR9-1000PY resist, pre-spin at 600 RPM for 6 seconds, spin at 4000 RPM for 30 seconds.
- Pre-bake resist at 110°C for 2 minutes.
- Remove the edge bead.
- Expose using MA6 contact aligner for 8 seconds.
- Post bake at 110°C for 2 minutes. This is easy to forget!
- Develop in MF CD-26 for 12 seconds.

Step 9. Deposit Pt or Au for top leads

- Perform a sputter etch at 200 W RF for 60s to remove any remaining adhesion layer from the top of the MTJ that was used to stick the carbon and clean up the contacts. Talk to the nanofab staff about how to do the etch if you don't know how.
- Sputter Pt on an adhesion layer (Ti, Ta and Cr are good known adhesion layers).
- Deposit in the 5T #5 using Ta and Pt. 5T #5 has a load lock which greatly expedites the sputtering procedure.
    - Presputter Pt for 1 min at 50 W DC.
    - Presputter Ta for 5 min at 100 W RF.
    - Sputter Ta for 46 seconds at 100 W RF (~10 nm Ta).
    - Sputter Pt for 509 sec at 50 W for ~120 nm of Pt.
- Remove AZ resist by sonicating substrate for 8 minutes in acetone. Rinse with IPA and blow dry with N_2.

Step 10. If using STT or SOT control, skip to step 14. If using magnetic field control, deposit SiN_x to vertically separate the MTJ connections from the magnetic field generating lead. This will require some calculation to determine the distance between the MTJ and the field-generating wire. I calculated 200 nm for the KAUST films, but this will vary based on the coercivity of your devices.

Step 11. Photolithography to define vias to the L5 pads using the photo mask with 6 square vias per device.

- Spin on HDMS resist, pre-spin at 600 RPM for 6 seconds, spin at 4000 RPM for 45 seconds.
- Spin on AZ4110 resist, pre-spin at 600 RPM for 6 seconds, spin at 4000 RPM for 45 seconds.
- Pre-bake resist at 95°C for 4 minutes.
- Expose using MA6 contact aligner for 60 seconds.
- Develop in 4:1 H_2O:AZ Developer for 2 minutes.

- (Optional but recommended) Descum the sample in PT 790 using Mr. Pink recipe.
- RIE to define via in SiN_x layer:
    - Recipe: SKPSIN.
    - Chuck: Carbon.
    - Rate: 9 nm/min.
- Remove AZ resist by sonicating substrate for 8 minutes in acetone. Rinse with IPA and blow dry with N_2.

Step 12. Photolithography to define magnetic field lead and device connection bond pads. Use the final mask with 6 bond pads and one long lead coving the center of device.

- Spin on HDMS resist, pre-spin at 600 RPM for 6 seconds, spin at 4000 RPM for 45 seconds.
- Spin on NR9-1000PY resist, pre-spin at 600 RPM for 6 seconds, spin at 4000 RPM for 30 seconds.
- Pre-bake resist at 110°C for 2 minutes.
- Remove the edge bead.
- Expose using MA6 contact aligner for 8 seconds.
- Post bake at 110°C for 2 minutes. This is easy to forget!
- Develop in MF CD-26 for 12 seconds.

Step 13. Deposit Pt or Au for final leads

- Sputter Pt on an adhesion layer (Ti, Ta and Cr are good known adhesion layers).
- Deposit in the 5T #5 using Ta and Pt. 5T #5 has a load lock which greatly expedites the sputtering procedure.
    - Presputter Pt for 1 min at 50 W DC.
    - Presputter Ta for 5 min at 100 W RF.
    - Sputter Ta for 46 seconds at 100 W RF (~10 nm Ta).
    - Sputter Pt for 509 sec at 50 W for ~120 nm of Pt.

- Remove AZ resist by sonicating substrate for 8 minutes in acetone. Rinse with IPA and blow dry with N_2.

Step 14: Coat in baked resist for dicing

- Spin HMDS adhesion promoter at 4000 rpm. Spin AZ4110 resist at 4000 rpm.
- Bake on 95C hot plate for 5 minutes.
- Leave with clean room staff for dicing (explain the dicing tracks on the sample if the staff member is not familiar with this sample from previous dicing runs)
- Sonicate for 5-10 minutes in acetone after dicing to remove AZ4110 resist.

State of sample after each step:

1. Additional layers are sputtered on top of the MTJ stack in preparation for patterning. A Pt layer (20-30 nm) is sputtered on top for good electrical contact through backetched vias at the end of the process. Also, A C/SiN_x layer is sputtered on top to serve as a hard mask for pattern transfer of the MTJ devices.
2. Alignment marks made of Ta are defined on top of the C/SiN_x hard mask layer and the sample is ready for electron beam lithography.
3. The devices have been defined in exposed and developed HSQ.
4. The MTJ device patterns have been transferred into the underlying MTJ film stack and passivated with SiN_x.
5. The bottom leads have been defined with the L2 mask.
6. First photolithography step for via formation is complete (L3 mask). Important to INSPECT WITH SEM HERE.
7. Second photolithography step for via formation is complete (L4 mask).
8. Top MTJ connection leads have been defined using photolithography and the L5 mask.
9. Top MTJ connection leads fabricated with Pt deposition and liftoff.
10. Sample is coated with SiN_x build-up layer.

11. Vias to top MTJ connection leads are etched through SiN_x.
12. Final lead layer is defined in photoresist.
13. Final leads are deposited.
14. Sample is diced.

APPENDIX B Process Flow for Spin Hall Effect Devices

This appendix describes the process flow for fabricating patterned magnetic tunnel junctions (MTJs) on top of Hall Cross intersections. The stack structure and fabrication scheme are designed so that MTJ devices are situated on top of a thin metal lead. A Ta underlayer is often chosen because of its efficiency for spin orbit torque.

The chip layout is organized so that the devices can be manipulated/measured with both hardwired current injection and CAFM. At the end of the fabrication scheme, each sample consists of a single wafer-cut die with 6 Hall Cross intersections. MTJ devices are patterned at the center of each Hall intersection. Each Hall Cross consists of two, 10 μm wide, intersecting leads patterned from the metal layer beneath the MTJ layers. Beyond the immediate vicinity of the Hall Cross intersection, 200 nm of Pt is sputtered atop the heavy metal leads to reduce resistance in the SOT leads. 150 μm wide, 200 nm thick, Pt bonding pads are located at the edge of the sample for wire bonding and hardwired current injection.

Wire bonding was done with the assistance of Michael Sinko in Benjamin Hunt's lab at CMU. The gold wires bonded to the samples were 1 mm thick and had an estimated current capacity of 0.5 Amps. Current higher than this critical value heats the gold wires and causes them to melt.

I recommend carefully inspecting the sample with an optical microscope between steps to ensure everything is going well. Do not remove the sample from the clean room until the full process is completed. Descumming in the PT790 using the Mr. Pink recipe after each photolithography development can help improve the edges of the photolithography features.

When aligning samples with the MA6 contact aligner, it is best to compare alignment on two sets of alignment marks spaced far apart across the sample. In order to converge on the best possible alignment, you should do an X,Y alignment first with one set of marks. Then, scan to the second set of marks and align them as best as you can by rotating half the distance to the alignment marks and finishing with X,Y alignment. At this point, you scan back to the first set of marks and repeat the half rotation and half X,Y alignment. Successive iterations of this process will result in an optimal X,Y and rotation alignment across the whole sample. This is especially important for the Hall Cross devices because the functionality of the sample depends on devices being patterned precisely at each Hall Cross.

This process flow was originally written by Stephan Piotrowski on 8/29/16 and modified by Samuel Oberdick. I further modified the process based on my own experience in using it several times.

This process has not yet been run with the new Elionix e-beam writer, and likely requires further modification. I'm writing this how I would plan a first attempt using the Elionix. A new CAD file will be required.

Process Flow

Step 1: Photolithography to define e-beam alignment marks. These could also be included in the E-beam write, in which case this step can be skipped.

- Spin HMDS adhesion promoter at 4000 rpm for 60 seconds. Spin NR9-1000PY resist at 4000 rpm for 60 seconds.
- Bake on 110°C hot plate for 2 minutes.
- Expose using the L1 mask in the MA6 for 8 seconds.
- Post bake on 110°C hot plate for 2 minutes.
- Develop in CD-26 for 12 seconds.
- Deposit 100 nm of Ta.
- Lift off by sonicating in acetone at 140 kHz and 100% power for 8 minutes.

<u>Step 2:</u> Hard mask deposition for ion milling of e-beam patterns.

This can take many forms. Consult the table of ion milling rates to determine what hard mask is right for you. You may wish to deposit a film of silicon nitride to act as the ion milling hard mask or use a lift off process to deposit islands of Cr/Ru to act as hard mask.

<u>Step 3:</u> Electron beam lithography

Write devices with electron beam lithography on PMMA

- Spin on PMMA A2 or A7, pre-spin at 500 RPM for 6 seconds, spin at 4000 RPM for 60 seconds.
- Pre-bake at 180°C for 2 minutes.
- Load into the Elionix for electron beam lithography
- Follow usual e-beam lithography procedure
- The write is done at 100 kV and 1 nA beam current.
- After lithography is finished, develop in 4:1 IPA:MIBK developer for 2 minutes.

<u>Step 4:</u> Deposit metal into PMMA trenches.

- If using SiN_x hard mask, deposit 3-5 nm of adhesive metal (Cr, Ta, or Ti) on the developed PMMA and lift off by sonicating in acetone for 8 minutes at 140 kHz and 100% power. Etch the SiN_x by RIE in the PT 790 using the SKPSIN recipe. This recipe etches SiN_x at a rate of 9-12 nm per minute depending upon some gas calibration conditions. You should be doing regular rate tests of the PT 790 system and using your latest rate results.

- If using metal hard mask, deposit the desired thickness here. Remember to include an adhesion layer as native oxide may have grown on the film surface. Lift off by sonicating as described above.

Step 5: Ion mill to bottom lead

- Using SIMS (Secondary ion mass spectroscopy) to observe the Mg, Ru, Co, and Ta signal, mill at 22.5° until the bottom CoFeB layer is fully removed and the heavy metal layer beneath it is exposed. SIMS data is displayed in Figure B-1
- Optionally, mill for an additional 23 seconds at 85° to remove redeposited material
- Sonicate the sample in acetone to remove the resist. Five minutes is usually sufficient.

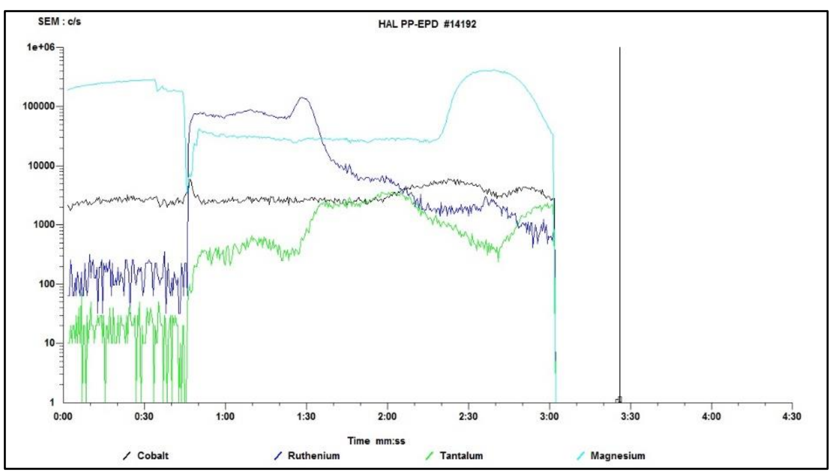

Figure B-1. SIMS signal for ion milling to base Ta layer. The four colored time traces indicate mass spectroscopy signals from four distinct elements – Co, Ru, Ta and Mg. At 45 seconds, the grounded shield in front of the sample is removed and milling begins. From 45 seconds to 1 minute 30 seconds, the top Ru layer is etched. From 1 minute 30 seconds to about 2 minutes, the topmost Ta layer is etched. Then,

from 2 minutes to 3 minutes the CoFeB/MgO/CoFeB tunnel barrier is etched. Note that two small peaks are visible in the Co signal for each CoFeB layer. The etch is stopped when the Mg/Co signal has dropped, and the Ta signal has reached a maximum.

Step 6: Photolithography to define base leads

- Spin HMDS adhesion promoter at 4000 rpm for 60 seconds. Spin AZ4110 resist at 4000 rpm for 60 seconds.
- Bake on 95°C hot plate for 4 minutes.
- Remove the edge-bead left by beaded resist at edge of substrate (optional).
- Align the L2 mask alignment marks to the alignment marks left from the L1 or e-beam process.
- Expose using the L2 mask in the MA6 for 45 seconds.
- Develop in 4:1 AZ 400K:DI water for ~1 minute and 15 seconds.

Step 7: Ion milling to create leads

- Using SIMS to observe the Ru, and Ta signal, mill at 22.5° until the bottom Ta layer is completely gone.
- Sonicate the sample in acetone to remove the resist. Five minutes is usually sufficient.

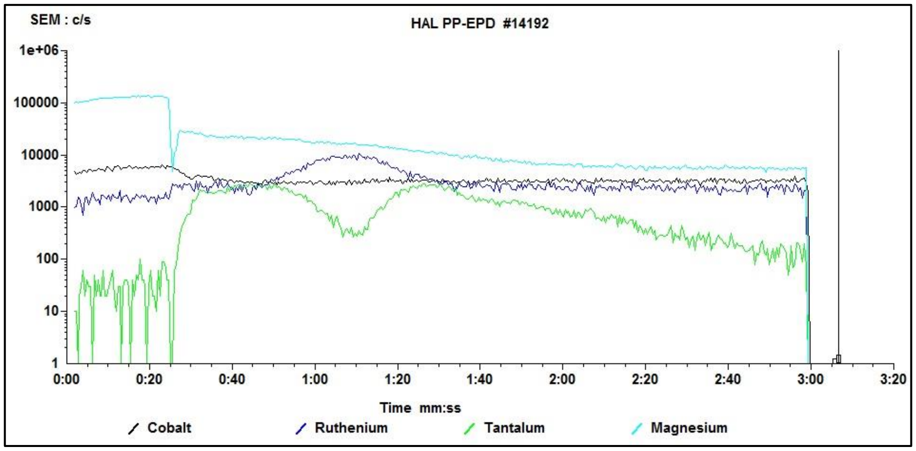

Figure B-2. SIMS signal from second ion milling step. The grounded shield in front of the sample is removed at 25 seconds and the etch begins. The topmost Ta layer is first milled away. Then, from 50 seconds to 1 minute 25 seconds the Ruthenium layer is milled away. At 1 minute 25 seconds, the Ru signal decreases and the Ta signal rises, indicating that the bottom most Ta layer is being etched. The etch continues until the Ta falls to background levels, indicating that the Ta has been etched away entirely.

<u>Step 8:</u> Photolithography to create resist trenches for Pt lift-off

- Spin HMDS adhesion promoter at 4000 rpm. Spin NR9-1000PY resist at 4000 rpm.
- Bake on 110°C hot plate for 2 minutes.
- Remove the edge bead (optional).
- Align the L3 mask alignment marks to the alignment marks left from the L2 process. There are also L1 to L3 alignment marks which ideally should be aligned simultaneously.
- Expose using the L3 mask in the MA6 for 8 seconds.
- Post bake on 110°C hot plate for 2 minutes.
- Develop in CD-26 for 12 seconds.

<u>Step 9:</u> Pt deposition and lift-off

Sputter Pt on an adhesion layer (Ta, Cr, or Ti).

To complete the liftoff, sonicate the sample in acetone for about 8 minutes at 140 kHz and 100% power or until all of the Pt has clearly lifted off.

Step 10: Remove SiNx hard mask

Perform the CF4/CHF3 RIE with 10% over etch to remove any residual SiNx remaining on the devices.

- Etched for 1 minute and 40 seconds using CF4/CHF3 RIE, 10% over etch accounting for ion milling in step 2

Step 11: Coat in baked resist for dicing

- Spin HMDS adhesion promoter at 4000 rpm. Spin AZ4110 resist at 4000 rpm.
- Bake on 95°C hot plate for 5 minutes.
- Leave with clean room staff for dicing (explain the dicing tracks on the sample if the staff member is not familiar with this sample from previous dicing runs)
- Sonicate for 5-10 minutes in acetone after dicing to remove AZ4110 resist

State of sample after each step:

15. Alignment marks are defined
16. Hard mask is deposited, if applicable
17. Devices are defined in the PMMA resist
18. Metal mask is deposited
19. MTJs pillars are milled out
20. SOT leads are defined in photoresist
21. SOT leads are milled out of the heavy metal film
22. Pt leads are defined in the photoresist
23. Pt leads are deposited
24. Residual SiN_x hard mask is removed, if applicable
25. The sample is finished

References

[1] Wi. Thomson, *On the Electro-Dynamic Qualities of Metals:—Effects of Magnetization on the Electric Conductivity of Nickel and of Iron*, Proc. R. Soc. London **8**, 546 (1857).

[2] R. P. Hunt, *A Magnetoresistive Readout Transducer*, IEEE Trans. Magn. **7**, 150 (1971).

[3] M. N. Baibich, J. M. Broto, A. Fert, F. N. Van Dau, F. Petroff, P. Eitenne, G. Creuzet, A. Friederich, and J. Chazelas, *Giant Magnetoresistance of (001)Fe/(001)Cr Magnetic Superlattices*, Phys. Rev. Lett. **61**, 2472 (1988).

[4] G. Binasch, P. Grünberg, F. Saurenbach, and W. Zinn, *Enhanced Magnetoresistance in Layered Magnetic Structures with Antiferromagnetic Interlayer Exchange*, Phys. Rev. B **39**, 4828 (1989).

[5] C. Tsang, R. E. Fontana, T. Lin, D. E. Heim, V. S. Speriosu, B. A. Gurney, and M. L. Williams, *Design, Fabrication, & Testing of Spin-Valve Read Heads for High Density Recording*, IEEE Trans. Magn. **30**, 3801 (1994).

[6] D. Hannon, M. Krounbi, and J. Christner, *Allicat Magnetoresistive Head Design and Performance*, IEEE Trans. Magn. **30**, 298 (1994).

[7] A. Wallash, *A Study of Voltage Fluctuation, Noise and Magnetic Instability in Spin Valve GMR Recording Heads*, IEEE Trans. Magn. **34**, 1450 (1998).

[8] T. Nakatani, S. Li, Y. Sakuraba, T. Furubayashi, and K. Hono, *Advanced CPP-GMR Spin-Valve Sensors for Narrow Reader Applications*, IEEE Trans. Magn. **54**, (2018).

[9] J. S. Moodera, L. R. Kinder, T. M. Wong, and R. Meservey, *Large Magnetoresistance at Room Temperature in Ferromagnetic Thin Film Tunnel Junctions*, Phys. Rev. Lett. **74**, 3273 (1995).

[10] S. Z. Peng, Y. Zhang, M. X. Wang, Y. G. Zhang, and W. Zhao, *Magnetic Tunnel Junctions for Spintronics: Principles and Applications*, Wiley Encycl. Electr. Electron. Eng. **1936**, 1 (2014).

[11] J. F. Gregg, I. Petej, E. Jouguelet, and C. Dennis, *Spin Electronics - A Review*, J. Phys. D. Appl. Phys. **35**, (2002).

[12] M. Julliere, *Tunneling between Ferromagnetic Films*, Phys. Lett. A **54**, 225 (1975).

[13] W. H. Butler, *Tunneling Magnetoresistance from a Symmetry Filtering Effect*, Sci. Technol. Adv. Mater. **9**, (2008).

[14] S. S. P. Parkin, Z. G. Li, and D. J. Smith, *Giant Magnetoresistance in Antiferromagnetic Co / Cu Multilayers*, Appl. Phys. Lett. **58**, 2710 (1991).

[15] S. S. P. Parkin, *Giant Magneto Resistance in Magnetic Nanostructures*, Annu Rev Mater Sci **25**, 357 (1995).

[16] H. Kano, K. Kagawa, A. Suzuki, A. Okabe, K. Hayashi, and K. Aso, *Substrate Temperature Effect on Giant Magnetoresistance of Sputtered Co/Cu Multilayers*, Appl. Phys. Lett. **63**, 2839 (1993).

[17] S. Ikeda, J. Hayakawa, Y. Ashizawa, Y. M. Lee, K. Miura, H. Hasegawa, M. Tsunoda, F. Matsukura, and H. Ohno, *Tunnel Magnetoresistance of 604% at 300 K by Suppression of Ta Diffusion in CoFeBMgOCoFeB Pseudo-Spin-Valves Annealed at High Temperature*, Appl. Phys. Lett. **93**, 1 (2008).

[18] B. Parks, M. Bapna, J. Igbokwe, H. Almasi, W. Wang, and S. A. Majetich, *Superparamagnetic Perpendicular Magnetic Tunnel Junctions for True Random Number Generators*, AIP Adv. **8**, (2018).

[19] M. Bapna, B. Parks, S. Oberdick, H. Almasi, C. Sun, and P. Voyles, *Effect of Mo Capping in Sub-100 Nm CoFeB-MgO Tunnel Junctions with Perpendicular Magnetic Anisotropy*, (2019).

[20] B. Parks, A. Abdelgawad, T. Wong, R. F. L. Evans, and S. A. Majetich, *Magnetoresistance Dynamics in Superparamagnetic Co-Fe- B Nanodots*, Phys. Rev. Appl. **13**, 1 (2020).

[21] H. Jin and T. Miyazaki, *Tunnel Magnetoresistance Effect*, in *The Physics of Ferromagnetism* (Springer Berlin Heidelberg, Berlin, Heidelberg, 2012), pp. 403–432.

[22] H. Jin and T. Miyazaki, *Magnetic Anisotropy*, in *The Physics of Ferromagnetism* (Springer Berlin Heidelberg, Berlin, Heidelberg, 2012), pp. 205–243.

[23] Y. Xie, Q. Zhan, Y. Hu, X. Hu, X. Chi, C. Zhang, H. Yang, W. Xie, X. Zhu, J. Gao, W. Cheng, D. Jiang, and R. W. Li, *Magnetocrystalline Anisotropy Imprinting of an Antiferromagnet on an Amorphous Ferromagnet in FeRh/CoFeB Heterostructures*, NPG Asia Mater. **12**, (2020).

[24] S. K. Piotrowski, M. Bapna, S. D. Oberdick, and S. A. Majetich, *Size and Voltage Dependence of Interface Anisotropy in Sub-100 Nm Perpendicular Magnetic Tunnel Junctions*, Phys. Rev. B **94**, 1 (2016).

[25] N. Nakajima, T. Koide, T. Shidara, H. Miyauchi, H. Fukutani, A. Fujimori, K. Iio, T. Katayama, M. Nývlt, and Y. Suzuki, *Perpendicular Magnetic Anisotropy Caused by Interfacial Hybridization via Enhanced Orbital Moment in Co/Pt Multilayers: Magnetic Circular X-Ray Dichroism Study*, Phys. Rev. Lett. **81**, 5229 (1998).

[26] R. Shimabukuro, K. Nakamura, T. Akiyama, and T. Ito, *Electric Field Effects on Magnetocrystalline Anisotropy in Ferromagnetic Fe Monolayers*, Phys. E Low-Dimensional Syst. Nanostructures **42**, 1014 (2010).

[27] H. Jin and T. Miyazaki, *Exchange Interaction*, in *The Physics of Ferromagnetism* (Springer Berlin Heidelberg, Berlin, Heidelberg, 2012), pp. 175–204.

[28] M. Kiwi, *Exchange Bias Theory*, J. Magn. Magn. Mater. **234**, 584 (2001).

[29] M. Bapna and S. A. Majetich, *Current Control of Time-Averaged Magnetization in Superparamagnetic Tunnel Junctions*, Appl. Phys. Lett. **111**, (2017).

[30] S. Ikeda, K. Miura, H. Yamamoto, K. Mizunuma, H. D. Gan, M. Endo, S. Kanai, J. Hayakawa, F. Matsukura, and H. Ohno, *A Perpendicular-Anisotropy CoFeB-MgO Magnetic Tunnel Junction.*, Nat. Mater. **9**, 721 (2010).

[31] W.-G. Wang, M. Li, S. Hageman, and C. L. Chien, *Electric-Field-Assisted Switching in Magnetic Tunnel Junctions*, Nat. Mater. **11**, 64 (2011).

[32] M. Bapna, B. Parks, S. D. Oberdick, H. Almasi, W. Wang, and S. A. Majetich, *Spin-Orbit-Torque Switching in 20-Nm Perpendicular Magnetic Tunnel Junctions*, Phys.

Rev. Appl. **10**, 1 (2018).

[33] W. F. Brown, *Thermal Fluctuations of a Single-Domain Particle*, Phys. Rev. **130**, 1677 (1963).

[34] P. L. Lu and S. H. Charap, *High Density Magnetic Recording Media Design and Identification: Susceptibility to Thermal Decay*, IEEE Trans. Magn. **31**, 2767 (1995).

[35] J. P. Eckert, *A Survey of Digital ComputerMemory Systems **, Proc. IRE **41**, 1393 (1953).

[36] D. Apalkov, B. Dieny, and J. M. Slaughter, *Magnetoresistive Random Access Memory*, Proc. IEEE **104**, 1796 (2016).

[37] S. Ikegawa, F. B. Mancoff, J. Janesky, and S. Aggarwal, *Magnetoresistive Random Access Memory: Present and Future*, IEEE Trans. Electron Devices **67**, 1407 (2020).

[38] K. Y. Camsari, S. Salahuddin, and S. Datta, *Implementing P-Bits with Embedded MTJ*, IEEE Electron Device Lett. **38**, 1767 (2017).

[39] W. A. Borders, A. Z. Pervaiz, S. Fukami, K. Y. Camsari, H. Ohno, and S. Datta, *Integer Factorization Using Stochastic Magnetic Tunnel Junctions*, Nature **573**, 390 (2019).

[40] K. Y. Camsari, B. M. Sutton, and S. Datta, *P-Bits for Probabilistic Spin Logic*, Appl. Phys. Rev. **6**, (2019).

[41] K. Y. Camsari, R. Faria, O. Hassan, A. Z. Pervaiz, B. M. Sutton, and S. Datta, *P-Transistors and p-Circuits for Boolean and Non-Boolean Logic*, 91 (2017).

[42] M. W. Daniels, A. Madhavan, P. Talatchian, A. Mizrahi, and M. D. Stiles, *Energy-Efficient Stochastic Computing with Superparamagnetic Tunnel Junctions*, Phys. Rev. Appl. **13**, 1 (2020).

[43] C. P. Bean, *Hysteresis Loops of Mixtures of Ferromagnetic Micropowders*, J. Appl. Phys. **26**, (1955).

[44] C. P. Bean and J. D. Livingston, *Superparamagnetism*, J. Appl. Phys. **30**, S120

(1959).

[45] L. Néel, *Influence Des Fluctuations Thermiques Sur l ' Aimantation de Grains Ferromagnétiques Très Fins*, Comptes Rendus Hebd. Des Seances L Acad. Des Sci. **228**, 664 (1949).

[46] S. K. Piotrowski, M. F. Matty, and S. A. Majetich, *Magnetic Fluctuations in Individual Superparamagnetic Particles*, IEEE Trans. Magn. **50**, 18 (2014).

[47] L. Berger, *Emission of Spin Waves by a Magnetic Multilayer Traversed by a Current*, Phys. Rev. B **54**, 9353 (1996).

[48] J. C. Slonczewski, *Current-Driven Excitation of Magnetic Multilayers*, J. Magn. Magn. Mater. **159**, (1996).

[49] J. C. Slonczewski, *Currents, Torques, and Polarization Factors in Magnetic Tunnel Junctions*, Phys. Rev. B - Condens. Matter Mater. Phys. **71**, 1 (2005).

[50] I. M. Miron, K. Garello, G. Gaudin, P.-J. Zermatten, M. V Costache, S. Auffret, S. Bandiera, B. Rodmacq, A. Schuhl, and P. Gambardella, *Perpendicular Switching of a Single Ferromagnetic Layer Induced by In-Plane Current Injection*, Nature **476**, (2011).

[51] A. Harres and J. Geshev, *A Polycrystalline Model for Magnetic Exchange Bias*, J. Phys. Condens. Matter **24**, (2012).

[52] J. D. Livingston and C. P. Bean, *Specific Heat of Superparamagnetic Particles*, J. Appl. Phys. **32**, 1964 (1961).

[53] F. G. West, *General Superparamagnetic Behavior of an Aligned Assembly of Uniaxially Anisotropic Particles*, J. Appl. Phys. **32**, 249S (1961).

[54] P. J. Cregg and L. Bessais, *Series Expansions for the Magnetisation of a Solid Superparamagnetic System of Non-Interacting Particles with Anisotropy*, J. Magn. Magn. Mater. **202**, 554 (1999).

[55] W. Hellenthal, *Superparamagnetic Effects in Thin Films*, IEEE Trans. Magn. **4**, 11 (1968).

[56] J. E. Hirsch, *Spin Hall Effect*, Phys. Rev. Lett. **83**, 1834 (1999).

[57] G. Bihlmayer, Y. M. Koroteev, P. M. Echenique, E. V. Chulkov, and S. Blügel, *The Rashba-Effect at Metallic Surfaces*, Surf. Sci. **600**, 3888 (2006).

[58] I. M. Miron, K. Garello, G. Gaudin, P.-J. Zermatten, M. V. Costache, S. Auffret, S. Bandiera, B. Rodmacq, A. Schuhl, and P. Gambardella, *Perpendicular Switching of a Single Ferromagnetic Layer Induced by In-Plane Current Injection*, Nature (2011).

[59] H. Sato, M. Yamanouchi, K. Miura, S. Ikeda, H. D. Gan, K. Mizunuma, R. Koizumi, F. Matsukura, and H. Ohno, *Junction Size Effect on Switching Current and Thermal Stability in CoFeB/MgO Perpendicular Magnetic Tunnel Junctions*, Appl. Phys. Lett. **99**, (2011).

[60] H. Sato, M. Yamanouchi, S. Ikeda, S. Fukami, F. Matsukura, and H. Ohno, *Perpendicular-Anisotropy CoFeB-MgO Magnetic Tunnel Junctions with a MgO/CoFeB/Ta/CoFeB/MgO Recording Structure*, Appl. Phys. Lett. **101**, 022414 (2012).

[61] M. Xiao, K. B. Klaassen, J. C. L. Van Peppen, and M. H. Kryder, *Extra-Low-Frequency Noise in Giant Magnetoresistance Recording Heads*, J. Appl. Phys. **85**, 5855 (1999).

[62] S. K. Piotrowski, M. Bapna, S. D. Oberdick, S. A. Majetich, M. Li, C. L. Chien, R. Ahmed, and R. H. Victora, *Size and Voltage Dependence of Effective Anisotropy in Sub-100-Nm Perpendicular Magnetic Tunnel Junctions*, Phys. Rev. B-Condensed Matter **94**, 014404 (2016).

[63] L. Jiang, E. R. Nowak, P. E. Scott, J. Johnson, J. M. Slaughter, J. J. Sun, and R. W. Dave, *Low-Frequency Magnetic and Resistance Noise in Magnetic Tunnel Junctions*, Phys. Rev. B - Condens. Matter Mater. Phys. **69**, 1 (2004).

[64] A. Sengupta, P. Panda, P. Wijesinghe, Y. Kim, and K. Roy, *Magnetic Tunnel Junction Mimics Stochastic Cortical Spiking Neurons*, Sci. Rep. **6**, 30039 (2016).

[65] V. Ostwal, P. Debashis, R. Faria, Z. Chen, and J. Appenzeller, *Spin-Torque Devices with Hard Axis Initialization as Stochastic Binary Neurons*, Sci. Rep. **8**, 1 (2018).

[66] J. M. Slaughter, N. D. Rizzo, J. Janesky, R. Whig, F. B. Mancoff, D. Houssameddine, J. J. Sun, S. Aggarwal, K. Nagel, S. M. Alam, T. Andre, P. Lopresti, and E. Technologies, *High Density ST-MRAM Technology (Invited)*, **85224**, 673 (2012).

[67] K. Hayakawa, S. Kanai, T. Funatsu, J. Igarashi, B. Jinnai, W. A. Borders, H. Ohno, and S. Fukami, *Nanosecond Random Telegraph Noise in In-Plane Magnetic Tunnel Junctions*, Phys. Rev. Lett. **126**, 117202 (2021).

[68] J. M. Slaughter, R. W. Dave, M. Durlam, G. Kerszykowski, K. Smith, K. Nagel, B. Feil, J. Calder, M. DeHerrera, B. Garni, and S. Tehrani, *High Speed Toggle MRAM with MgO-Based Tunnel Junctions*, Tech. Dig. - Int. Electron Devices Meet. IEDM **2005**, 873 (2005).

[69] K. Garello, I. M. Miron, C. O. Avci, F. Freimuth, Y. Mokrousov, S. Blügel, S. Auffret, O. Boulle, G. Gaudin, and P. Gambardella, *Symmetry and Magnitude of Spin–Orbit Torques in Ferromagnetic Heterostructures*, Nat. Nanotechnol. **8**, 587 (2013).

[70] K. Yagami, A. A. Tulapurkar, A. Fukushima, and Y. Suzuki, *Low-Current Spin-Transfer Switching and Its Thermal Durability in a Low-Saturation-Magnetization Nanomagnet*, Appl. Phys. Lett. **85**, 5634 (2004).

[71] D. C. Ralph and M. D. Stiles, *Spin Transfer Torques*, (n.d.).

[72] H. Jin and T. Miyazaki, *MRAM*, in *The Physics of Ferromagnetism* (Springer Berlin Heidelberg, Berlin, Heidelberg, 2012), pp. 433–446.

[73] E. R. Evarts, L. Cao, D. S. Ricketts, N. D. Rizzo, J. A. Bain, and S. A. Majetich, *Spin Transfer Torque Switching of Magnetic Tunnel Junctions Using a Conductive Atomic Force Microscope*, Appl. Phys. Lett. **95**, 93 (2009).

[74] M. Schoolnik and Everspin Technologies, *Everspin Releases Highest Density MRAM Products to Create Fastest And Most Reliable Non-Volatile Storage Class Memory*, (2016).

[75] S. Krause, G. Herzog, A. Schlenhoff, A. Sonntag, and R. Wiesendanger, *Joule*

Heating and Spin-Transfer Torque Investigated on the Atomic Scale Using a Spin-Polarized Scanning Tunneling Microscope, Phys. Rev. Lett. **107**, 1 (2011).

[76] S. Zhang, *Spin Hall Effect in the Presence of Spin Diffusion*, Phys. Rev. Lett. **85**, 393 (2000).

[77] E. I. Rashba and V. I. Sheka, *Symmetry of Energy Bands in Crystals of Wurtzite Type II . Symmetry of Bands with Spin-Orbit Interaction Included Construction of Double-Valued Irreducible Representations*, Dtsch. Phys. Gesellschaft **2**, 162 (1959).

[78] Y. A. Bychkov and E. I. Rashba, *Properties of a 2D Electron Gas with Lifted Spectral Degeneracy*, JETP Lett. **39**, 66 (1984).

[79] K. Ando, S. Takahashi, K. Harii, K. Sasage, J. Ieda, S. Maekawa, and E. Saitoh, *Electric Manipulation of Spin Relaxation Using the Spin Hall Effect*, Phys. Rev. Lett. **101**, 1 (2008).

[80] G. Muller, D. Weiss, A. V. Khaetskii, K. von Klitzing, S. Koch, H. Nickel, W. Schlapp, and R. Losch, *Equilibration Length of Electrons in Spin-Polarized Edge Channels*, Phys. Rev. B **45**, 3932 (1992).

[81] Q. Yang, P. Holody, S. F. Lee, L. L. Henry, R. Loloee, P. A. Schroeder, W. P. Pratt, and J. Bass, *Spin Flip Diffusion Length and Giant Magnetoresistance at Low Temperatures*, Phys. Rev. Lett. **72**, 3274 (1994).

[82] L. Liu, C.-F. Pai, Y. Li, H. W. Tseng, D. C. Ralph, and R. A. Buhrman, *Spin-Torque Switching with the Giant Spin Hall Effect of Tantalum*, Science (80-.). (2012).

[83] K. Tsunekawa, Y. S. Choi, Y. Nagamine, D. D. Djayaprawira, T. Takeuchi, and Y. Kitamoto, *Influence of Chemical Composition of CoFeB on Tunneling Magnetoresistance and Microstructure in Polycrystalline CoFeB/MgO/CoFeB Magnetic Tunnel Junctions*, Japanese J. Appl. Physics, Part 2 Lett. **45**, (2006).

[84] I. M. L. Billas, A. Chatelain, and W. A. De Heer, *Magnetism from the Atom to the Bulk in Iron , Cobalt , and Nickel Clusters,* Science (80-.). **265**, 1682 (1994).

[85] K. Y. Camsari, B. M. Sutton, and S. Datta, *P-Bits for Probabilistic Spin Logic*, Appl.

Phys. Rev. **6**, (2019).

[86] K. Y. Camsari, R. Faria, B. M. Sutton, and S. Datta, *Stochastic P-Bits for Invertible Logic*, Phys. Rev. X **7**, 1 (2017).

[87] K. Y. Camsari, S. Chowdhury, and S. Datta, *Scalable Emulation of Sign-Problem-Free Hamiltonians with Room-Temperature p-Bits*, Phys. Rev. Appl. **12**, 1 (2019).

[88] R. W. Dave, G. Steiner, J. M. Slaughter, J. J. Sun, B. Craigo, S. Pietambaram, K. Smith, G. Grynkewich, M. DeHerrera, J. Åkerman, and S. Tehrani, *MgO-Based Tunnel Junction Material for High-Speed Toggle Magnetic Random Access Memory*, IEEE Trans. Magn. **42**, 1935 (2006).

[89] G. Prenat, B. Dieny, W. Guo, M. El Baraji, V. Javerliac, and J. P. Nozières, *Beyond MRAM, CMOS/MTJ Integration for Logic Components*, IEEE Trans. Magn. **45**, 3400 (2009).

[90] W.-G. Wang, M. Li, S. Hageman, and C. L. Chien, *Electric-Field-Assisted Switching in Magnetic Tunnel Junctions*, (2011).

[91] T. Maruyama, Y. Shiota, T. Nozaki, K. Ohta, N. Toda, M. Mizuguchi, a a Tulapurkar, T. Shinjo, M. Shiraishi, S. Mizukami, Y. Ando, and Y. Suzuki, *Large Voltage-Induced Magnetic Anisotropy Change in a Few Atomic Layers of Iron.*, Nat. Nanotechnol. **4**, 158 (2009).

[92] M. Gajek, J. J. Nowak, J. Z. Sun, P. L. Trouilloud, E. J. O'Sullivan, D. W. Abraham, M. C. Gaidis, G. Hu, S. Brown, Y. Zhu, R. P. Robertazzi, W. J. Gallagher, and D. C. Worledge, *Spin Torque Switching of 20 Nm Magnetic Tunnel Junctions with Perpendicular Anisotropy*, Appl. Phys. Lett. **100**, 1 (2012).

[93] Y. Fan, P. Upadhyaya, X. Kou, M. Lang, S. Takei, Z. Wang, J. Tang, L. He, L.-T. Chang, M. Montazeri, G. Yu, W. Jiang, T. Nie, R. N. Schwartz, Y. Tserkovnyak, and K. L. Wang, *Magnetization Switching through Giant Spin–Orbit Torque in a Magnetically Doped Topological Insulator Heterostructure*, (2014).

[94] L. Liu, O. J. Lee, T. J. Gudmundsen, D. C. Ralph, and R. A. Buhrman, *Current-Induced Switching of Perpendicularly Magnetized Magnetic Layers Using Spin*

Torque from the Spin Hall Effect, Phys. Rev. Lett. **109**, 1 (2012).

[95] Y. W. Oh, S. H. C. Baek, Y. M. Kim, H. Y. Lee, K. D. Lee, C. G. Yang, E. S. Park, K. S. Lee, K. W. Kim, G. Go, J. R. Jeong, B. C. Min, H. W. Lee, K. J. Lee, and B. G. Park, *Field-Free Switching of Perpendicular Magnetization through Spin-Orbit Torque in Antiferromagnet/Ferromagnet/Oxide Structures*, Nat. Nanotechnol. **11**, 878 (2016).

[96] Z. Wang, W. Zhao, E. Deng, J. O. Klein, and C. Chappert, *Perpendicular-Anisotropy Magnetic Tunnel Junction Switched by Spin-Hall-Assisted Spin-Transfer Torque*, J. Phys. D. Appl. Phys. **48**, (2015).

[97] Z. Diao, Z. Li, S. Wang, Y. Ding, A. Panchula, E. Chen, L. C. Wang, and Y. Huai, *Spin-Transfer Torque Switching in Magnetic Tunnel Junctions and Spin-Transfer Torque Random Access Memory*, J. Phys. Condens. Matter **19**, (2007).

[98] K. Lee, K. Yamane, S. Noh, V. B. Naik, H. Yang, S. H. Jang, J. Kwon, B. Behin-Aein, R. Chao, J. H. Lim, K. W. Gan, D. Zeng, N. Thiyagarajah, L. C. Goh, B. Liu, E. H. Toh, B. Jung, T. L. Wee, T. Ling, T. H. Chan, N. L. Chung, J. W. Ting, S. Lakshmipathi, J. S. Son, J. Hwang, L. Zhang, R. Low, R. Krishnan, T. Kitamura, Y. S. You, C. S. Seet, H. Cong, D. Shum, J. Wong, S. T. Woo, J. Lam, E. Quek, A. See, and S. Y. Siah, *22-Nm FD-SOI Embedded MRAM with Full Solder Reflow Compatibility and Enhanced Magnetic Immunity*, Dig. Tech. Pap. - Symp. VLSI Technol. **2018-June**, 183 (2018).

[99] R. Yu, B. F. Miao, L. Sun, Q. Liu, J. Du, P. Omelchenko, B. Heinrich, M. Wu, and H. F. Ding, *Determination of Spin Hall Angle and Spin Diffusion Length in β -Phase-Dominated Tantalum*, Phys. Rev. Mater. **2**, 1 (2018).

[100] B. Jun and P. Kocher, *THE INTEL RANDOM NUMBER GENERATOR*, **27**, 1 (1999).

[101] M. Bucci, L. Germani, R. Luzzi, A. Trifiletti, and M. Varanonuovo, *A High-Speed Oscillator-Based Truly Random Number Source for Cryptographic Applications on a Smart Card IC*, IEEE Trans. Comput. **52**, 403 (2003).

[102] S. G. Bae, Y. Kim, Y. Park, and C. Kim, *3-Gb/s High-Speed True Random Number Generator Using Common-Mode Operating Comparator and Sampling Uncertainty of D Flip-Flop*, IEEE J. Solid-State Circuits **52**, 605 (2017).

[103] D. Vodenicarevic, N. Locatelli, A. Mizrahi, J. S. Friedman, A. F. Vincent, M. Romera, A. Fukushima, K. Yakushiji, H. Kubota, S. Yuasa, S. Tiwari, J. Grollier, and D. Querlioz, *Low-Energy True Random Number Generation with Superparamagnetic Tunnel Junctions for Unconventional Computing*, (2017).

[104] H. Lee, F. Ebrahimi, P. K. Amiri, and K. L. Wang, *Design of High-Throughput and Low-Power True Random Number Generator Utilizing Perpendicularly Magnetized Voltage-Controlled Magnetic Tunnel Junction*, AIP Adv. (2017).

[105] N. Nishimura, T. Hirai, A. Koganei, T. Ikeda, K. Okano, Y. Sekiguchi, and Y. Osada, *Magnetic Tunnel Junction Device with Perpendicular Magnetization Films for High-Density Magnetic Random Access Memory*, J. Appl. Phys. **91**, 5246 (2002).

[106] A. Rukhin, J. Soto, J. Nechvatal, M. Smid, E. Barker, S. Leigh, M. Levenson, M. Vangel, D. Banks, A. Heckert, J. Dray, and S. Vo, *A Statistical Test Suite for Random and Pseudorandom Number Generators for Cryptographic Applications*, (2010).

[107] M. Bapna, S. K. Piotrowski, S. D. Oberdick, M. Li, C. L. Chien, and S. A. Majetich, *Magnetostatic Effects on Switching in Small Magnetic Tunnel Junctions*, Appl. Phys. Lett. **108**, (2016).

[108] Unknown, *Statistical Tests of Random Number Generators*, ACM SIGSIM Simul. Dig. **8**, 85 (1976).

[109] Y. Cai, Z. Cheng, Z. Yang, C. W. Tang, K. M. Lau, and K. J. Chen, *High-Temperature Operation of AlGaN/GaN HEMTs Direct-Coupled FET Logic (DCFL) Integrated Circuits*, IEEE Electron Device Lett. **28**, 328 (2007).

[110] J. C. Slater and G. F. Koster, *Simplified LCAO Method for the Periodic Potential Problem*, Phys. Rev. **94**, 1498 (1954).

[111] J. F. Cornwell, D. M. Hum, and K. G. Wong, *Density of States in Iron*, Phys. Lett.

A **26**, 365 (1968).

[112] C. H. Park, B. C. Lee, and J. I. Lee, *Spin-Asymmetry of the Density of States for Bulk and Surface Fe, Co, and Ni*, J. Korean Phys. Soc. **47**, 655 (2005).

[113] W. H. Butler, *Tunneling Magnetoresistance from a Symmetry Filtering Effect*, Sci. Technol. Adv. Mater. **9**, 014106 (2008).

[114] W. H. Butler, X. G. Zhang, T. C. Schulthess, and J. M. MacLaren, *Spin-Dependent Tunneling Conductance of Fe/MgO/Fe Sandwiches*, Phys. Rev. B - Condens. Matter Mater. Phys. **63**, 544161 (2001).

[115] J. Z. Sun, *Spin-Current Interaction with a Monodomain Magnetic Body: A Model Study*, Phys. Rev. B - Condens. Matter Mater. Phys. **62**, 570 (2000).

[116] R. H. Victora, *Predicted Time Dependence of the Switching Field for Magnetic Materials*, Phys. Rev. Lett. **63**, 457 (1990).

[117] M. P. Sharrock, *Time Dependence of Switching Fields in Magnetic Recording Media (Invited)*, J. Appl. Phys. **76**, 6413 (1994).

[118] I. Theodonis, N. Kioussis, A. Kalitsov, M. Chshiev, and W. H. Butler, *Anomalous Bias Dependence of Spin Torque in Magnetic Tunnel Junctions*, Phys. Rev. Lett. **97**, 2 (2006).

[119] A. Manchon and S. Zhang, *Theory of Spin Torque Due to Spin-Orbit Coupling*, Phys. Rev. B - Condens. Matter Mater. Phys. **79**, 1 (2009).

[120] L. Liu, C.-F. Pai, Y. Li, H. W. Tseng, D. C. Ralph, and R. A. Buhrman, *Spin-Torque Switching with the Giant Spin Hall Effect of Tantalum*, (n.d.).

[121] V. E. Demidov, S. Urazhdin, E. R. J. Edwards, M. D. Stiles, R. D. McMichael, and S. O. Demokritov, *Control of Magnetic Fluctuations by Spin Current*, Phys. Rev. Lett. (2011).

[122] S. Kirkpatrick, C. D. Gelatt, and M. P. Vecchi, *Optimization by Simulated Annealing*, Science (80-.). **220**, 671 (1983).

[123] K. S. Lee, S. W. Lee, B. C. Min, and K. J. Lee, *Threshold Current for Switching of a Perpendicular Magnetic Layer Induced by Spin Hall Effect*, Appl. Phys. Lett. **102**,

(2013).

[124] B. Sutton, R. Faria, L. A. Ghantasala, R. Jaiswal, K. Y. Camsari, and S. Datta, *Autonomous Probabilistic Coprocessing With Petaflips per Second*, IEEE Access **8**, (2020).

[125] S. Ingvarsson, G. Xiao, S. S. P. Parkin, W. J. Gallagher, G. Grinstein, and R. H. Koch, *Low-Frequency Magnetic Noise in Micron-Scale Magnetic Tunnel Junctions S.*, Phys. Rev. Lett. **85**, 3289 (2000).

[126] C. G. Duan, J. P. Velev, R. F. Sabirianov, W. N. Mei, S. S. Jaswal, and E. Y. Tsymbal, *Tailoring Magnetic Anisotropy at the Ferromagnetic/Ferroelectric Interface*, Appl. Phys. Lett. **92**, 1 (2008).

[127] W. Bothe, *The Coincidence Method*, in *Nobel Lecture* (1954).

[128] B. Apolloni, C. Carvalho, and D. de Falco, *Quantum Stochastic Optimization*, Stoch. Process. Their Appl. **33**, 233 (1989).

[129] T. Hogg, *Quantum Computing and Phase Transitions in Combinatorial Search*, J. Artif. Intell. Res. **4**, 91 (1996).

[130] M. Steffen, W. van Dam, T. Hogg, G. Breyta, and I. Chuang, *Experimental Implementation of an Adiabatic Quantum Optimization Algorithm*, Phys. Rev. Lett. **90**, 4 (2003).

[131] M. W. Johnson, M. H. S. Amin, S. Gildert, T. Lanting, F. Hamze, N. Dickson, R. Harris, A. J. Berkley, J. Johansson, P. Bunyk, E. M. Chapple, C. Enderud, J. P. Hilton, K. Karimi, E. Ladizinsky, N. Ladizinsky, T. Oh, I. Perminov, C. Rich, M. C. Thom, E. Tolkacheva, C. J. S. Truncik, S. Uchaikin, J. Wang, B. Wilson, and G. Rose, *Quantum Annealing with Manufactured Spins*, Nature **473**, 194 (2011).

[132] V. N. Smelyanskiy, S. Knysh, and R. D. Morris, *Quantum Adiabatic Optimization and Combinatorial Landscapes*, Phys. Rev. E - Stat. Physics, Plasmas, Fluids, Relat. Interdiscip. Top. **70**, 18 (2004).

[133] R. Harris, M. W. Johnson, T. Lanting, A. J. Berkley, J. Johansson, P. Bunyk, E. Tolkacheva, E. Ladizinsky, N. Ladizinsky, T. Oh, F. Cioata, I. Perminov, P. Spear,

C. Enderud, C. Rich, S. Uchaikin, M. C. Thom, E. M. Chapple, J. Wang, B. Wilson, M. H. S. Amin, N. Dickson, K. Karimi, B. MacReady, C. J. S. Truncik, and G. Rose, *Experimental Investigation of an Eight-Qubit Unit Cell in a Superconducting Optimization Processor*, Phys. Rev. B - Condens. Matter Mater. Phys. **82**, 1 (2010).

[134] E. C. Stoner and E. P. Wohlfarth, *A Mechanism of Magnetic Hysteresis in Heterogeneous Alloys*, Philos. Trans. R. Soc. London. Ser. A, Math. Phys. Sci. **240**, 599 (1948).

[135] A. Thiaville, *Extensions of the Geometric Solution of the Two Dimensional Coherent Magnetization Rotation Model*, J. Magn. Magn. Mater. **182**, 5 (1998).

[136] E. Bonet, W. Wernsdorfer, B. Barbara, A. Benoît, D. Mailly, and A. Thiaville, *Three-Dimensional Magnetization Reversal Measurements in Nanoparticles*, Phys. Rev. Lett. **83**, 4188 (1999).

[137] J. L. F. Cuñado, A. Bollero, T. Pérez-Castañeda, P. Perna, F. Ajejas, J. Pedrosa, A. Gudín, A. Maldonado, M. A. Niño, R. Guerrero, D. Cabrera, F. J. Terán, R. Miranda, and J. Camarero, *Emergence of the Stoner-Wohlfarth Astroid in Thin Films at Dynamic Regime*, Sci. Rep. **7**, 1 (2017).

[138] Y. Henry, S. Mangin, J. Cucchiara, J. A. Katine, and E. E. Fullerton, *Distortion of the Stoner-Wohlfarth Astroid by a Spin-Polarized Current*, Phys. Rev. B - Condens. Matter Mater. Phys. **79**, 1 (2009).

[139] J. J. Nowak, R. P. Robertazzi, J. Z. Sun, G. Hu, J. H. Park, J. Lee, A. J. Annunziata, G. P. Lauer, R. Kothandaraman, E. J. O Sullivan, P. L. Trouilloud, Y. Kim, and D. C. Worledge, *Dependence of Voltage and Size on Write Error Rates in Spin-Transfer Torque Magnetic Random-Access Memory*, IEEE Magn. Lett. **7**, 4 (2016).

[140] K. Watanabe, B. Jinnai, S. Fukami, H. Sato, and H. Ohno, *Shape Anisotropy Revisited in Single-Digit Nanometer Magnetic Tunnel Junctions*, Nat. Commun. **9**, 5 (2018).

[141] A. Z. Pervaiz, L. A. Ghantasala, K. Y. Camsari, and S. Datta, *Hardware Emulation of Stochastic P-Bits for Invertible Logic*, Sci. Rep. **7**, 1 (2017).

[142] D. MacNeill, G. M. Stiehl, M. H. D. Guimaraes, R. A. Buhrman, J. Park, and D. C. Ralph, *Control of Spin-Orbit Torques through Crystal Symmetry in WTe 2 /Ferromagnet Bilayers*, Nat. Phys. **13**, 300 (2017).

[143] S. Jenkins, R. Chantrell, T. Klemmer, and R. F. L. Evans, *Extraordinary Temperature Dependent Magnetic Anisotropy of the Non-Collinear Antiferromagnet IrMn3*, ArXiv **220405**, 1 (2019).

[144] G. Vallejo-Fernandez, N. P. Aley, J. N. Chapman, and K. O'Grady, *Measurement of the Attempt Frequency in Antiferromagnets*, Appl. Phys. Lett. **97**, 1 (2010).